

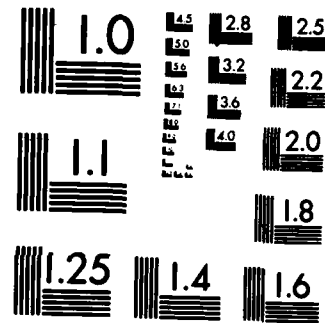
AD-A147 429 SOLID STATE RESEARCH(U) MASSACHUSETTS INST OF TECH 1/2  
LEXINGTON LINCOLN LAB A L MCWHORTER 15 FEB 84 1984-1  
ESD-TR-84-006 F19628-80-C-0002  
UNCLASSIFIED F/G 20/12 NL

UNCLASSIFIED

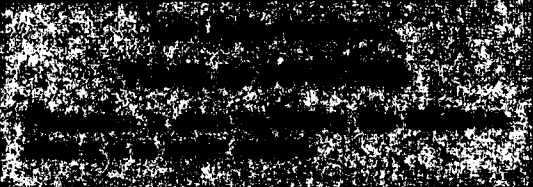
F/G 20/12

1/2

HL



AD-A147 429



**MASSACHUSETTS INSTITUTE OF TECHNOLOGY  
LINCOLN LABORATORY**

**SOLID STATE RESEARCH**

**QUARTERLY TECHNICAL REPORT**

**1 NOVEMBER 1983 — 31 JANUARY 1984**

**ISSUED 9 AUGUST 1984**

**Approved for public release; distribution unlimited.**

**LEXINGTON**

**MASSACHUSETTS**

## **ABSTRACT**

This report covers in detail the solid state research work of the Solid State Division at Lincoln Laboratory for the period 1 November 1983 through 31 January 1984. The topics covered are Solid State Device Research, Quantum Electronics, Materials Research, Microelectronics, and Analog Device Technology. Funding is primarily provided by the Air Force, with additional support provided by the Army, DARPA, Navy, NASA, and DOE.

<b>Accession For</b>	
NTIS GRA&I	<input checked="" type="checkbox"/>
DTIC TAB	<input type="checkbox"/>
Unannounced	<input type="checkbox"/>
Justification	
By _____	
Distribution/ _____	
<b>Availability Codes</b>	
Dist	Avail and/or Special
A-1	



## TABLE OF CONTENTS

<b>Abstract</b>	iii
<b>List of Illustrations</b>	vii
<b>List of Tables</b>	xi
<b>Introduction</b>	xiii
<b>Reports on Solid State Research</b>	xvii
<b>Organization</b>	xxvii
<b>1. SOLID STATE DEVICE RESEARCH</b>	<b>1</b>
1.1 Low-Threshold GaInAsP/InP Buried-Heterostructure Lasers with a Chemically Etched and Mass-Transported Mirror	1
1.2 Signal Correlation Using a One-Dimensional Electroabsorptive CCD Spatial Light Modulator	5
<b>2. QUANTUM ELECTRONICS</b>	<b>7</b>
2.1 Recent Advances in Solid State Lasers	7
2.2 High Average Power Mode-Locked Operation of Co:MgF <sub>2</sub> and Ni:MgF <sub>2</sub> Lasers	9
2.3 Temperature Dependence of Quantum Fluctuation Linewidth Broadening in GaAlAs Diode Lasers	10
<b>3. MATERIALS RESEARCH</b>	<b>15</b>
3.1 Role of Oxygen in Zone-Melting Recrystallization of Si Films on SiO <sub>2</sub> -Coated Si Substrates	15
3.2 Triple Ion-Implantation Technique for Formation of Shallow npn Bipolar Transistor Structures in Silicon	21
3.3 Identity of Residual Donors in InP	25
3.4 Depth Profiles of Traps in GaAs Epilayer on Dry-Etched GaAs Substrate	27
3.5 GaAs MESFETs Fabricated on Monolithic GaAs/Si Substrates	36

<b>4. MICROELECTRONICS</b>	<b>43</b>
4.1 Charge-Coupled Devices: Time-Integrating Correlator	43
4.2 Modification of Schottky-Diode Characteristics in GaAs by Dry Etching	46
4.3 Ultra-Low Temperature Growth of GaAs Using Chloride- Transport Vapor-Phase Epitaxy	49
4.4 Large-Area Ion-Beam-Assisted Etching of GaAs with High Etch Rates and Controlled Anisotropy	55
4.5 Submicrometer Gates for Field-Effect Transistors	59
4.6 Planar GaAs PIN Photodiode with Picosecond Time Response	62
<b>5. ANALOG DEVICE TECHNOLOGY</b>	<b>67</b>
5.1 Integration of Multiple Elastic Convolvers into a Communi- cation Signal Processor	67
5.2 Concept for a Holographic-Grating Bulk-Acoustic-Wave Reflective-Array Device	73

## LIST OF ILLUSTRATIONS

<b>Figure No.</b>		<b>Page</b>
1-1	Procedures for Formation of Transported Mirror	2
1-2	SEM Photographs of Longitudinal Cross Sections (a) Before and (b) After Mass Transport. In (b), Active Layer Is Stained for Contrast.	3
1-3	SEM Photographs Showing Perspective Views of (a) Transported and (b) Cleaved Mirrors. Active Layer Is Stained for Contrast.	4
1-4	(a) Light-Current Characteristics and (b) Emission Spectra of a GaInAsP/InP BH Laser with a Transported Mirror	5
2-1	Output vs Input Energy at a 20-Hz Repetition Rate from a Flashlamp-Pumped Nd:Cr:GSGG Laser	8
2-2	Average Power Output vs Pulse Repetition Rate for Nd:Cr:GSGG Laser at 10-J/Pulse Input Level	9
2-3	Linewidth of a CW Single-Frequency Mitsubishi TJS Laser at 293 and 1.7 K	11
2-4	Integrated Upper- and Lower-Sideband Intensities Relative to Main Frequency Intensity for a Mitsubishi TJS CW, Single-Frequency Diode Laser at 20°C	12
2-5	Fabry-Perot Spectrum of Mitsubishi TJS Diode Laser at 1.7 K for Three Output-Power Levels	13
3-1	Optical Micrograph of ZMR Si Film that Has Been Etch-Delineated to Show Sub-boundaries. Upper Graphite Heater Was Scanned in Direction from Top to Bottom of Micrograph.	15
3-2	Schematic Diagram Showing an Initially Planar Solid-Liquid Interface that Becomes Faceted, Causing Sub-boundaries	16
3-3	SIMS Profile of ZMR Sample that Had Encapsulating Layer Removed	17
3-4	Oxygen Map Obtained by SIMS, Showing Oxygen Concentrated Along Sub-boundaries	17
3-5	(a) Schematic Diagram Showing Oxygen Concentration as a Function of Distance in Vicinity of Solid-Liquid Interface. (b) Schematic Diagram Showing Liquidus Temperature $T_L$ and Melt Temperatures $T$ (Dashed Lines) as Functions of Distance in Vicinity of Solid-Liquid Interface.	18

Figure No.		Page
3-6	Schematic Diagram Showing Rejection of Impurities from the Solid into the Liquid at a Faceted Interface, Causing an Increase in Impurity Concentration at Inner Corners of Interface	20
3-7	As and B Depth Profiles Obtained by SIMS Analysis of Triply Implanted Si(100) Samples Before and After Annealing	22
3-8	As and B Depth Profiles Obtained by SIMS Analysis of Triply Implanted Poly-Si/Si(100) Samples Before and After Annealing	24
3-9	Temperature Dependence of Schottky-Diode Capacitance Measured (a) for $V_b = 0.30$ V, and (b) for Values of $V_b$ Obtained with Servo-Feedback Circuit	28
3-10	Depth Profiles of $(N_D - N_A)$ at Room Temperature (RT) and Liquid Nitrogen Temperature (LN) Obtained by Conventional C-V Method (Dashed Lines, After Reference 27) and by Present Method (Solid Lines)	29
3-11	Temperature Dependence of $(N_D - N_A)$ for Values of Depletion Width W Between 0.30 and 0.60 $\mu\text{m}$	30
3-12	Temperature Dependence of $\Delta C$ Obtained by DLTS Measurements Using Pulses Large Enough to Fill All Traps in Depletion Region, for (a) W Values Between 0.30 and 0.50 $\mu\text{m}$ , and (b) W = 0.55 and 0.60 $\mu\text{m}$	32
3-13	Temperature Dependence of $\Delta C$ Obtained by DLTS Measurements Using Trap-Filling Pulse with $V_p = 0.15$ V, for W Between 0.30 and 0.60 $\mu\text{m}$	33
3-14	Temperature Dependence of $\Delta C$ Obtained by ODLTS Measurements for W Between 0.30 and 0.60 $\mu\text{m}$	34
3-15	Depth Profiles of Hole Trap and Three Electron Traps	35
3-16	Design of MGS GaAs MESFET Fabricated on Monolithic GaAs/Si Substrate. Doping Concentrations of n and n <sup>+</sup> GaAs Layers Are $1 \times 10^{17}$ and $2.5 \times 10^{18} \text{ cm}^{-3}$ , Respectively.	36
3-17	Nomarski Interference Micrograph Showing Surface Morphology of GaAs Layer Grown by MBE on Ge-Coated Si Substrate	38
3-18	Optical Micrograph of MGS GaAs MESFET with Gate Length of 2.1 $\mu\text{m}$ and Gate Width of 200 $\mu\text{m}$	38
3-19	Schottky-Diode Characteristic Between Source and Gate of MGS GaAs MESFET	39

Figure No.		Page
3-20	Transistor Characteristics of MGS GaAs MESFET. Top Curve Is for $V_{gs} = 0.5$ V.	39
4-1	Schematic Diagram of a Correlator System Using a CCD Time-Integrating Correlator and a Digital Post-processor for Pattern-Noise Suppression and Additional Integration	44
4-2	Top Trace: CCD Input Signal Consisting of an m-Sequence with Gaussian Noise (SNR = 50 dB). Middle Trace: CCD Correlator Output. Bottom Trace: Output of Post-processor After Integrating 32768 Frames of CCD Output Data.	45
4-3	Semilog Plot of Forward Current Density as a Function of Voltage for a Control Sample, Samples Etched by Ar IBE at 500 V, and Samples Etched by IBAE with an $Ar^+$ Energy of 500 V and $Cl_1$ Flux Equivalent to $5 \times 10^{-4}$ Torr	47
4-4	Capacitance-Voltage Plot for a Control Sample, and for Samples Reactive-Ion Etched in $CF_4$ at 250, 500, and 700 V	50
4-5	Epitaxial Growth Rate as a Function of Combined Partial Pressures of $AsH_3$ and $AsCl_3$ for Various GaAs Source Temperatures	52
4-6	Epitaxial Growth Rate as a Function of GaAs Source Temperature for a Constant $AsCl_3$ Partial Pressure and Two $AsH_3$ Partial Pressures	53
4-7	Schematic Diagram of IBAE System Which Consists of an Ion Source, One or More Reactive Gas Jets (Only One Shown), and a Cold Trap to Pump Unused Reactive Gas and Reaction Products. Stainless-Steel Vacuum Chamber Is Pumped Either with a Cryopump or a Cold Trapped Diffusion Pump.	56
4-8	Diagram Showing Effect of Ion Source to Sample Distance on Profile of Etched Structure	57
4-9	Scanning Electron Micrographs of GaAs Samples Etched with (a) a Sample-to-Source Distance of 19 cm, and (b) a Sample-to-Source Distance of 45.5 cm. A $20\text{-}\mu\text{A cm}^{-2}$ Beam of 500-eV $Ar^+$ and an Equivalent Reactive Flux of $2 \times 10^{-3}$ Torr Were Used to Obtain These Profiles.	58
4-10	Scanning Electron Micrograph of a GaAs Sample Etched Under Same Conditions as Sample Shown in Figure 4-9(b). Grating Is Etched to About a $1.5\text{-}\mu\text{m}$ Depth.	59

<b>Figure No.</b>		<b>Page</b>
4-11	Submicrometer T-Shaped Gate Fabricated Using Deep Ultraviolet Lithography	60
4-12	Plated and Recessed Submicrometer-Gate FET	61
4-13	0.5 × 150- $\mu$ m Gate FET	61
4-14	Cross Section of Planar GaAs PIN Photodiode	62
4-15	Impulse Response of Planar GaAs PIN Photodiode Biased at -1.5 V	63
4-16	Correlation Measurement of Planar GaAs PIN Photodiode and a Photoconductive Sampling Gate	64
5-1	Long-Convolver Subassembly	68
5-2	Short-Convolver Subassembly	69
5-3	Convolver Module Switching-Matrix Schematic	71
5-4	Convolver Module Assembly	72
5-5	Short-Convolver Correlation Waveform	73
5-6	Long-Convolver Correlation Waveform	74
5-7	Bulk-Acoustic-Wave Grating Reflector. Stored Grating Is Created by Interference of Two Laser Beams. Incident Acoustic Beam Strongly Interacts with Grating in a Narrow Frequency Band, Thus Forming a Bandpass Filter.	75
5-8	Theoretical Response of a Holographic-Grating Bandpass Filter in LiNbO <sub>3</sub> Calculated from Coupled-Wave Theory	76

## LIST OF TABLES

Table No.		Page
3-1	Measured Values of $n_{77}$ and $\mu_{77}(10^4 \text{ cm}^2\text{V}^{-1}\text{s}^{-1})$ and Estimated $N_D$ , $N_A$ , and Donor Concentrations in LEC Boules of InP (All Con- centrations Given in Units of $10^{15} \text{ cm}^{-3}$ )	26
4-1	Parameters Deduced from I-V Measurements on Schottky Diodes	46
4-2	DLTS Measurements	48
4-3	Parameters Deduced from I-V Measurements on Schottky Diodes	49
4-4	Carrier Concentration Dependence on Dopant Partial Pressure	54
4-5	Carrier Concentration Dependence on Arsine Partial Pressure	54
5-1	Elastic Convolver Characteristics	70
5-2	Module Performance Characteristics	70

## INTRODUCTION

### 1. SOLID STATE DEVICE RESEARCH

The InP mass-transport technique has been used to improve chemically etched mirrors for GaInAsP/InP buried-heterostructure lasers. Devices with one such mirror and a second cleaved mirror show high device yield, threshold currents as low as 5 mA, and differential quantum efficiency as high as 33 percent.

The performance of an electroabsorptive CCD spatial light modulator in electrical signal correlation has been analyzed. In the space-integrating mode, such a correlator should have a dynamic range from 20 to 40 dB. When operated as a time-integrating correlator, the range improves to 35 to 55 dB.

### 2. QUANTUM ELECTRONICS

The tuning range of the Ti:Al<sub>2</sub>O<sub>3</sub> laser has been extended to cover the wavelength region from 660 to 986 nm. Operation at 1060 nm with a 5-percent differential power efficiency has been obtained from a flashlamp-pumped laser rod of the sensitized garnet Nd:Cr:Gd<sub>3</sub>Sc<sub>2</sub>Ga<sub>3</sub>O<sub>12</sub> (GSGG).

Tunable, actively mode-locked operation of a CW Co:MgF<sub>2</sub> laser has produced pulses as short as 36 ps in the 1.6- to 2.0-μm region and average output powers of 2 W. A 23-ps output was obtained from a Ni:MgF<sub>2</sub> laser.

Quantum-fluctuation linewidth broadening, including relaxation sideband resonances, has been studied in GaAlAs diode lasers as a function of power from 1.7 to 300 K. The power-independent linewidth was consistent with a phenomenological model involving electron-number fluctuations. In agreement with theory, the relative strength of the relaxation-sideband resonances decreased linearly with increasing laser power.

### 3. MATERIALS RESEARCH

Secondary-ion mass spectroscopic analysis has shown that oxygen is strongly concentrated at the sub-boundaries in zone-melting-recrystallized silicon-on-insulator films prepared by the graphite-strip-heater technique. This observation suggests that the formation of sub-boundaries during recrystallization may be caused by constitutional supercooling resulting from the presence of oxygen that is dissolved into the molten Si zone from the adjacent SiO<sub>2</sub> layers.

Bipolar npn transistor structures with emitter-base junction depths and base widths of only about 0.1 μm have been obtained by implantation of B<sup>+</sup> and As<sup>+</sup> ions into amorphous layers formed in n-Si wafers by the prior implantation of Si<sup>+</sup> ions. The implanted dopant atoms are activated by thermal annealing, which results in the recrystallization of the amorphous layers by solid-phase epitaxy to form single-crystal regions that are almost free of defects near the emitter-base and base-collector junctions.

Samples of nominally undoped, n-type InP have been supplied to the Royal Signals and Radar Establishment, United Kingdom, for characterization by means of low-temperature photoluminescence measurements at high magnetic fields. The photoluminescence data indicate that S is the dominant donor in the highest-purity polycrystalline ingots, while in high-purity InP boules grown by the liquid-encapsulated Czochralski method the principal donor is an unidentified species (possibly a native defect), with S as a significant species and Si as a minor one.

The accuracy of measuring the depth profiles of traps in semiconductor samples by deep-level transient spectroscopy has been increased by using a system that incorporates a servo-feedback circuit to adjust the DC bias voltage so that the depletion width and therefore the region sampled do not vary as the temperature is increased. In measurements on a GaAs epilayer grown on a dry-etched GaAs substrate, we found that the density of the principal electron traps generally decreases with increasing distance from the substrate.

GaAs metal-semiconductor field-effect transistors have been fabricated for the first time on monolithic GaAs/Si substrates, which were prepared by growing GaAs layers on Ge-coated Si wafers. The transistors exhibit good operating characteristics, with maximum transconductance of 105 mS/mm for a gate length of 2.1  $\mu\text{m}$ .

#### 4. MICROELECTRONICS

A digital post-processor for a CCD time-integrating correlator has been used to remove pattern noise and to increase integration times to more than 1 s. The combined CCD/digital system has demonstrated a process gain of 70 dB with a bandwidth of 10 MHz. The removal of the pattern noise increased the effective CCD dynamic range to a value of 67 dB based on the device temporal noise.

Damage induced in GaAs by ion-beam etching with Ar, reactive-ion etching with  $\text{CF}_4$  and  $\text{CHF}_3$ , and ion-beam-assisted etching with Ar on  $\text{Cl}_2$  has been studied. The degree of damage was determined by evaluating Schottky diodes fabricated on the etched surfaces and by using deep-level transient spectroscopy. We found that variations in the etching conditions had a strong effect on the measured characteristics of the samples.

Vapor phase epitaxy of high-quality GaAs films using chloride transport has been achieved at a growth temperature of 500°C. The films are grown at atmospheric pressure in a conventional  $\text{AsCl}_3\text{-GaAs-H}_2$  reactor. The addition of  $\text{AsH}_3$  to the gas flow over the GaAs source is the key element in achieving high-quality epitaxial films at this low temperature.

An improved system for ion-beam-assisted etching has been developed. Structures with aspect ratios in excess of 40:1 have been etched in GaAs. In addition, 5-percent etch uniformity has been achieved over areas as large as 4  $\text{cm}^2$ .

Fabrication procedures for submicrometer-gatelength GaAs MESFETs are being developed. Deep UV lithography and novel process sequences are used to achieve the required resolution. Initial devices show great promise, with a maximum available gain of 6.5 dB at 18 GHz.

A planar GaAs PIN photodiode has been developed which exhibits an impulse response of 19-ps FWHM to 4-ps pulses from a near-infrared laser. The external quantum efficiency of this device exceeds 10 percent at a -1.5-V bias.

## 5. ANALOG DEVICE TECHNOLOGY

Four 1.4- $\mu$ s-long and two 22- $\mu$ s-long elastic convolvers with 100-MHz bandwidth have been developed and integrated into a high-speed switching matrix contained on a densely packed stripline circuit board. The circuit sequentially connects convolvers to provide continuous demodulation of spread-spectrum communication signals at both high and low data rates. Measurements of the main-lobe/side-lobe rms ratios of correlation waveforms for a pseudorandom code yield 29.8 dB for the long convolvers and 16.5 dB for the short, both close to theoretical values.

A concept has been further developed for using a holographically written electroacoustic grating in bulk LiNbO<sub>3</sub> to form high-frequency acoustic filters. Mode-coupling calculations using previously measured electroacoustic coefficients predict a bulk-acoustic-wave reflection coefficient per grating element of  $2.7 \times 10^{-4}$  at a typical strength of 50 kV/cm for the stored periodic electric field. A device is being fabricated which should provide strong interaction between the acoustic wave and the charge grating.

## REPORTS ON SOLID STATE RESEARCH

15 November 1983 through 15 February 1984

### PUBLISHED REPORTS

#### Journal Articles

##### JA No.

5429	20 GHz Optical Waveguide Sampler	L.A. Molter-Orr H.A. Haus* F.J. Leonberger	IEEE J. Quantum Electron. QE-19, 1877 (1983)
5456	LPE Growth and Characterization of InP Photodiodes	S.H. Groves M.C. Plonko C.A. Armiento V. Diadiuk	J. Cryst. Growth 64, 83 (1983)
5472	An Ultrafast All-Optical Gate	A. Lattes H.A. Haus* F.J. Leonberger E.P. Ippen*	IEEE J. Quantum Electron. QE-19, 1718 (1983)
5480	Dual Ion Implantation Technique for Formation of Shallow $p^*/n$ Junctions in Silicon	B-Y. Tsaur C.H. Anderson, Jr.	J. Appl. Phys. 54, 6336 (1983)
5482	A Technique for the Determination of Stress in Thin Films	E.I. Bromley J.N. Randall D.C. Flanders R.W. Mountain	J. Vac. Sci. Technol. B 1, 1364 (1983)
5489	Laser Direct Writing for VLSI	D.J. Ehrlich J.Y. Tsao	In <i>VLSI Electronics: Microstructure Science</i> , edited by N.G. Einspruch (Academic Press, New York, 1984), Vol. 7, pp. 129-164
5496	Self-Developing UV Photoresist Using Excimer Laser Exposure	T.F. Deutsch M.W. Geis	J. Appl. Phys. 54, 7201 (1983)

\* Author not at Lincoln Laboratory.

**JA No.**

5500	A Review of Laser-Microchemical Processing	D.J. Ehrlich J.Y. Tsao	J. Vac. Sci. Technol. B 1, 969 (1983)
5503	Optical Heterodyne Spectroscopy with Frequency-Modulated and Amplitude-Modulated Semiconductor Lasers	W.Lenth	Opt. Lett. 8, 575 (1983)
5508	Orientation Filtering by Growth-Velocity Competition in Zone-Melting Recrystallization of Silicon on SiO <sub>2</sub>	H.A. Atwater* C.V. Thompson* H.I. Smith* M.W. Geis	Appl. Phys. Lett. 43, 1126 (1983)
5512	Effects of Dry Etching on GaAs	S.W. Pang G.A. Lincoln R.W. McClelland P.D. DeGraff M.W. Geis W.J. Piacentini	J. Vac. Sci. Technol. B 1, 1334 (1983)
5513	Read-Only Memory with Electron-Beam Programmable Floating-Gate Transistors	D.C. Shaver	J. Vac. Sci. Technol. B 1, 1084 (1983)
5514	Low-Loss GaInAsP Buried-Heterostructure Optical Waveguide Branches and Bends	L.M. Johnson Z.L. Liau S.H. Groves	Appl. Phys. Lett. 44, 278 (1984)
5515	Silicon Nitride Stencil Masks for High Resolution Ion Lithography Proximity Printing	J.N. Randall D.C. Flanders N.P. Economou J.P. Donnelly E.I. Bromley	J. Vac. Sci. Technol. B 1, 1152 (1983)

---

\* Author not at Lincoln Laboratory.

**JA No.**

5517	Nitrocellulose as a Self-Developing Resist with Submicrometer Resolution and Processing Stability	M.W. Geis J.N. Randall T.F. Deutsch N.N. Efremow J.P. Donnelly J.D. Woodhouse	J. Vac. Sci. Technol. B 1, 1178 (1983)
5520	Large Area Ion Beam Assisted Etching of GaAs with High Etch Rates and Controlled Anisotropy	G.A. Lincoln M.W. Geis S. Pang N.N. Efremow	J. Vac. Sci. Technol. B 1, 1043 (1983)
5521	Synthesis of Metastable, Semiconducting Ge-Sn Alloys by Pulsed UV Laser Recrystallization	S. Oguz* W. Paul* T.F. Deutsch B-Y. Tsaur D.V. Murphy	Appl. Phys. Lett. 43, 848 (1983)
5534	Structural Characterization by Transmission Electron Microscopy of Silicon Grown Over Submicrometer-Period Gratings of Deposited Tungsten	B.A. Vojak D.D. Rathman J.A. Burns S.M. Cabral N.N. Efremow	Appl. Phys. Lett. 44, 223 (1984)
5539	Nonreciprocal Laser-Microchemical Processing: Spatial Resolution Limits and Demonstration of 0.2- $\mu$ m Linewidths	D.J. Ehrlich J.Y. Tsao	Appl. Phys. Lett. 44, 267 (1984)
5544	Deep UV Exposure of Ag <sub>2</sub> Se/GeSe <sub>2</sub> Utilizing an Excimer Laser	K.J. Polasko* D.J. Ehrlich J.Y. Tsao R.F.W. Pease* E.E. Marinero*	IEEE Electron Device Lett. EDL-5, 24 (1984)
5552	Frequency-Modulation (FM) Spectroscopy — Theory of Lineshapes and Signal-to-Noise Analysis	G.C. Bjorklund* M.D. Levenson* W. Lenth C. Ortiz*	Appl. Phys. B 32, 145 (1983)

\* Author not at Lincoln Laboratory.

**JA No.**

- 5553 Linewidth Measurements of a (GaAl)As Diode Laser with a High Reflectivity Coating W. Lenth Appl. Phys. Lett. 44, 283 (1984)

**Meeting Speeches****MS No.**

- 6221 Performance Criteria of Components Required for Electrooptic Analog-to-Digital Conversion R.A. Becker F.J. Leonberger *Integrated Optics III*, L.D. Hutcheson and D.G. Hall, Eds., Proc. SPIE 408, 50-56 (1983)
- 6292 A Precision Wide-Range Optical Gap Measurement Technique D.C. Flanders T.M. Lysczczarz J. Vac. Sci. Technol. B 1, 1196 (1983)
- 6293 Generation of <50 nm Period Gratings Using Edge Defined Techniques D.C. Flanders N.N. Efremow J. Vac. Sci. Technol. B 1, 1105 (1983)
- 6329A Resonant Tunneling Through Quantum Wells at 2.5 THz T.C.L.G. Sollner W.D. Goodhue P.E. Tannenwald C.D. Parker D.D. Peck Conference Digest, Eighth International Conference on Infrared and Millimeter Waves, Miami Beach, 12-17 December 1983, p. TS.1
- 6330 Q-Switched Semiconductor Diode Lasers with Integrated Modulators D.Z. Tsang J.N. Walpole *Integrated Optics III*, L.D. Hutcheson and D.G. Hall, Eds., Proc. SPIE 408, 128-132 (1983)
- 6393 Wideband Signal Processing for Communication and Radar J.H. Cafarella Proceedings 1983 IEEE National Telesystems Conference, San Francisco, 14-16 November 1983, pp. 55-58

**MS No.**

6435	Wide-Bandwidth HgCdTe Photodiode Photomixers at $28 \mu\text{m}$	D.L. Spears	Conference Digest, Eighth International Conference on Infrared and Millimeter Waves, Miami Beach, 12-17 December 1983
------	--	-------------	--

\* \* \* \* \*

**UNPUBLISHED REPORTS****Journal Articles****JA No.**

5499	A CCD Time-Integrating Correlator	B.E. Burke D.L. Smythe	Accepted by IEEE J. Solid-State Circuits
5504	A High-Speed Digitally Programmable CCD Transversal Filter	A.M. Chiang B.E. Burke	Accepted by IEEE J. Solid-State Circuits
5527	Zone Melting Recrystallization of Thick Silicon on Insulator Films	H.A. Atwater* H.I. Smith* C.V. Thompson* M.W. Geis	Accepted by Mater. Lett.
5536	Monolithic Silicon Bolometers	P.M. Downey* A.D. Jeffries* S.S. Meyer* R.W. Weiss* F.J. Bachner J.P. Donnelly W.T. Lindley R.W. Mountain D.J. Silversmith	Accepted by Appl. Opt.
5538	The Band Structure of a-Sn and Ge-Sn Alloys	S.H. Groves W. Paul*	Accepted by IEE Proceedings

---

\* Author not at Lincoln Laboratory.

**JA No.**

5546	Efficient AlGaAs Shallow-Homojunction Solar Cells	R.P. Gale J.C.C. Fan G.W. Turner R.L. Chapman J.V. Pantano	Accepted by Appl. Phys. Lett.
5549	Dry Etching Induced Damage in Si and GaAs	S.W. Pang	Accepted by Solid State Technol.
5550	Mode Locked Operation of Co:MgF <sub>2</sub> and Ni:MgF <sub>2</sub> Lasers	B.C. Johnson P.F. Moulton A. Mooradian	Accepted by Opt. Lett.
5559	Passive Ti:LiNbO <sub>3</sub> Channel Waveguide TE-TM Mode Splitter	D. Yap L.M. Johnson G.W. Pratt, Jr.*	Accepted by Appl. Phys. Lett.
5562	Residual Donors in LEC Indium Phosphide	P.J. Dean* M.S. Skolnick* B. Cockayne* W.R. MacEwan* G.W. Iseler	Accepted by J. Cryst. Growth
5564	Signal Correlation Using a One-Dimensional Electro-absorptive CCD Spatial Light Modulator	R.H. Kingston	Accepted by Proc. IEEE
5569	The Future of High-Efficiency Solar Cells	J.C.C. Fan	Accepted by Solar Cells
5570	Annealing of Damage in Se <sup>+</sup> Implanted InP	J.D. Woodhouse J.P. Donnelly P.M. Nitishin E.B. Owens J.L. Ryan	Accepted by Solid-State Electron.
5573	Molecular Astronomy Using Heterodyne Detection at 691 GHz	D.D. Peck H.R. Fetterman* D. Buhl* G. Chin* S. Petuchowski*	Accepted by Int'l. J. Infrared and Millimeter Waves

---

\* Author not at Lincoln Laboratory.

### **Meeting Speeches\***

#### **MS No.**

5707L	<b>Laser Microchemistry: New Chemical Mechanisms and Solid-State Device Applications</b>	D.J. Ehrlich	Seminar, Department of Chemistry, Stanford University, 6 December 1983
6008D	<b>High-Efficiency, Low Cost Tandem Cells</b>	J.C.C. Fan	American Physical Society, San Francisco, 21-23 November 1983
6106C	<b>Preparation of High-Quality Silicon Films on Insulators by Zone-Melting Recrystallization</b>	B-Y. Tsaur	Meeting of the Institute of Chinese Engineers, Boston Chapter, M.I.T., 5 November 1983
6455	<b>An Introduction to Semiconductor Lasers</b>	Z.L. Liau	
6283A	<b>Solid State Lasers</b>	P.F. Moulton	NSF Workshop on the Future of Light-Wave Technology, University of Southern California, Los Angeles, 31 January 1984
6310C	<b>Microwave Semiconductor Devices</b>	W.T. Lindley	Graduate Student Seminar, Howard University, Washington, D.C., 29 November 1983
6373A	<b>Analog Signal Processing in LiNbO<sub>3</sub>: The Electrooptic Analog-to-Digital Converter</b>	R.A. Becker	Seminar, IEEE Student Chapter, University of California at Los Angeles, 14 November 1983

\* Titles of Meeting Speeches are listed for information only. No copies are available for distribution.

**MS No.**

6389A,B	Wideband Analog Signal Processing with Superconductive Circuits	S.A. Reible	Interdepartmental Physics Colloquium, Westinghouse Research and Development Center, Pittsburgh, 10 November 1983; and Seminar, Hughes Aircraft Company, Ground Systems Group, Fullerton, California, 30 November 1983
6407	Semi-Insulating InGaAs Optoelectronic Switches	V. Diadiuk S.H. Groves	1983 International Electron Devices Meeting, Washington, D.C., 5-7 December 1983
6408	High-Speed InP-Based Photodetectors	F.J. Leonberger V. Diadiuk	
6409	Impurity Distribution in Zone-Melting-Recrystallized Silicon-on-Insulator Films	J.C.C. Fan B-Y. Tsaur C.K. Chen J.R. Dick* L.L. Kazmerski*	Materials Research Society, Boston, 14-17 November 1983
6483	Rapid Thermal Annealing of Composite TaSi <sub>2</sub> /n <sup>+</sup> Poli-Si Silicide Films	D.L. Kwong* R. Kwor* B-Y. Tsaur K. Daneshvar*	
6433	Fabrication and Characterization of Ti-Indiffused and Proton Exchange Waveguides in LiNbO <sub>3</sub>	R.A. Becker	SPIE, Los Angeles, 22-27 January 1984
6438	An Electroabsorptive CCD Spatial Light Modulator	R.H. Kingston B.E. Burke K.B. Nichols F.J. Leonberger	

\* Author not at Lincoln Laboratory.

**MS No.**

6524	Surface and Gas Phase Processes in Photodeposition in Small Zones	J.Y. Tsao D.J. Ehrlich	SPIE, Los Angeles, 22-27 January 1984
6540	Buried Heterostructure Q-Switched Diode Lasers	D.Z. Tsang J.N. Walpole Z.L. Liau S.H. Groves	
6488	Laser Photochemical Fabri- cation of Microstructures	D.J. Ehrlich	Seminar, Electrical Engineering Department, M.I.T., 14 December 1983
6493	Spectral Properties of Semi- conductor Diode Lasers	A. Mooradian	International Conference on Lasers '83, San Francisco, 12-16 December 1983
6495	Crystal Growth by Molecular Beam Epitaxy	A.R. Calawa	Seminar, American Association for Crystal Growth, Lexington, Massachusetts, 14 December 1983
6507	Laser Direct Write Techniques for IC Development, Yield Improvement and Testing	D.J. Silversmith	Seminar, Hughes Aircraft Company, Carlsbad, California, 10 January 1984
6507A	Laser Direct Write Techniques	D.J. Silversmith	New England Chapter Meeting, American Vacuum Society, Bedford, Massachusetts, 18 January 1984
6532	Low Threshold GaInAsP/InP Buried-Heterostructure Lasers with a Chemically Etched and Mass-Transported Mirror	Z.L. Liau J.N. Walpole D.Z. Tsang	OFC '84, New Orleans, 24-26 January 1984
6552	Laser-Induced Surface-Chemical Processing	J.Y. Tsao D.J. Ehrlich	Seminar, General Electric Research and Development Center, Schenectady, New York, 2 February 1984

## ORGANIZATION

### SOLID STATE DIVISION

A.L. McWhorter, *Head*  
I. Melngailis, *Associate Head*  
E. Stern, *Associate Head*  
J.F. Goodwin, *Assistant*

P.E. Tannenwald, *Senior Staff*

### QUANTUM ELECTRONICS

A. Mooradian, *Leader*  
P.L. Kelley, *Associate Leader*

Barch, W.E.  
Belanger, L.J.  
Brueck, S.R.J.  
Burke, J.W.  
Bushee, J.F., Jr.  
DeFeo, W.E.  
Deutsch, T.F.  
Ehrlich, D.J.  
Feldman, B.  
Hancock, R.C.

Harrison, J.\*  
Johnson, B.C.\*  
Killinger, D.K.  
Lenth, W.  
Menyuk, N.  
Moulton, P.F.  
Sedlacek, J.H.C.  
Sharpe, K.A.  
Sullivan, D.J.  
Tsao, J.Y.

### ELECTRONIC MATERIALS

A.J. Strauss, *Leader*  
J.C.C. Fan, *Associate Leader*  
J.G. Mavroides, *Senior Staff*  
H.J. Zeiger, *Senior Staff*

Anderson, C.H., Jr.  
Branz, H.M.\*  
Button, M.J.  
Chapman, R.L.  
Chen, C.K.  
Choi, H.K.  
Connors, M.K.  
Delaney, E.J.  
Fahey, R.E.  
Finn, M.C.  
Gale, R.P.  
Iseler, G.W.  
King, B.D.  
Kolesar, D.F.  
Krohn, L., Jr.  
Mastromattei, E.L.  
McClelland, R.W.  
Metze, G.M.  
Nitishin, P.M.  
Palm, B.J.  
Pantano, J.V.  
Tracy, D.M.  
Tsaur, B-Y.  
Turner, G.W.  
Windhorn, T.H.

### APPLIED PHYSICS

R.C. Williamson, *Leader*  
F.J. Leonberger, *Assistant Leader*  
T.C. Harman, *Senior Staff*  
R.H. Kingston, *Senior Staff*  
R.H. Rediker, *Senior Staff*

Becker, R.A.  
Carter, F.B.  
Chinnock, C.B.  
Cox, C.H., III  
DeMeo, N.L., Jr.  
Diadiuk, V.  
Donnelly, J.P.  
Ferrante, G.A.  
Groves, S.H.

Hovey, D.L.  
Johnson, L.M.  
Liau, Z.L.  
Lind, T.A.  
McBride, W.F.  
Molter-Orr, L.\*  
O'Donnell, F.J.  
Paladino, A.E.

Plonko, M.C.  
Schloss, R.P.\*  
Spears, D.L.  
Tsang, D.Z.  
Walpole, J.N.  
Whitaker, N.\*  
Woodhouse, J.D.  
Yap, D.\*

\* Research Assistant

## ANALOG DEVICE TECHNOLOGY

J.H. Cafarella, *Leader*  
R.W. Ralston, *Associate Leader*

Anderson, A.C.  
Arsenault, D.R.  
Boisvert, R.R.  
Bouman, C.A.  
Brogan, W.T.  
Dolat, V.S.  
Fischer, J.H.  
Fitch, G.L.  
Flynn, G.T.

Gottschalk, P.G.\*  
Green, J.B.  
Hauser, E.M.  
Holtham, J.H.  
Kernan, W.C.  
Lattes, A.L.  
Macedo, E.M., Jr.  
Macopoulos, W.

Melngailis, J.†  
Oates, D.E.  
Reible, S.A.  
Sage, J.P.  
Slattery, R.L.  
Smith, L.N.  
Withers, R.S.  
Yao, I.

## MICROELECTRONICS

W.T. Lindley, *Leader*  
N.P. Economou, *Associate Leader*  
R.A. Murphy, *Assistant Leader*

Bozler, C.O.  
Bromley, E.I.  
Burke, B.E.  
Cabral, S.M.  
Calawa, A.R.  
Chen, C.L.  
Chiang, A.M.  
Chu, A.  
Clifton, B.J.  
Daniels, P.J.  
Durant, G.L.  
Efremow, N.N., Jr.  
Felton, B.J.  
Flanders, D.C.  
Geis, M.W.

Gray, R.V.  
Hollis, M.A.  
Kosicki, B.B.  
Lax, B.†  
LeCoz, Y.L.\*  
Lincoln, G.A., Jr.  
Lysczarz, T.M.  
Mahoney, L.J.  
Manfra, M.J.  
McGonagle, W.H.  
Mountain, R.W.  
Mroczkowski, I.H.  
Nichols, K.B.  
Pang, S.W.  
Parker, C.D.

Peck, D.D.  
Piacentini, W.J.  
Pichler, H.H.  
Rabe, S.  
Randall, J.N.  
Rathman, D.D.  
Rienstra, J.\*  
Shaver, D.C.  
Silversmith, D.J.  
Smythe, D.L., Jr.  
Sollner, T.C.L.G.  
Taylor, J.A.\*  
Vera, A.  
Vojak, B.A.  
Wilde, R.E.

---

\* Research Assistant

† Part Time

## 1. SOLID STATE DEVICE RESEARCH

### 1.1 LOW-THRESHOLD GaInAsP/InP BURIED-HETEROSTRUCTURE LASERS WITH A CHEMICALLY ETCHED AND MASS-TRANSPORTED MIRROR

Chemically etched mirrors<sup>1-6</sup> are potentially very important for monolithic optoelectronic integration and for short or coupled cavity lasers. However, the etched mirrors reported to date<sup>1-6</sup> were generally not flat, not vertical, or not easily applicable to the conventional buried-heterostructure lasers. These problems can be solved by using the recently developed mass-transport technique,<sup>7</sup> and promising initial results are described below.

Figure 1-1(a-c) illustrates the formation of a chemically etched mirror facet and the subsequent smoothing of the facet by using the mass-transport phenomenon. The etched profile in Figure 1-1(b) is obtained by a repeated use of a mixture of  $H_3PO_4$  and  $HCl$  (see References 8 and 9) and an aqueous solution of  $K_3Fe(CN)_6$  and  $KOH$ . The mass transport is carried out by heating the wafer at a temperature of  $670^\circ$  to  $690^\circ C$  in  $H_2$  and  $PH_3$  atmosphere.<sup>7</sup>

Figure 1-2(a-b) shows SEM photographs of the cross sections of samples before and after the mass transport. Note that a smooth mirror surface is obtained after transport, and that the GaInAsP active region is totally buried in InP.

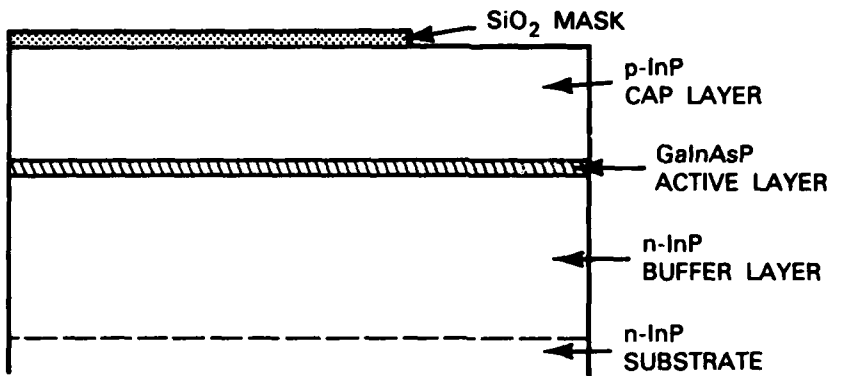
To fabricate the "transported mirror" on a stripe-geometry laser, we start with a mass-transported GaInAsP/InP buried-heterostructure (BH) laser wafer<sup>7</sup> in which the laser stripe edge is parallel to the (011) crystallographic planes; at the end of each laser mesa, a planar region is retained. The transported mirror is then formed in that planar region, as shown in the SEM perspective view of Figure 1-3(a). For comparison, a BH laser mesa with a cleaved-mirror facet is shown in Figure 1-3(b).

After metallization and dicing, the finished BH lasers have one transported mirror and one cleaved mirror. They are conveniently characterized by using the emission from the cleaved mirror because the transported mirror is coated during fabrication with phosphosilicate glass and Ti/Au metallization layers. A high yield of good BH lasers has been obtained. For example, 50 percent of some 40 devices tested from Wafer 657 show threshold currents between 5 and 10 mA. Figure 1-4(a-b) shows the CW light-current characteristics and emission spectra of one device from Wafer 655 mounted p-side up.

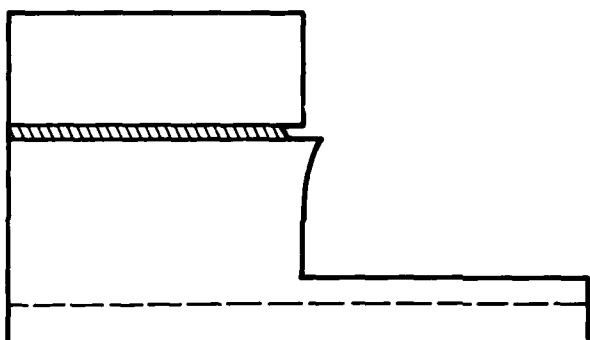
It should be noted that the present threshold currents are significantly lower than the >50-mA values previously reported<sup>1-4</sup> for GaInAsP/InP lasers with etched mirrors, and are comparable to the lowest achieved for the lasers with both mirrors cleaved. Nevertheless, further improvements in threshold current, efficiency, and mode behavior might be obtained by using a better mirror coating and a shorter cavity.

Z.L. Liau  
J.N. Walpole  
D.Z. Tsang

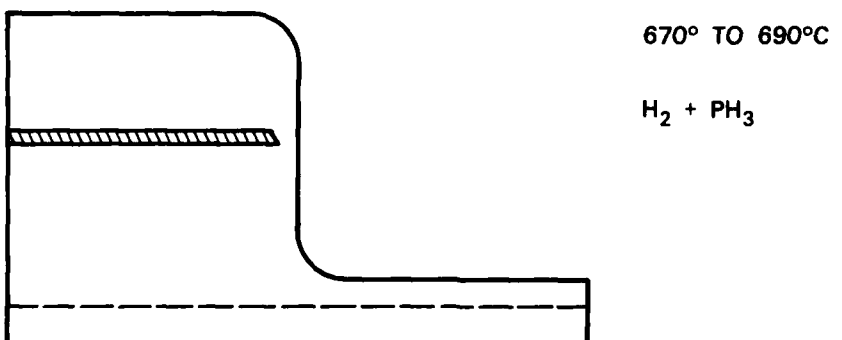
(a) HETEROSTRUCTURE LASER WAFER



(b) SELECTIVE CHEMICAL ETCHING

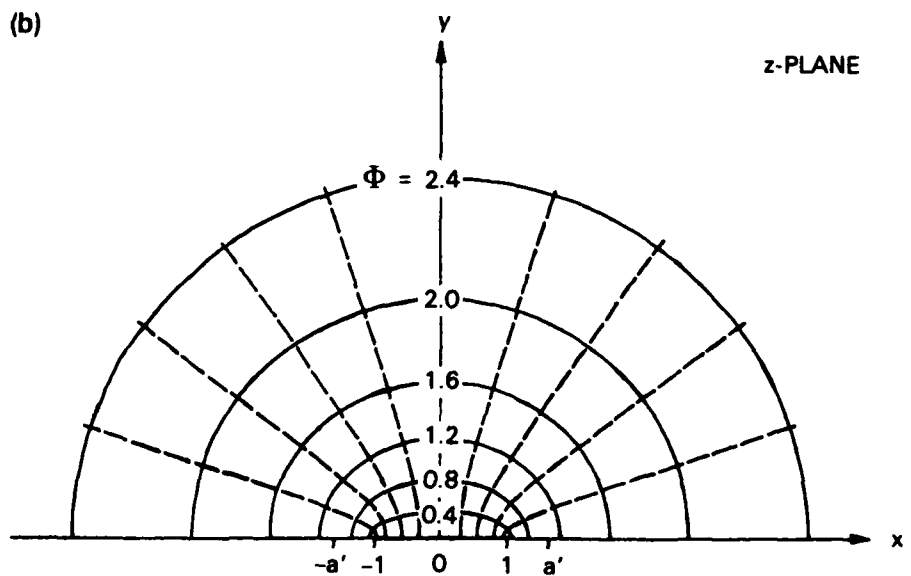
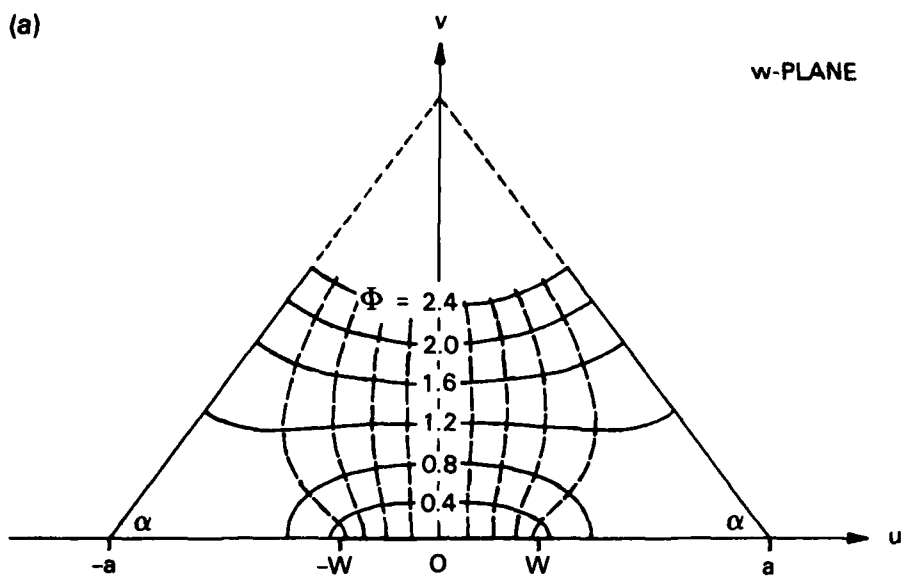


(c) MASS TRANSPORT



135255-N-01

Figure 1-1(a-c). Procedures for formation of transported mirror.



139926-R

**Figure 1-2.** SEM photographs of longitudinal cross sections (a) before and (b) after mass transport.  
In (b), active layer is stained for contrast.

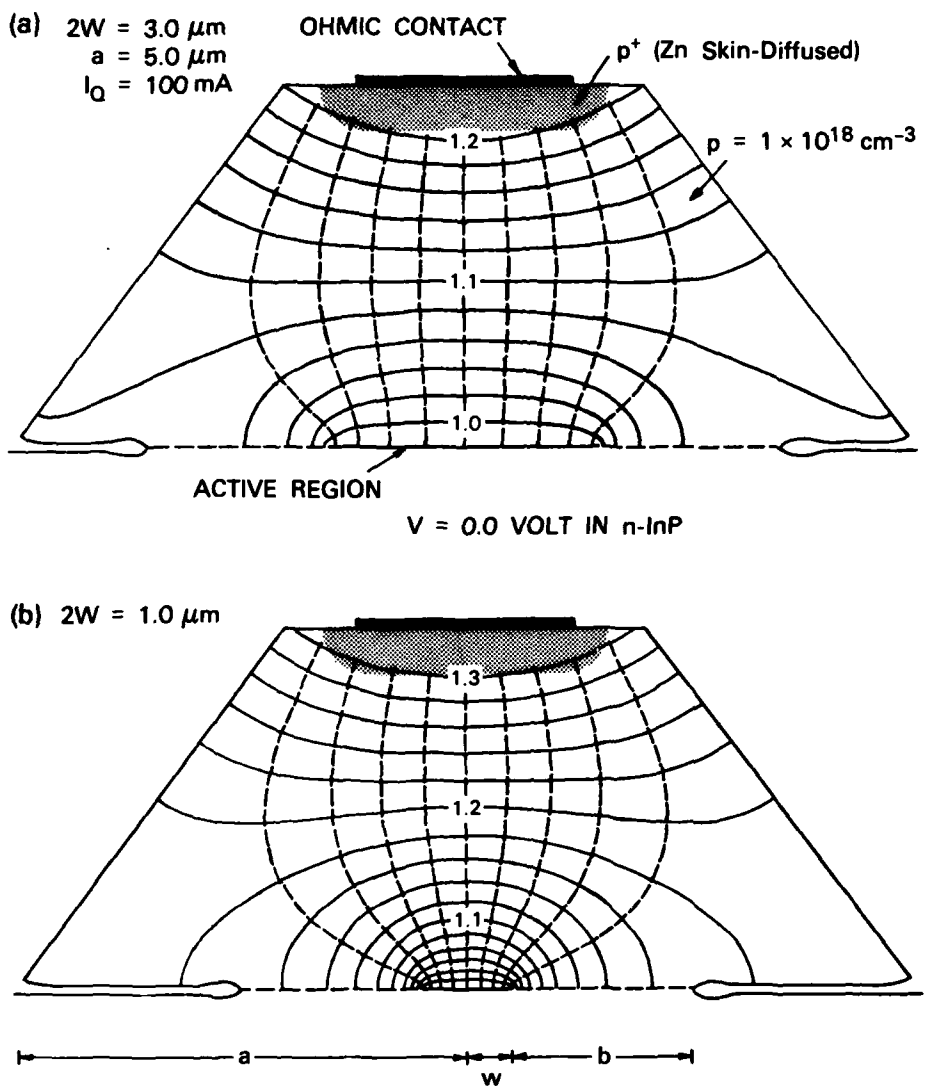


Figure 1-3. SEM photographs showing perspective views of (a) transported and (b) cleaved mirrors. Active layer is stained for contrast.

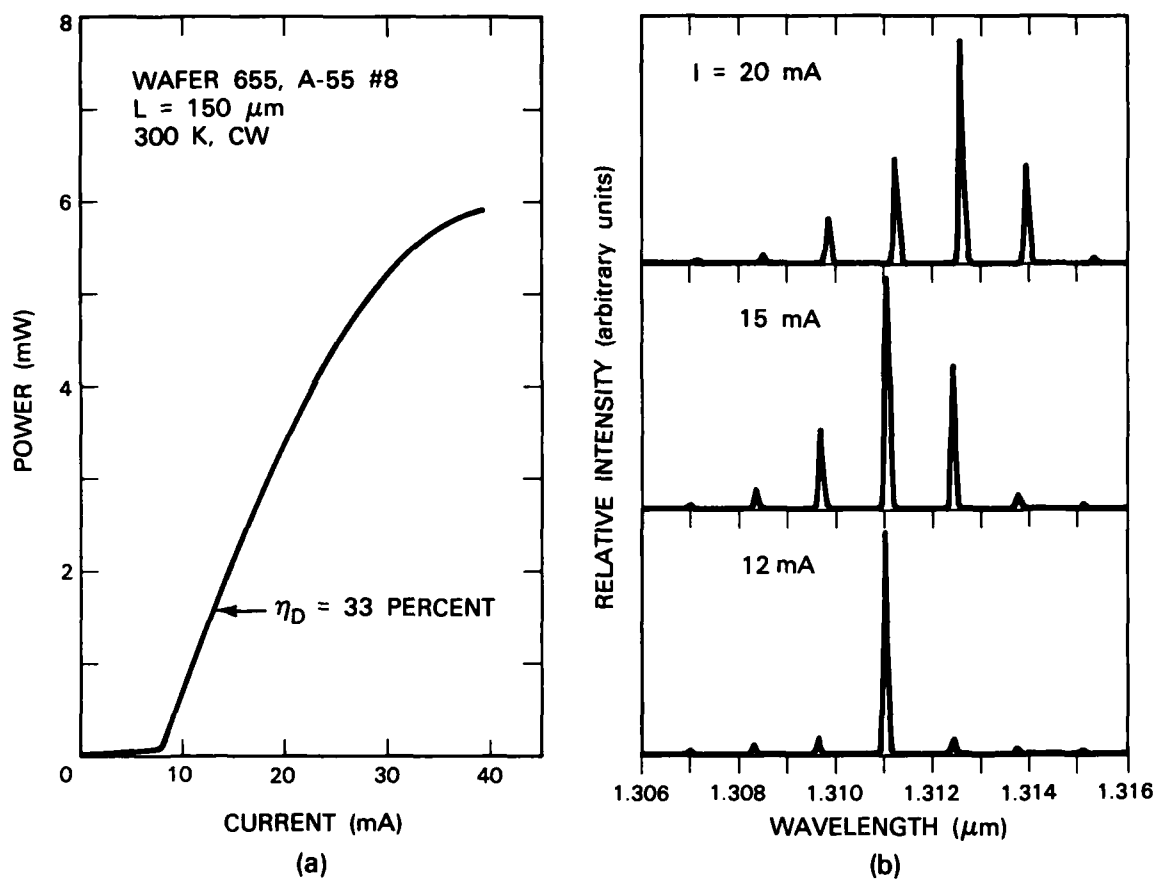


Figure 1-4. (a) Light-current characteristics and (b) emission spectra of a GaInAsP/InP BH laser with a transported mirror.

## 1.2 SIGNAL CORRELATION USING A ONE-DIMENSIONAL ELECTRO-ABSORPTIVE CCD SPATIAL LIGHT MODULATOR

Electrically addressed spatial light modulation (SLM) can be carried out in a GaAs charge-coupled device (CCD) by charge transfer control of the electroabsorption in the individual storage wells. One-dimensional modulator arrays may be utilized in both space- and time-integrating correlators operated as incoherent optical processors. In the space-integrating case, one SLM controlled by the input signal is operated in cascade with a second SLM controlled by a reference waveform. This arrangement yields a single-detector output which is the correlation as a function of time. In the time-integrating correlator, the input signal is carried by the light source while a single SLM with a traveling reference wave controls the output intensity to a detector array. The modulator arrays may be operated with the light

at normal incidence to a CCD with transparent gates or in a guided-wave mode, where the light propagates beneath the gate electrodes and parallel to the surface. The calculated dynamic range is greater for the guided-wave case because of the greater depth of modulation, although the fabrication and optical coupling are more critical. Space-integrating correlator performance is limited by "bleaching" or well-filling by the modulated light, and predicted dynamic ranges are 20 dB for normal-incidence operation and 40 dB for the guided-wave mode. In the time-integrating correlator, saturation of the detector array is limiting, but the 100-percent modulation available in the input optical source yields 35-dB dynamic range for normal-incidence and 55 dB for guided-wave operation.<sup>10</sup>

R.H. Kingston

#### REFERENCES

1. K. Iga and B.I. Miller, IEEE J. Quantum Electron. **QE-18**, 22 (1982), and earlier works cited therein.
2. P.D. Wright, R.J. Nelson, and R.B. Wilson, IEEE J. Quantum Electron. **QE-18**, 249 (1982), and earlier works cited therein.
3. L.A. Coldren, K. Furuya, B.I. Miller, and J.A. Rentschler, IEEE J. Quantum Electron. **QE-18**, 1679 (1982), and earlier works cited therein.
4. S. Adachi, H. Kawaguchi, K. Takahei, and Y. Noguchi, J. Appl. Phys. **52**, 5843 (1981).
5. K. Furuya, L.A. Coldren, B.I. Miller, and J.A. Rentschler, Electron. Lett. **17**, 582 (1981).
6. L.A. Coldren, K. Furuya, and B.I. Miller, J. Electrochem. Soc. **130**, 1918 (1983).
7. Z.L. Liau and J.N. Walpole, Appl. Phys. Lett. **40**, 568 (1982), DTIC AD-A121779.
8. S.E.H. Turley and P.D. Greene, J. Cryst. Growth **58**, 409 (1982).
9. P. Buchmann and A.J.N. Houghton, Electron. Lett. **18**, 850 (1982).
10. R.H. Kingston, Proc. IEEE (to be published).

## 2. QUANTUM ELECTRONICS

### 2.1 RECENT ADVANCES IN SOLID STATE LASERS

The Ti:Al<sub>2</sub>O<sub>3</sub> laser described previously<sup>1,2</sup> has the potential for broad tunability because of the large fluorescence linewidth and the lack of excited-state absorption. In earlier experiments,<sup>2</sup> a Ti:Al<sub>2</sub>O<sub>3</sub> laser, tuned by two intracavity, Brewster-angle, fused silica prisms and pumped by a pulsed dye laser, had demonstrated an operation over the 687- to 821-nm range. Recently, a set of mirrors coated for longer-wavelength operation was used in this system. At a pump energy of 20 mJ (at ~580 nm), the Ti:Al<sub>2</sub>O<sub>3</sub> laser oscillated out to a wavelength of 986 nm which, from previously measured data,<sup>1</sup> is far into the long-wavelength tail of the fluorescence spectrum. The upper limit of the lasing wavelength is longer than expected, and suggests that a more careful examination of the fluorescence spectra of Ti:Al<sub>2</sub>O<sub>3</sub> is required.

The lower limit of the Ti:Al<sub>2</sub>O<sub>3</sub> laser wavelength is determined by a combination of increased absorption from the lower laser level as the wavelength of the zero-phonon line is approached, and of increased scattering losses in the laser crystal at shorter wavelengths. Both effects combine to raise the Ti:Al<sub>2</sub>O<sub>3</sub> laser threshold beyond the pump-laser output level. The 2-cm-long laser crystal used in the long-wavelength measurements described above was doped with ~0.1-percent Ti<sup>3+</sup> and had a scattering loss of ~0.05 cm<sup>-1</sup> at 750 nm. A 3.2-cm-long crystal doped with ~0.02-percent Ti<sup>3+</sup> and having considerably lower scattering losses was used in an experiment to extend the short-wavelength tuning range. The dye laser wavelength was shifted to ~505 nm in order to be more efficiently absorbed by the optically "thinner" crystal. At 18 mJ of pump energy, the shortest wavelength observed was 660 nm; higher pumping levels should permit even shorter wavelengths. The present tuning range spans ~5000 cm<sup>-1</sup>, the longest of any tunable laser.

A series of measurements<sup>3</sup> performed on various host crystals for the Nd<sup>3+</sup> ion indicated that Cr<sup>3+</sup>-sensitized Gd<sub>3</sub>Sc<sub>2</sub>Ga<sub>3</sub>O<sub>12</sub> (GSGG) is several times more efficient under flashlamp-pumped conditions than the more common host, Y<sub>3</sub>Al<sub>5</sub>O<sub>12</sub> (YAG). However, the data showed a slope (differential power) efficiency for the Nd:Cr:GSGG laser of 2.5 percent, which can be achieved by a well-designed Nd:YAG laser. To determine if high absolute efficiencies can be obtained from lasers using the sensitized garnet crystal, several experiments were carried out employing a 5-mm-diameter by 75-mm-long laser rod in an efficient optical pumping cavity. The doping level was approximately 1 percent for both the Nd<sup>3+</sup> and Cr<sup>3+</sup> ions (see Reference 4). The pump source, a 400-Torr xenon flashlamp with a 4-mm bore and 6.25-cm arc length, was driven by a resonantly charged LC discharge circuit with a 55-μF capacitance and 82-μH inductance. The water-cooled pump cavity<sup>5</sup> was constructed of a samarium-doped glass tube with a diffuse reflector coated on the outer surface of the tube.

Figure 2-1 presents the input-output energy curves for the system running at a repetition rate of 20 Hz. The laser cavity for these results consisted of two flat mirrors spaced 33 cm

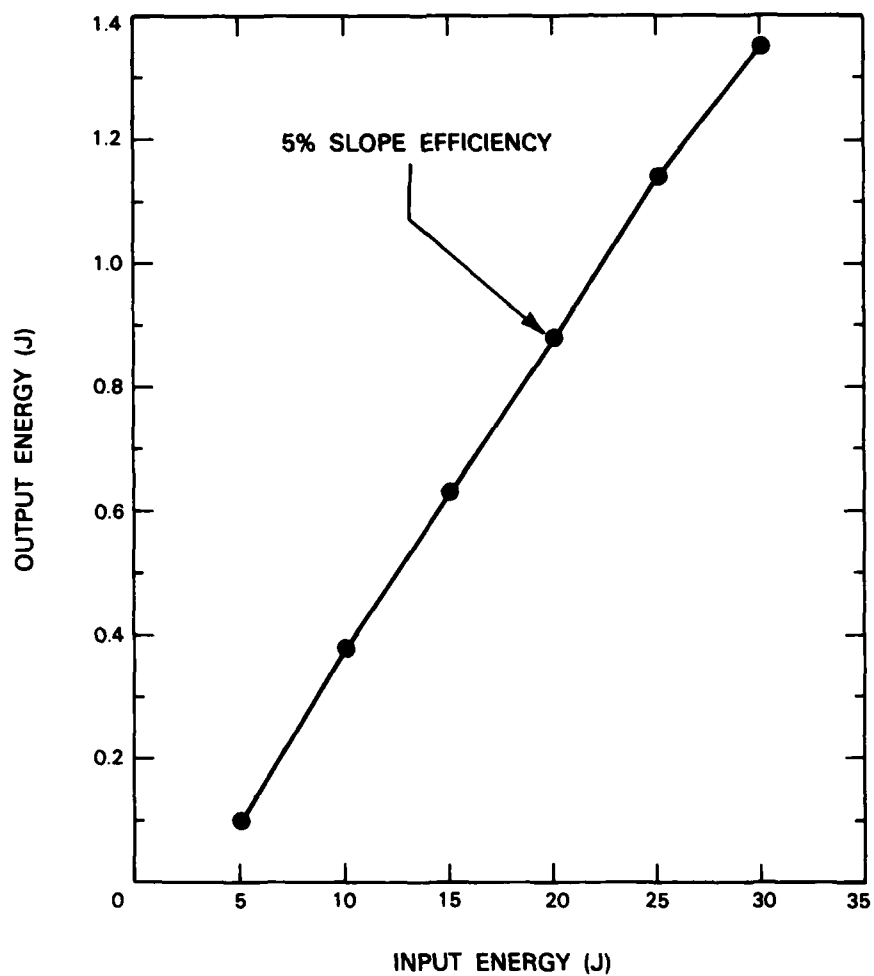


Figure 2-1. Output vs input energy at a 20-Hz repetition rate from a flashlamp-pumped Nd:Cr:GSGG laser.

apart with an output coupling of 50 percent; the threshold was 2.6 J. When the output coupling was reduced to 20 percent, the threshold dropped to  $\sim$ 1.2 J, indicating that the crystal losses were relatively low. The laser performance as a function of repetition rate is shown in Figure 2-2. The rolloff at the highest rate is due to the limited recharging rate of the power supply. Up to 40 W of average power at a 30-Hz rate was observed at  $\sim$ 32-J/pulse input energy. Higher outputs could not be obtained because of the limited thermal rating of the pump cavity.

The slope and overall efficiencies of a standard Nd:YAG laser rod in the same pump cavity and with the same pump lamp are 2.5 and 2 percent, respectively.<sup>6</sup> Thus, the Nd:Cr:GSGG laser, with slope and overall efficiencies of 5 and 4.5 percent, respectively, was

138562-N

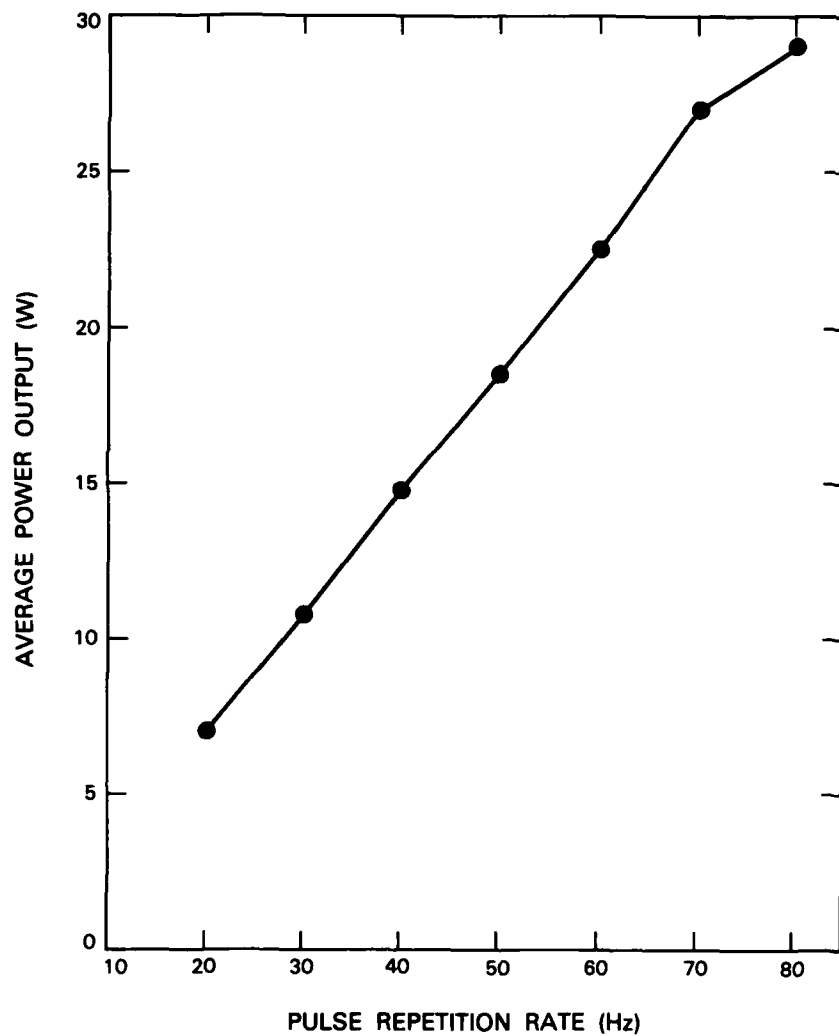


Figure 2-2. Average power output vs pulse repetition rate for Nd:Cr:GSGG laser at 10-J/pulse input level.

significantly more efficient than YAG when both lasers operated under more optimal conditions than previously reported. Adjustments to the pump-lamp parameters and the rod doping levels may yield even higher efficiencies from the Nd:Cr:GSGG laser.

P.F. Moulton

## 2.2 HIGH AVERAGE POWER MODE-LOCKED OPERATION OF Co:MgF<sub>2</sub> AND Ni:MgF<sub>2</sub> LASERS

Vibronic lasers based on Co:MgF<sub>2</sub> and Ni:MgF<sub>2</sub> crystals have proven to be versatile, broadly tunable CW and pulsed sources of infrared radiation.<sup>7,8</sup> We report here the first

tunable, CW mode-locked operation of these lasers. The Co:MgF<sub>2</sub> and Ni:MgF<sub>2</sub> materials have large gain bandwidths of 2000 and 400 cm<sup>-1</sup>, respectively. The more widely tunable Co:MgF<sub>2</sub> system is especially interesting, having demonstrated CW tunability from 1.55 to 2.15 μm. These systems have small gain cross sections (~10<sup>-21</sup> cm<sup>2</sup>) and therefore require the use of intracavity modulation for practical mode-locking.

Initial pulse-width measurements were made using a laser system which consisted of a three-mirror cavity containing a Brewster cut Co:MgF<sub>2</sub> (or Ni:MgF<sub>2</sub>) crystal cooled in a liquid-nitrogen Dewar, a birefringent tuning element, and an acousto-optic loss modulator. The laser was longitudinally pumped by a CW 1.33-μm Nd:YAG laser, and average mode-locked output powers up to 100 mW were obtained. Autocorrelation pulse-width measurements showed that the Co:MgF<sub>2</sub> produced pulses between 36 and 100 ps over the 1.65- to 2.01-μm wavelength range, while the Ni:MgF<sub>2</sub> laser generated pulses between 23 and 50 ps over the 1.61- to 1.73-μm range. The variation of pulse width with wavelength is influenced by structure in the gain vs wavelength curve, and by weak etalon effects within the cavity. Calculations<sup>9</sup> show these systems capable of producing pulses as short as 10 ps. Elimination of unwanted etalon effects and improvements in system stability should make this possible.

A Co:MgF<sub>2</sub> laser has also been demonstrated with average mode-locked powers of up to 2 W and pulse widths similar to those produced by the lower power laser. This laser had a two-mirror cavity with a large mode waist in the crystal, which allowed pumping with a high-power, multiple-transverse-mode Nd:YAG laser.

The lasers described above have produced pulses shorter than most similar actively mode-locked lasers, such as the CW Nd:YAG laser. The high power capability of these lasers makes possible extended tunability by nonlinear techniques such as frequency doubling and mixing. These lasers should be useful for studies of ultrahigh-speed properties of semiconductor devices and optical fibers.

B.C. Johnson      P.F. Moulton  
M. Rosenbluh†      A. Mooradian

### 2.3 TEMPERATURE DEPENDENCE OF QUANTUM FLUCTUATION LINewidth BROADENING IN GaAlAs DIODE LASERS

Measurements of the spectral lineshape as a function of power have been carried out from room temperature down to 1.7 K in order to understand the influence of fundamental quantum fluctuations on the spectral characteristics of single-frequency, CW, GaAlAs diode lasers. Such information is important for use of these lasers in heterodyne communications and fiber optical sensors. Previous measurements<sup>10</sup> of linewidth as a function of power at 273, 195, and 77 K agreed well with a model<sup>11</sup> for the linewidth in which spontaneous

---

† Permanent address: Physics Department, Bar Ilan University, Ramat Gan, Israel.

emission caused fluctuations in both the phase and amplitude of the laser field. A power-independent contribution to the laser linewidth was also observed<sup>12</sup> whose magnitude increased from 1.9 MHz at 273 K to 8.4 MHz at 77 K, and was consistent with a phenomenological model involving electron number fluctuations in the gain volume that produced fluctuations in the resonant frequency of the passive cavity. An alternative theory for this power-independent broadening by Vahala and Yariv<sup>13</sup> attributed the phenomenon to electron occupation fluctuations rather than number fluctuations. Their model, however, predicts a linewidth which approaches zero as the temperature approaches zero. This is in sharp contrast with measurements carried out at temperatures down to 1.7 K in which the power-independent linewidth increases to about 40 MHz at 1.7 K, as seen in Figure 2-3. The behavior at 1.7 K is consistent with the phenomenological model of Reference 12, just as the observed power-dependent linewidth is consistent with the model of Reference 11.

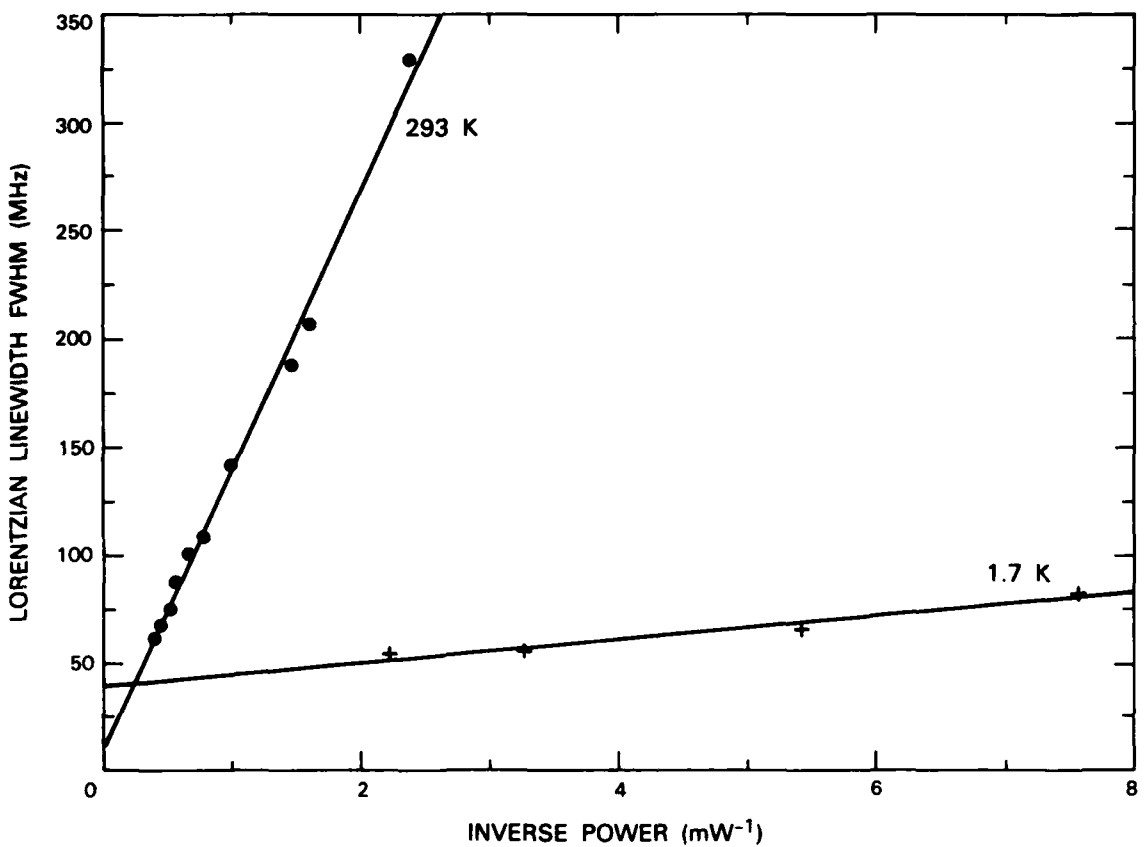


Figure 2-3. Linewidth of a CW single-frequency Mitsubishi TJS laser at 293 and 1.7 K.

The quantum fluctuations in both the field intensity and phase also produce sidebands at the relaxation oscillation resonance<sup>14</sup> as the perturbed field returns to steady state. The

behavior of these sidebands as a function of power, temperature, and multimode operation of the devices has been studied here. Sidebands due only to fundamental quantum fluctuations occur when devices operate in a single longitudinal mode and exhibit an expected integrated intensity relative to the main peak intensity which is linear with reciprocal power in the main mode, as is shown in Figure 2-4. Multi-transverse-mode operation results in a substantial increase over the fundamental sideband intensities, with up to third-order sidebands being observed. Figure 2-5 shows the output spectrum as recorded with a Fabry-Perot spectrometer of the output of a single-mode GaAlAs diode laser at 1.7 K for various power levels. The sideband resonances at about 150 MHz are approximately ten times lower in frequency than those measured at room temperature for comparable power levels in the same device.

J. Harrison  
A. Mooradian

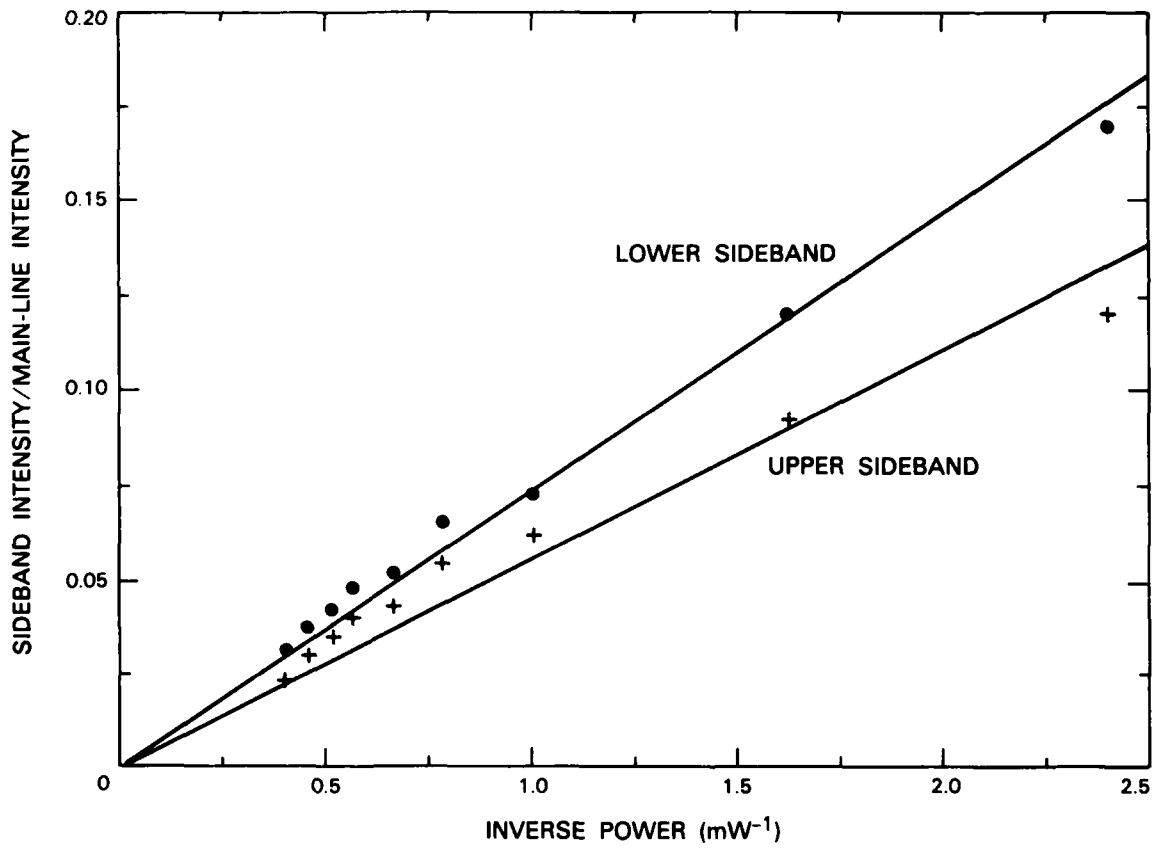


Figure 2-4. Integrated upper- and lower-sideband intensities relative to main frequency intensity for a Mitsubishi TJS CW, single-frequency diode laser at 20°C.

13855-N

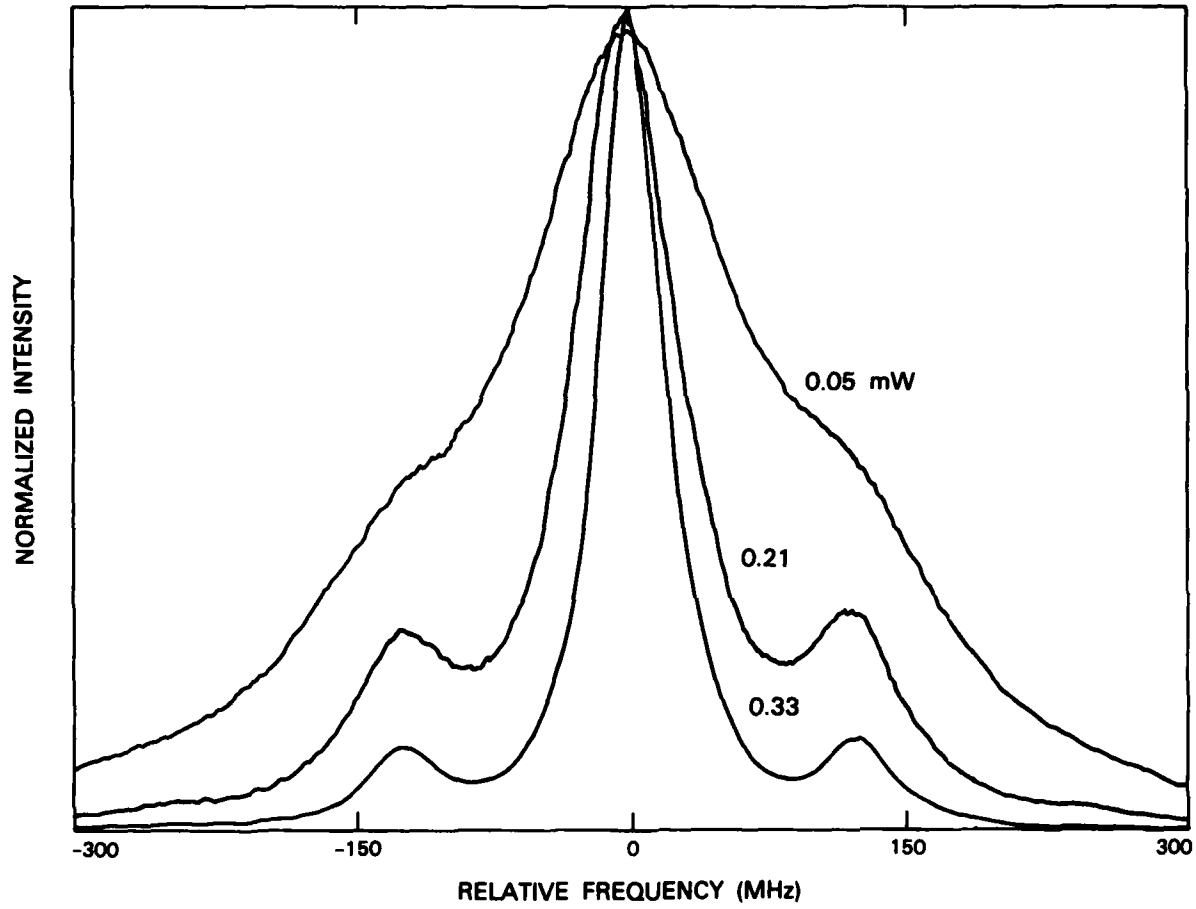


Figure 2-5. Fabry-Perot spectrum of Mitsubishi TJS diode laser at 1.7 K for three output-power levels.

## REFERENCES

1. Solid State Research Report, Lincoln Laboratory, M.I.T. (1982:3), pp. 15-21, DTIC AD-A124305/4.
2. *Ibid.* (1983:3), p. 17.
3. E.V. Zharikov *et al.*, Sov. J. Quantum Electron. **12**, 1652 (1982).
4. The material was grown commercially by Airtron, Incorporated, New Jersey.
5. Kigre, Incorporated, Ohio, Model YW-525.
6. A. Schwalbe, Jr. (personal communication).
7. P.F. Moulton and A. Mooradian, Appl. Phys. Lett. **35**, 838 (1979), DTIC AD-A085795/3.
8. P.F. Moulton, IEEE J. Quantum Electron. **QE-18**, 1185 (1982).
9. D.J. Kuizenga and A.E. Siegman, IEEE J. Quantum Electron. **QE-6**, 691 (1970).
10. D. Welford and A. Mooradian, Appl. Phys. Lett. **40**, 865 (1982).
11. C.H. Henry, IEEE J. Quantum Electron. **QE-18**, 259 (1982).
12. D. Welford and A. Mooradian, Appl. Phys. Lett. **40**, 560 (1982), DTIC AD-A121778.
13. K. Vahala and A. Yariv, Appl. Phys. Lett. **43**, 140 (1983).
14. B. Daino, P. Spano, M. Tamburini, and S. Piazzolla, IEEE J. Quantum Electron. **QE-19**, 266 (1983); K. Vahala, C. Marder, and A. Yariv, Appl. Phys. Lett. **42**, 211 (1983).

### 3. MATERIALS RESEARCH

#### 3.1 ROLE OF OXYGEN IN ZONE-MELTING RECRYSTALLIZATION OF Si FILMS ON SiO<sub>2</sub>-COATED Si SUBSTRATES

In previous reports,<sup>1-5</sup> we described a graphite-strip-heater technique for obtaining large-area, high-quality silicon films on SiO<sub>2</sub> by zone-melting recrystallization (ZMR). A typical sample is prepared by coating a Si wafer with a 1-μm-thick thermally grown SiO<sub>2</sub> layer, a 0.5-μm-thick poly-Si layer deposited by low-pressure chemical-vapor deposition (LPCVD), and an encapsulating layer consisting of a 2-μm layer of CVD SiO<sub>2</sub> and a 30-nm layer of sputtered Si-rich Si<sub>3</sub>N<sub>4</sub>. A narrow molten zone produced in the poly-Si by a movable upper strip heater is translated across the sample, leaving a recrystallized Si film. Almost all our ZMR films (as well as those prepared elsewhere, regardless of the heat source used<sup>6-9</sup>) contain low-angle sub-boundaries (see Figure 3-1). Sub-boundaries are typically formed in regions where the solid-liquid interface at the trailing edge of the molten Si zone is strongly

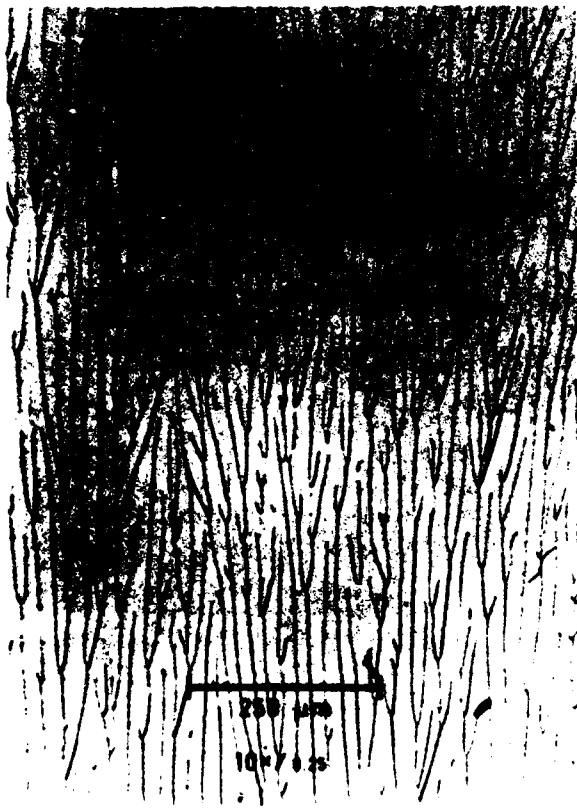
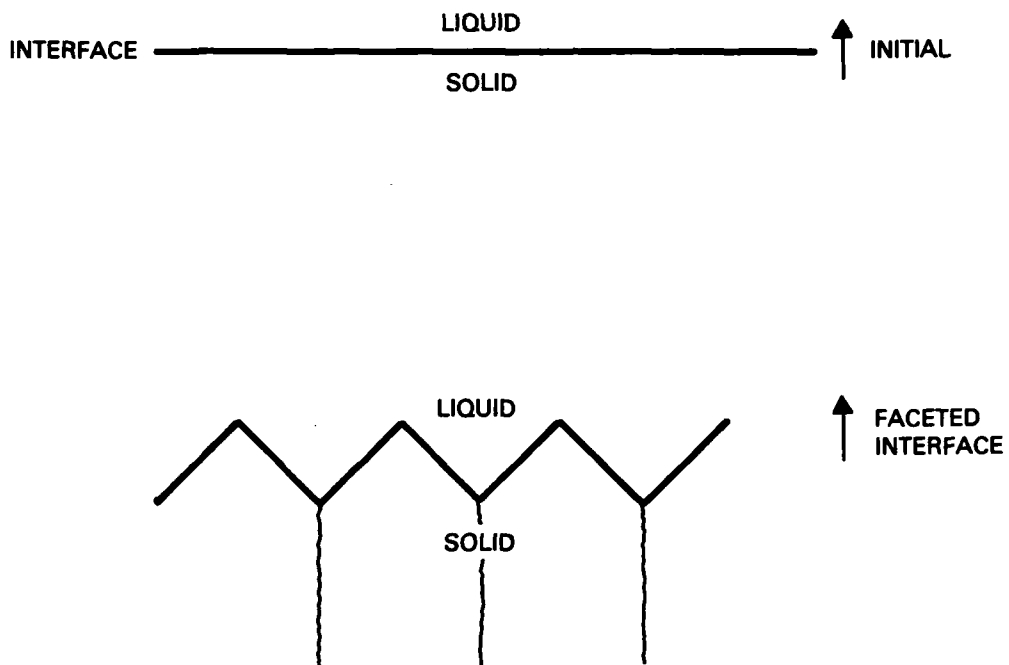


Figure 3-1. Optical micrograph of ZMR Si film that has been etch-delineated to show sub-boundaries. Upper graphite heater was scanned in direction from top to bottom of micrograph.

faceted by [111] planes, with the sub-boundaries originating at the inner corners of the facets (see Figure 3-2). We now report an investigation of ZMR films by secondary-ion mass spectrometry (SIMS) analysis, which shows that oxygen is strongly concentrated along the sub-boundaries. This observation suggests the possibility that faceting, and therefore sub-boundary formation, may result from constitutional supercooling that occurs because of the presence of oxygen introduced into the molten zone by partial dissolution of the SiO<sub>2</sub> layers bordering the Si film. (Both the SIMS results and other observations indicate that two other nonplanar interface morphologies — dendritic and cellular — are sometimes present during recrystallization. These probably have the same basic origin as the faceted morphology.)



**Figure 3-2.** Schematic diagram showing an initially planer solid-liquid interface that becomes faceted, causing sub-boundaries.

The ZMR Si films were analyzed for oxygen, carbon, copper, hydrogen, and nitrogen with a Cameca IMS-3f SIMS instrument at the Solar Energy Research Institute. Figure 3-3 shows depth profiles obtained for a sample from which the encapsulating layer was removed by chemical etching. The high initial concentrations of oxygen, carbon, copper, and hydrogen are probably due to post-etching surface contamination. The oxygen profile in the Si film is asymmetric, exhibiting a substantial rise in concentration as the lower SiO<sub>2</sub> interface is approached, while the other profiles do not appear to have any noteworthy features. Figure 3-4 is a SIMS map showing the lateral distribution of oxygen in a region of the Si

134405-N

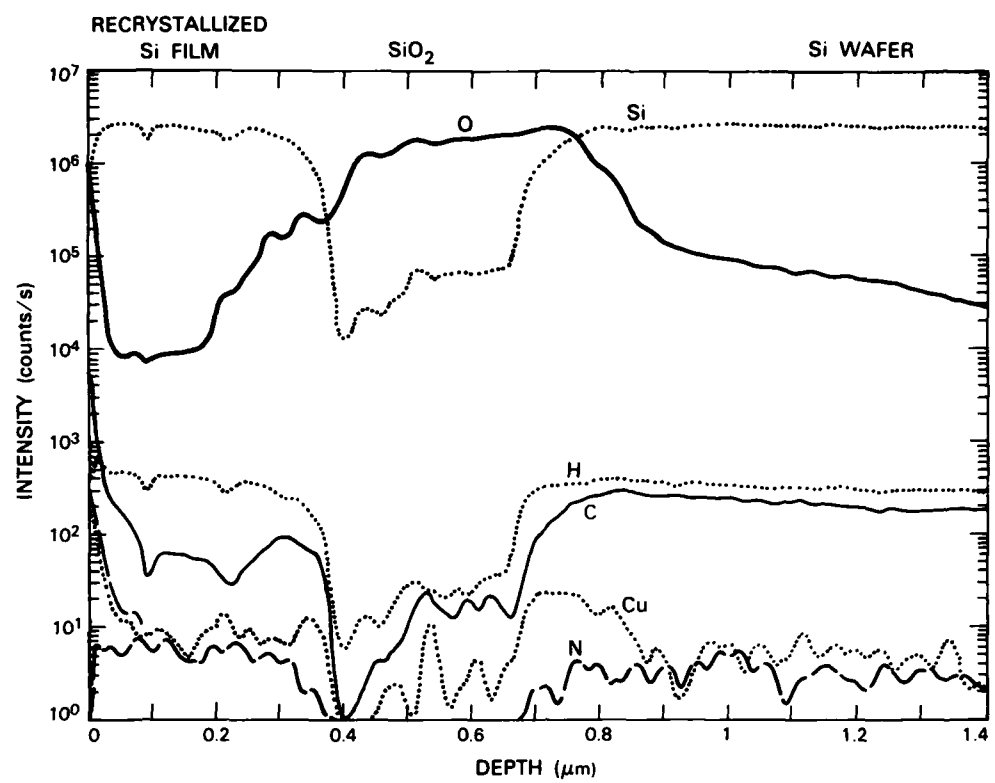
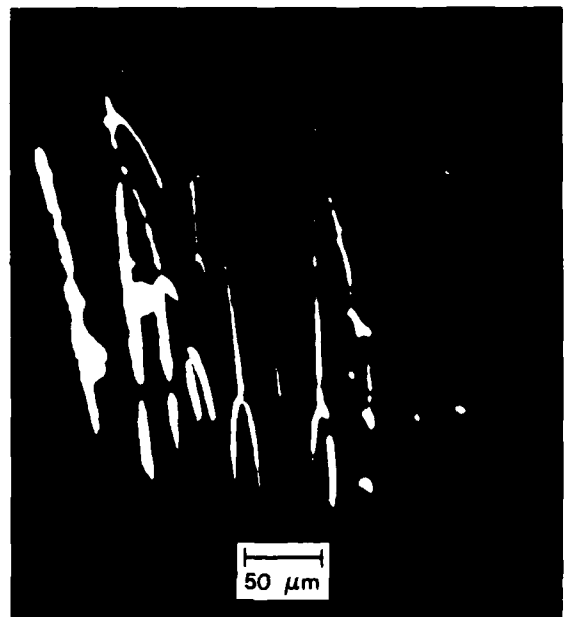
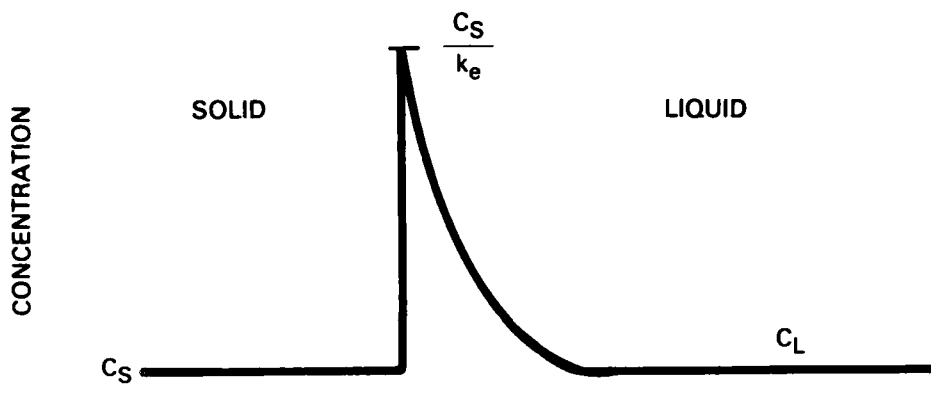


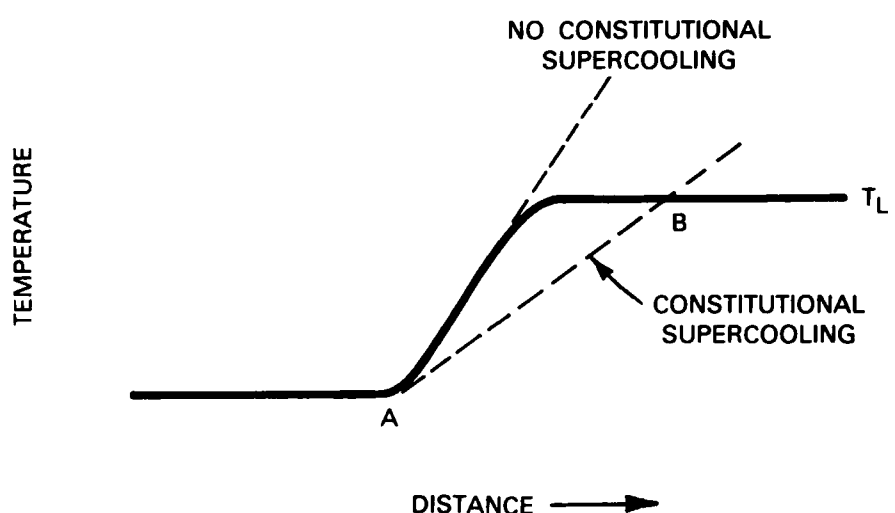
Figure 3-3. SIMS profile of ZMR sample that had encapsulating layer removed.

Figure 3-4. Oxygen map obtained by SIMS, showing oxygen concentrated along sub-boundaries.





(a)



(b)

**Figure 3-5.** (a) Schematic diagram showing oxygen concentration as a function of distance in vicinity of solid-liquid interface. (b) Schematic diagram showing liquidus temperature  $T_L$  and melt temperatures  $T$  (dashed lines) as functions of distance in vicinity of solid-liquid interface.

134433-N-02

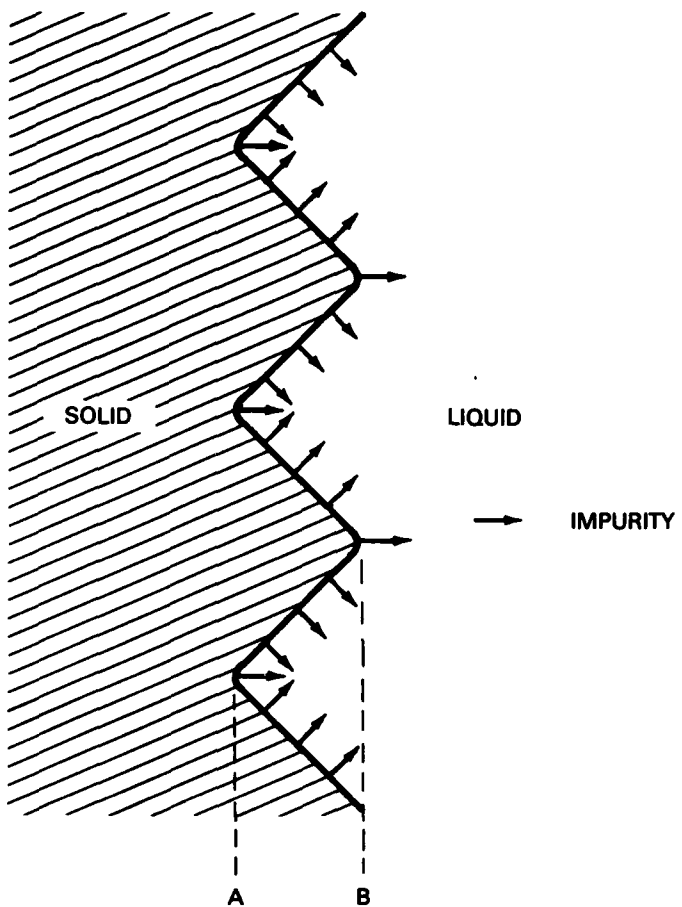
film near the lower  $\text{SiO}_2$  interface. The features observed have the characteristic configuration of the sub-boundaries, showing clearly that oxygen is concentrated there. For the other impurities, the signal-to-noise ratios were too low to permit mapping.

The segregation of oxygen along the sub-boundaries can be attributed to its preferential incorporation in these locations during solidification of the molten zone, since the depth profiles would be symmetric if post-solidification diffusion of oxygen from the upper and lower  $\text{SiO}_2$  layers was a major factor. Although the zone scanning rate is about 1 mm/s, dissolution of  $\text{SiO}_2$  and subsequent diffusion of oxygen in the melt occur so rapidly that for films only  $\sim 0.5 \mu\text{m}$  thick the molten zone becomes saturated with oxygen at the equilibrium solubility limit, which is estimated to be  $\sim 3.5 \times 10^{18} \text{ cm}^{-3}$  (see Reference 10). For oxygen in Si the equilibrium distribution coefficient ( $k_e = C_S/C_i$ , where  $C_S$  and  $C_i$  are the concentrations of oxygen in the solid and liquid, respectively, at the interface) is between 0.2 and 0.3 (see Reference 11). At the trailing edge of the molten zone, therefore, oxygen is rejected from the solid into the melt. At the ZMR scanning rates, diffusion of oxygen is not rapid enough for the liquid to reach equilibrium in the direction normal to the interface. Therefore,  $C_i$  becomes greater than  $C_L$ , the concentration of oxygen in the bulk of the liquid away from the interface, as shown in Figure 3-5(a). Accordingly,  $C_S = k_e C_i$  is greater than  $k_e C_L$ . In fact,  $C_S \approx C_L$  on the average, i.e., the effective distribution coefficient ( $k_{\text{eff}} = C_S/C_L$ ) is approximately unity.<sup>11,12</sup>

For a planar growth interface,  $C_i$  and therefore  $C_S$  will be the same all along the interface. Along a faceted interface, however, rejection of oxygen into the liquid during solidification leads to local variations in  $C_i$ , with  $C_i$  highest at the inner corners, as shown by the schematic diagram of Figure 3-6. Since the sub-boundaries originate at these corners,  $C_S$  will be highest along the sub-boundaries, as observed by SIMS analysis, although  $C_S$  will still be equal to  $C_L$  on the average.

The explanation just given for the segregation of oxygen along the sub-boundaries is based on the two independent observations that the growth interface is faceted and that  $k_e$  for oxygen in Si is less than unity. We now suggest the possibility that there is actually a direct relationship between these observations, in particular that faceting and therefore sub-boundary formation may result from constitutional supercooling<sup>13</sup> resulting from the rejection of oxygen at the growth interface.

For an impurity with  $k_e < 1$ , the increase in concentration from  $C_L$  to  $C_i$  within the interface region leads to a corresponding decrease in the liquidus temperature  $T_L$ , which is shown by the solid line in Figure 3-5(b). Whether or not constitutional supercooling will occur depends on the temperature gradient in the liquid. If this gradient is larger than the gradient for the upper dashed line in Figure 3-5(b), a planar interface will be stable with respect to small fluctuations. If the gradient in the liquid is smaller, as shown for example by the lower dashed line in Figure 5(b), then in the region between A and B the liquid will be supercooled. In this case the interface will be unstable, because any portion that advances beyond A will continue to advance until it reaches B. In a process such as ZMR, there are many possible sources for interface fluctuations. In fact, it would be extremely difficult (if not impossible) to eliminate all these fluctuations.



134434-N-01

**Figure 3-6.** Schematic diagram showing rejection of impurities from the solid into the liquid at a faceted interface, causing an increase in impurity concentration at inner corners of interface.

Growth interfaces that are unstable because of constitutional supercooling can exhibit a variety of morphologies, depending on the thermal distribution. Faceting is one such morphology. In Ga-doped Ge, for example, constitutional supercooling leads to the formation of a faceted interface composed of  $\{111\}$  planes.<sup>14</sup> As noted above, the faceted interfaces in ZMR Si films are also composed of  $\{111\}$  planes.<sup>4</sup> We believe that there is a good possibility that constitutional supercooling also leads to the faceting (and therefore sub-boundary formation) in these films. If so, it seems probable that oxygen is the impurity responsible, although the evidence is by no means conclusive. Perhaps the most persuasive argument for this assignment is that it would account for the fact that sub-boundaries are almost universally observed in ZMR Si films, since all such films are in contact with  $\text{SiO}_2$  layers and should be saturated with oxygen.

Because sub-boundaries are the most prominent defects in ZMR films, their elimination is the objective of much of the current work on the ZMR process. If they are caused by constitutional supercooling, it should be possible to eliminate them if experimental conditions can be found that prevent constitutional supercooling. Even if this cannot be accomplished over the whole area of unseeded or singly seeded films, sub-boundaries can be eliminated by the means of multiple seeding. In early experiments using seeds spaced 50  $\mu\text{m}$  apart, we obtained<sup>2</sup> sub-boundary-free regions several tens of square millimeters in area, and it should be possible to obtain such regions covering an entire wafer, probably with significantly larger seed spacings.

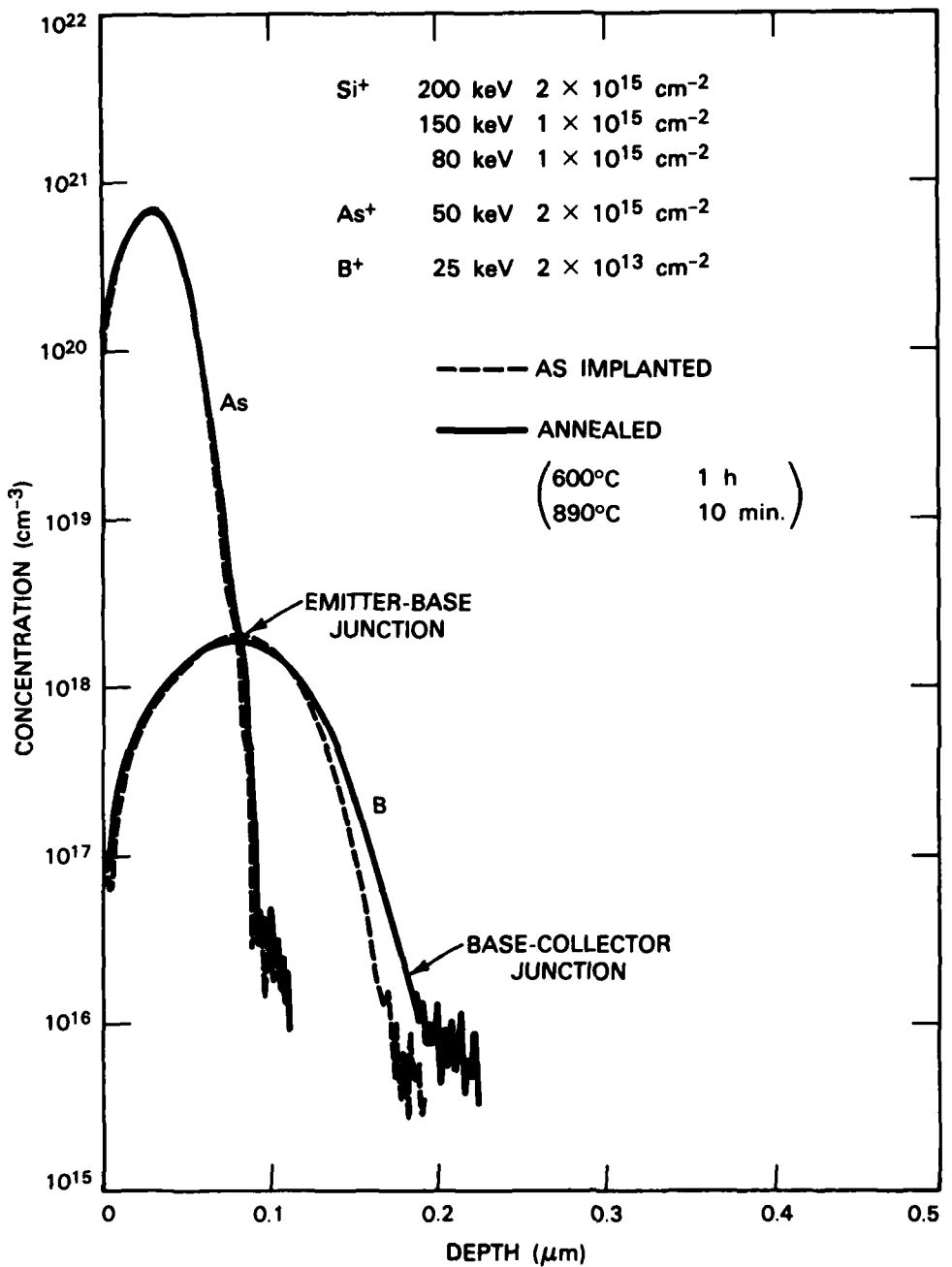
J.C.C. Fan  
B-Y. Tsaur  
C.K. Chen

### 3.2 TRIPLE ION-IMPLANTATION TECHNIQUE FOR FORMATION OF SHALLOW npn BIPOLAR TRANSISTOR STRUCTURES IN SILICON

In the development of increasingly complex VLSI circuits, as lateral device dimensions are decreased to achieve higher levels of integration it also becomes necessary to reduce vertical dimensions in order to maintain desirable device performance.<sup>15</sup> Recent demonstrations have shown that shallow p<sup>+</sup>/n junctions, with depths of the order of 0.1  $\mu\text{m}$  or less, can be formed in Si by a dual ion-implantation technique.<sup>16-18</sup> In this technique, B is introduced into an n-type Si wafer by implantation of low-energy B<sup>+</sup> ions, but only after implantation of Si<sup>+</sup> ions has been used to produce an amorphous Si layer that prevents B<sup>+</sup> ion channeling. Subsequent thermal annealing, which causes recrystallization of the amorphous layer by solid-phase epitaxy (SPE), results in complete electrical activation of the implanted B atoms, without appreciable redistribution, to form the shallow p<sup>+</sup> region.

In this report, we describe a technique that has been developed for preparing high-quality, shallow npn structures for bipolar transistors by the addition of another implantation step to the dual implantation procedure. In this triple implantation technique, the initial Si<sup>+</sup> implantation into an n-type wafer is followed by successive low-dose B<sup>+</sup> and high-dose As<sup>+</sup> implantations into the amorphous Si layer. Thermal annealing is then used to recrystallize this amorphous layer and activate the B and As dopants to form the base and emitter regions, both of which are about 0.1  $\mu\text{m}$  wide. The same procedure has been applied to samples prepared by coating Si wafers with a poly-Si film. For these samples the final structure has a poly-Si emitter contact, since SPE regrowth of the region that was initially polycrystalline is prevented by the presence of native oxide at the original interface between this region and the single-crystal wafer. This structure was investigated because high current gain has been demonstrated for bipolar devices with a poly-Si emitter contact.<sup>19</sup>

The substrates used were either single-crystal n-type Si(100) wafers with 0.3- $\Omega\text{-cm}$  resistivity, or such wafers coated with a 0.09- $\mu\text{m}$ -thick poly-Si film formed by low-pressure chemical-vapor deposition (LPCVD). Both types of substrates were first implanted with Si<sup>+</sup> ions at energies of 200, 150, and 80 keV to produce an amorphous Si layer estimated to be



124861-N-02

Figure 3-7. As and B depth profiles obtained by SIMS analysis of triply implanted Si(100) samples before and after annealing.

~0.35  $\mu\text{m}$  thick. The base and emitter implantations were then performed with 25-keV  $\text{B}^+$  ions and a much heavier dose of 50-keV  $\text{As}^+$  ions, respectively. The implanted samples were annealed in a quartz-tube furnace with flowing  $\text{Ar}/\text{H}_2$  ambient, first at 600°C to recrystallize the amorphous layer and then at a higher temperature to increase dopant activation and reduce residual defect density.

After implantation and annealing, a Si(100) sample and a poly-Si/Si(100) sample were examined by transmission electron microscopy (TEM). In both cases, the TEM micrographs show that a narrow zone with a high density of defects, which can be identified as dislocation loops, is located at the estimated depth of the initial amorphous-crystalline interface obtained after  $\text{Si}^+$  implantation. Above this zone is a single-crystal region that is almost free of defects. For the Si(100) sample, this region extends to the surface. For the poly-Si/Si(100) sample, above the single-crystal region is a polycrystalline region (of the same thickness as the initial poly-Si film) that extends to the surface. In both cases the locations of the emitter-base and base-collector junctions, as determined from the results of SIMS analysis described below, lie within the single-crystal region.

Sheet-resistance measurements were made on Si(100) samples that were implanted with  $\text{Si}^+$ ,  $\text{B}^+$ , and  $\text{As}^+$  and then annealed, or were treated in the same manner but without  $\text{As}^+$  implantation. The measured resistance values are approximately 80 and 1000  $\Omega/\square$ , respectively, which correspond to essentially complete activation of As in the first case and B in the second case.

Figure 3-7 shows the As and B concentration profiles determined by SIMS analysis of triply implanted Si(100) samples before and after annealing. Both as-implanted profiles are in good agreement with the profiles calculated from published range data.<sup>20</sup> Annealing produced virtually no change in the As profile, and only a slight broadening of the B profile. If complete electrical activation is assumed for both As and B, the emitter-base junction depth and the base width are found to be 0.09 and 0.10  $\mu\text{m}$ , respectively. The B concentration at the emitter-base junction is  $2 \times 10^{18} \text{ cm}^{-3}$ . Such a high concentration is necessary for narrow-base transistors in order to prevent collector-emitter punchthrough, and to sustain an adequate collector-emitter bias voltage.<sup>15</sup>

Figure 3-8 shows the As and B concentration profiles determined by SIMS analysis of poly-Si/Si(100) samples before and after annealing. For these samples, the temperature of the second annealing step was increased in order to produce sufficient indiffusion so that the emitter-base junction would be formed within the single-crystal region obtained by recrystallization. On the basis of the post-annealing profiles, this junction is located at a depth of 0.08  $\mu\text{m}$  below the poly-Si/single-crystal interface, the B concentration at the junction is  $2 \times 10^{18} \text{ cm}^{-3}$ , and the base width is 0.09  $\mu\text{m}$ . Within the poly-Si region the B profile is hardly changed by annealing, but the As concentration has become quite uniform, probably as a result of grain-boundary diffusion.<sup>21</sup> For complete As and B activation, this

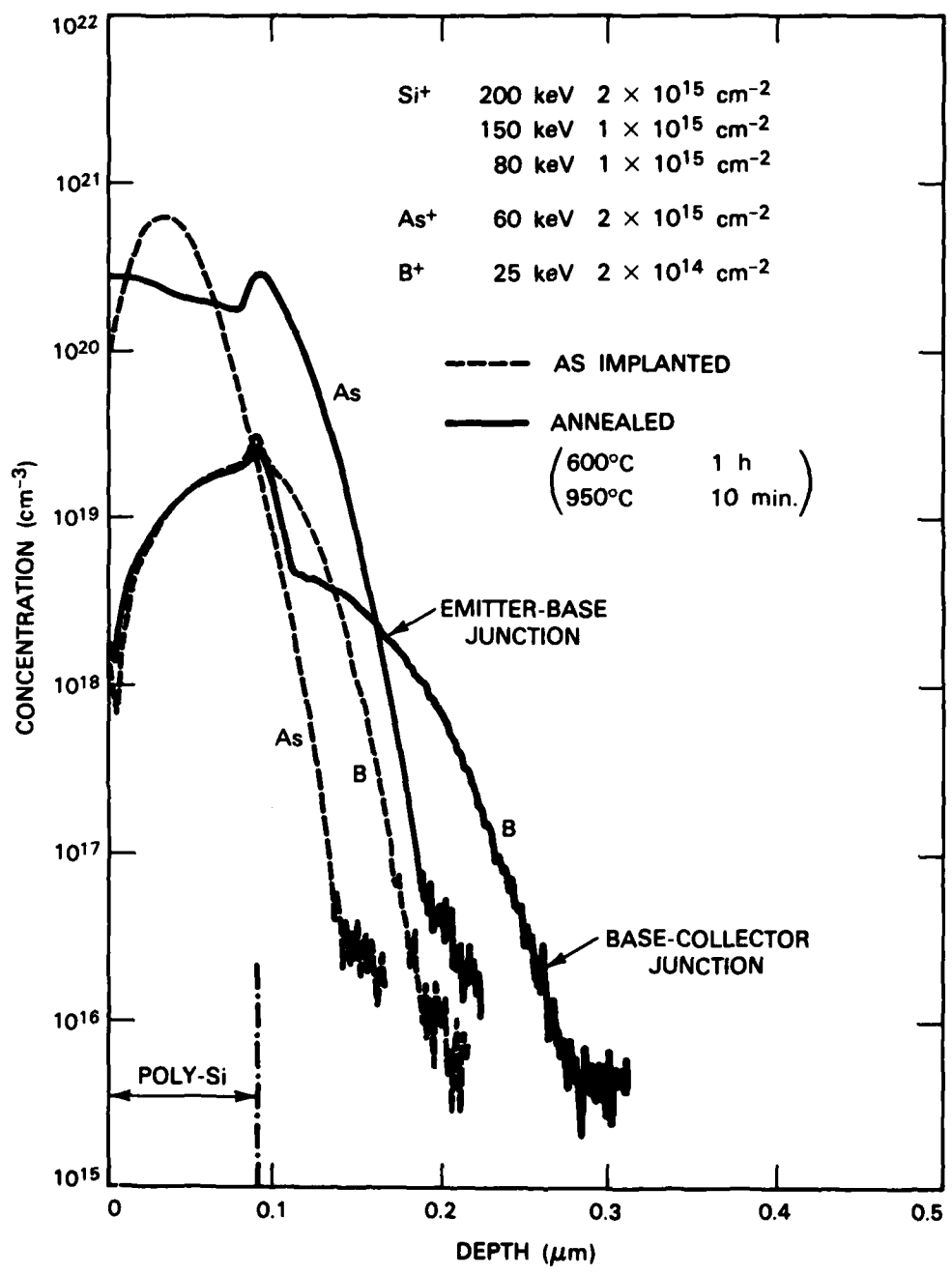


Figure 3-8. As and B depth profiles obtained by SIMS analysis of triply implanted poly-Si/Si(100) samples before and after annealing.

134862-N-01

region will be strongly n-type with a surface carrier concentration exceeding  $2 \times 10^{20} \text{ cm}^{-3}$ , which should permit the formation of low-resistance ohmic contacts.

B-Y. Tsaur  
J.D. Woodhouse  
C.H. Anderson, Jr.

### 3.3 IDENTITY OF RESIDUAL DONORS IN InP

The growth of InP single-crystal boules by the liquid-encapsulated Czochralski (LEC) method has been described earlier.<sup>22</sup> As starting material, we use polycrystalline InP synthesized from the elements in the form of n-type ingots produced by directional solidification of In-rich solutions under controlled P pressure. If the LEC boules are not intentionally doped, they too are n-type. Thus, the principal electrically active species in both cases are shallow donors. For the better ingots, the total shallow donor concentration  $N_D$  is 1 to  $2 \times 10^{15} \text{ cm}^{-3}$ , as determined from the values of the electron concentration  $n_{77}$  and mobility  $\mu_{77}$  measured at 77 K. The values of  $N_D$  are always greater for nominally undoped LEC boules than for the ingot material, although these values are significantly lower for "nonstandard" boules grown from charges prepared by adding elemental In to polycrystalline ingot material than for "standard" boules grown from ingot material alone.<sup>23</sup> We have recently grown a nonstandard boule with values of  $N_D$  as low as  $1.1 \times 10^{15} \text{ cm}^{-3}$  and values of  $\mu_{77}$  up to  $7.0 \times 10^4 \text{ cm}^2\text{V}^{-1}\text{s}^{-1}$ , the highest so far reported for an LEC crystal of InP.

In attempting to achieve further reductions in  $N_D$ , it would be extremely helpful to know the identity of the principal shallow donor species in the better polycrystalline ingots and LEC boules. Even if the donors are impurities rather than native defects, they are present at concentrations too low to permit their identification by conventional analytical techniques. We have therefore investigated their identities by means of photoluminescence measurements at high magnetic fields, which were made at the Royal Signals and Radar Establishment (RSRE), United Kingdom. The results of these measurements show that the dominant shallow donor species in the polycrystalline ingots is S, while the dominant species in nominally undoped LEC boules is an unidentified donor.

For even the purest available InP, which has been prepared by vapor-phase epitaxy (VPE), peaks associated with different shallow donors are not resolved in zero-field photoluminescence spectra, since the line widths in this material exceed the expected differences of about 0.1 to 0.2 meV in the ionization energies of these donors. In high magnetic fields ( $\sim 10$  T), however, broadening is significantly reduced because the extended wave functions of the weakly bound donor electrons are strongly compressed. Application of such fields has made it possible for workers at RSRE to resolve "two-electron" satellites of peaks due to excitons bound to four different neutral donors, even for InP samples with values of  $n_{300}$  as high as  $5 \times 10^{15} \text{ cm}^{-3}$  and  $\mu_{77}$  as low as  $2.5 \times 10^4 \text{ cm}^2\text{V}^{-1}\text{s}^{-1}$ . In addition, by measurements on VPE crystals intentionally doped with very low levels of S and Si, the RSRE workers have identified the particular two-electron satellites due to these two elements.<sup>24</sup>

We have supplied three samples from polycrystalline ingots to RSRE for photoluminescence characterization. Their values of  $\mu_{77}$  range from  $6.0 \times 10^4$  to  $8.2 \times 10^4 \text{ cm}^2\text{V}^{-1}\text{s}^{-1}$ . The results for one sample indicate that S is the primary donor species, with Si also present at a concentration about one-fifth that of S. For the other two samples, S is the only significant donor species.<sup>25</sup> In view of the fact that the ingots are synthesized in silica boats sealed inside silica ampoules, it is somewhat surprising that S rather than Si is the primary donor.

Samples from one standard and three nonstandard LEC boules were also supplied to RSRE. The results<sup>25</sup> for these samples are given in Table 3-1 which lists the composition of the melt from which the sample was grown, the measured values of  $n_{77}$  and  $\mu_{77}$ , the values of  $N_D$  and total acceptor concentration  $N_A$  obtained from  $(N_D - N_A) = n_{77}$  and the value of  $(N_D + N_A)$  estimated from  $\mu_{77}$ , and the concentrations of the donor species identified by the photoluminescence measurements. The latter concentrations were found by assuming that the relative amounts of the various donor species are proportional to the intensities of their photoluminescence peaks, and that the total concentration of the donor species is equal to  $N_D$ .

TABLE 3-1

**Measured Values of  $n_{77}$  and  $\mu_{77}$  ( $10^4 \text{ cm}^2\text{V}^{-1}\text{s}^{-1}$ ) and Estimated  $N_D$ ,  $N_A$ , and Donor Concentrations in LEC Boules of InP (All Concentrations Given in Units of  $10^{15} \text{ cm}^{-3}$ )**

Boule	Melt Composition (a/o In)	$n_{77}$	$\mu_{77}$	$N_D$	$N_A$	Concentration of Donor Species		
						S	Si	Effective Mass Donor
452	56	2.7	5.7	2.9	0.2	1.2	0	1.7
470†	61	2.3	5.2	2.9	0.6	0.85	0.25	1.8
471†	50	5.0	3.0	6.5	1.5	2.5	0	4.0
474	68	2.0	5.3	2.6	0.6	1.0	0.2	1.4

† Charges prepared from aliquots of same polycrystalline ingot.

Table 3-1 shows that the principal donor in each of the four LEC samples is a species that has been designated by the RSRE workers as the "effective mass donor" because its ionization energy is very close to that calculated from simple effective mass theory. This species has not been identified chemically; it might actually be a native defect or a defect-impurity complex rather than an impurity. All four samples also contain smaller concentrations of S, while two contain relatively small amounts of Si. The concentrations of both the

effective mass donor and S are significantly lower in the samples from the three non-standard boules than in the standard one. The data for Si are too limited to establish a relationship between its concentration and the composition of the melt.

There is a marked difference between the photoluminescence results for the LEC samples and those for the samples from polycrystalline ingots, since in the latter S is the dominant donor and the effective mass donor is not detected at all. Although there are several obvious differences between our LEC and synthesis processes, none of these appear to account for the presence of the effective mass donor in the LEC boules. Additional work will be necessary to determine both the origin and the identity of this species.

G.W. Iseler

### 3.4 DEPTH PROFILES OF TRAPS IN GaAs EPILAYER ON DRY-ETCHED GaAs SUBSTRATE

In a recent report,<sup>26</sup> we described the initial results of an investigation on the effect of dry etching on the electrical properties of GaAs. In this investigation, which is an extension of an earlier study,<sup>27</sup> deep-level transient spectroscopy (DLTS) and optical DLTS (ODLTS) are being used to determine the depth profiles of electron and hole traps, respectively. The specimen was prepared by using vapor-phase epitaxy to grow a 0.6- $\mu\text{m}$ -thick n-type GaAs epilayer (doped to  $1 \times 10^{16} \text{ cm}^{-3}$ ) on an n-type GaAs substrate layer (doped to  $5 \times 10^{16} \text{ cm}^{-3}$ ) that had been reactive-ion etched, Ar-ion beam etched, and then cleaned by chemical etching. In the DLTS experiments, measurements are made of the capacitance transient obtained when a trap-filling pulse  $V_p$  is applied to a Schottky diode fabricated on the epilayer surface. Values of the trap concentration are found from the expression  $N_t = -2\Delta C/C(N_D - N_A)$ , where  $\Delta C$  is the change in capacitance immediately after the removal of the filling pulse, C is the static capacitance, and  $(N_D - N_A)$  is the net donor concentration. In the initial experiments,<sup>26</sup>  $\Delta C$  was measured as a function of temperature for four different values of DC bias  $V_b$ , so that each measurement sampled the region between the depletion widths W and  $(W + \Delta W)$  corresponding to  $V_b$  and  $(V_b + V_p)$ , respectively. The value of  $V_p$  was 0.14 V, yielding  $\Delta W$  of 0.05  $\mu\text{m}$  or less.

As observed earlier,<sup>26</sup> at any fixed value of  $V_b$  the values of C measured for the Schottky diode exhibit a significant temperature dependence, so that W also depends on temperature. The variation in C is illustrated by curve (a) in Figure 3-9, which is a plot of C measured at  $V_b = -0.30$  V as a function of temperature. This variation causes a change in W from 0.55 to 0.36  $\mu\text{m}$  between liquid nitrogen temperature (LN) and room temperature (RT). Changes of this magnitude in W can lead to significant errors in the trap density profiles measured by DLTS, since the region sampled does not remain the same during a particular temperature scan. In order to minimize such errors, we have modified the measurement setup by adding a servo-feedback circuit that varies  $V_b$  during each scan to maintain a preselected value of C, and therefore W. (The circuit's response time is too long for the individual capacitance transient measurements to be affected.) The effectiveness of this technique is illustrated by curve (b) in Figure 3-9, which shows C vs T for a run in which the feedback circuit was used.

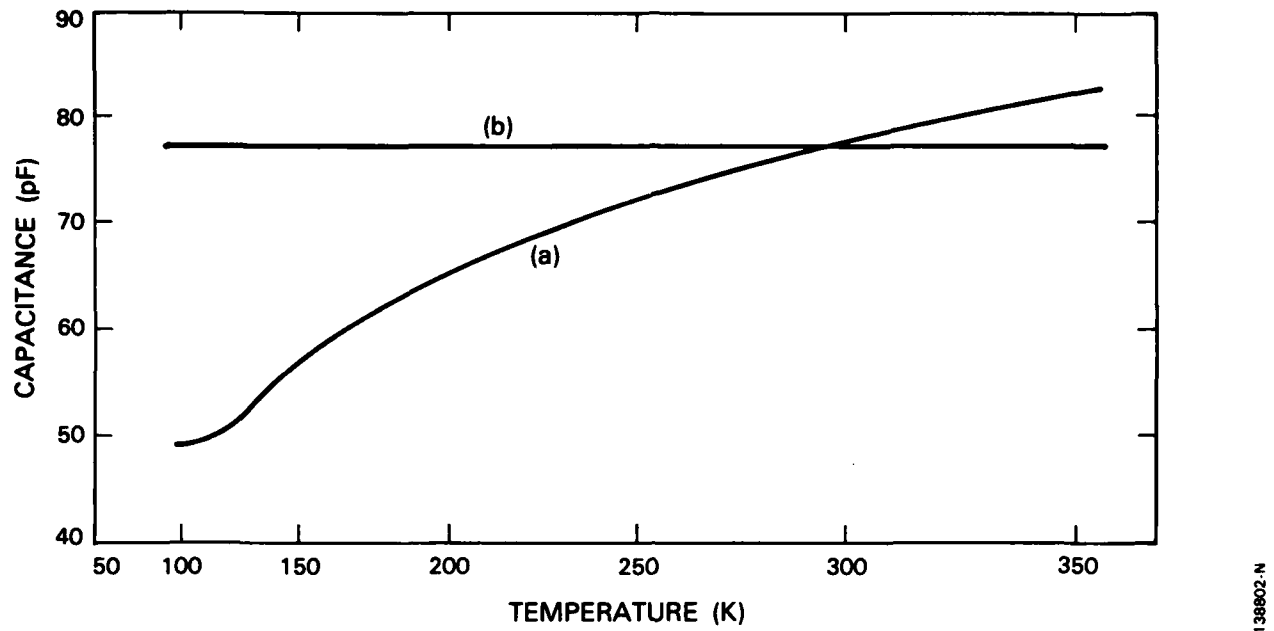


Figure 3-9. Temperature dependence of Schottky-diode capacitance measured (a) for  $V_b = 0.30$  V, and (b) for values of  $V_b$  obtained with servo-feedback circuit.

138602-N

To accurately evaluate the expression for  $N_t$ , it is necessary to use the appropriate value of  $(N_D - N_A)$ . By means of conventional C-V measurements made on the specimen at RT and LN, it was found earlier<sup>27</sup> that  $(N_D - N_A)$  varies substantially with both depth and temperature, as shown by the dashed lines plotted in Figure 3-10. We have obtained additional data by using a technique for measuring  $(N_D - N_A)$  at constant  $W$  as a function of temperature. In these measurements, the Schottky diode is modulated with a probing voltage of 8.6 mV at 10 Hz, the change in  $C$  is measured with a capacitance meter operating at 1 MHz with a modulation voltage of 100 mV, and analog circuitry is used to determine  $(N_D - N_A)$  from the expression

$$N_D - N_A = -\frac{1}{q\epsilon_0 A^2} \frac{C^3}{\frac{dC}{dV}}$$

where  $A$  is the capacitor area and  $q$ ,  $\epsilon$  and  $\epsilon_0$  have their usual meanings. Measurements of  $(N_D - N_A)$  as a function of temperature were made by this technique for values of  $W$  between 0.30 and 0.60  $\mu\text{m}$  in 0.05- $\mu\text{m}$  steps. The results are plotted in Figure 3-11. From these results we obtain depth profiles of  $(N_D - N_A)$  at LN and RT, shown as solid lines in Figure 3-10, that agree quite well with the profiles obtained by conventional C-V measurements.

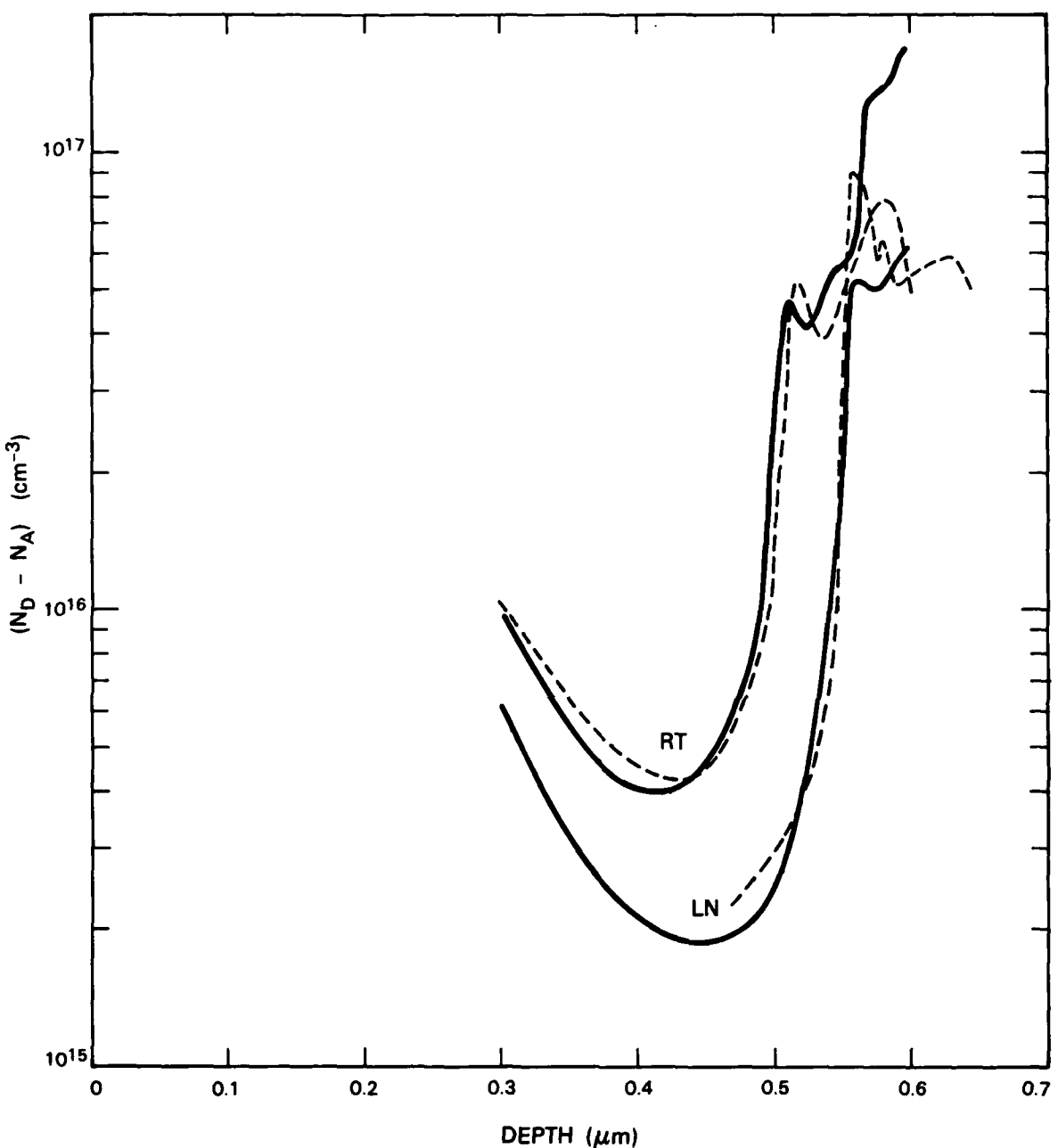


Figure 3-10. Depth profiles of  $(N_D - N_A)$  at room temperature (RT) and liquid nitrogen temperature (LN) obtained by conventional C-V method (dashed lines, after Reference 27) and by present method (solid lines).

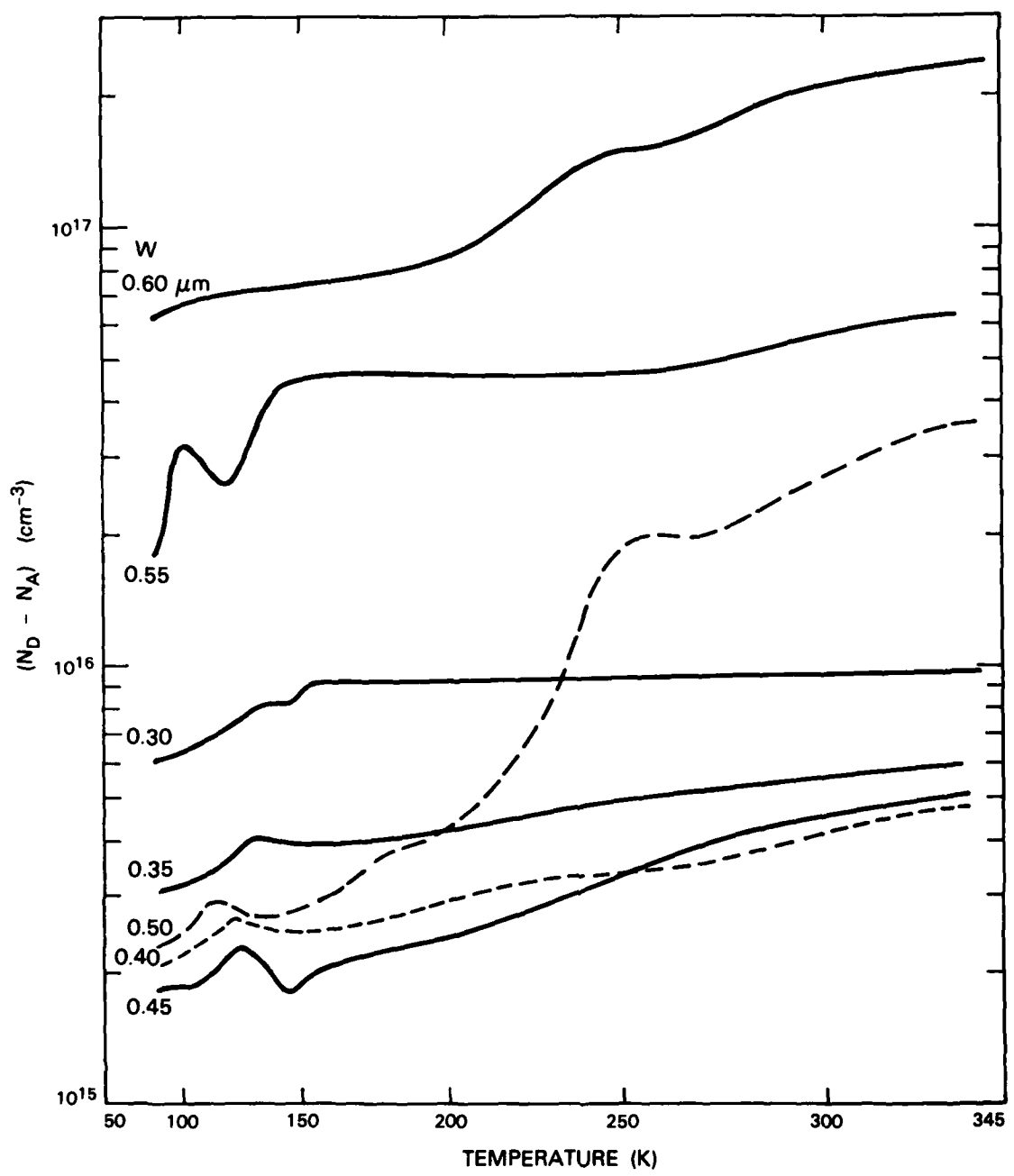


Figure 3-11. Temperature dependence of  $(N_D - N_A)$  for values of depletion width  $W$  between 0.30 and 0.60  $\mu\text{m}$ .

138804-N

The modified measuring system has been used for making two sets of DLTS measurements on the GaAs specimen, in each case for values of C selected to yield values of W between 0.30 and 0.60  $\mu\text{m}$  in 0.05- $\mu\text{m}$  steps. For the first set, the filling pulses were made large enough to fill all the traps in the depletion region, giving the results for  $\Delta C$  vs T plotted in Figure 3-12(a-b). Values of  $N_t(T)$  for each 0.05- $\mu\text{m}$  increment in W could be obtained by taking the difference between two successive plots and multiplying by the appropriate average values of  $(N_D - N_A)(1/C)$ . The second set of measurements employed a fixed  $V_p$  of only 0.15 V. These measurements, like those made earlier,<sup>26</sup> directly yield values of  $\Delta C$  for the region between W and  $(W + \Delta W)$ . Their accuracy is substantially improved over the the earlier ones because W is kept constant for each temperature scan, but they are still subject to errors arising because the value of  $\Delta W$  at constant  $V_p$  varies with W, and also with temperature for a given W. The results of the new measurements are plotted in Figure 3-13.

The structure in the  $\Delta C$  vs T plots of Figures 3-12 and 3-13 shows that the number of electron-trap species increases with increasing distance from the metal-semiconductor contact at the surface of the epilayer. The plot in Figure 3-13 for  $W = 0.55 \mu\text{m}$ , which is close to the interface between the epilayer and the etched surface of the substrate, reveals five distinct traps with energies of 0.14, 0.17, 0.35, 0.51, and 0.78 eV, as labeled on the figure. The latter four species are those conventionally designated as EL-10, EL-16, EL-4, and EL-12, respectively. A peak corresponding to the trap EL-3 (0.58 eV) appears prominently for  $W = 0.60 \mu\text{m}$ . In addition, a peak at  $\sim 400$  K corresponding to the trap EL-2 (0.83 eV) was found throughout the epilayer in runs extending to temperatures higher than those shown in Figures 3-12 and 3-13.

The constant depletion width system was also used for ODLTS measurements, in which hole traps are filled by employing a light pulse rather than a voltage pulse. Figure 3-14 shows the  $\Delta C$  vs T plots obtained for one value of the time interval used for sampling the capacitance transient. As in the earlier measurements,<sup>26</sup> there is a single peak corresponding to a trap energy of about 0.20 eV. In some subsequent measurements using other sampling times, the peak split into three components, indicating the presence of three hole traps with very similar energies.

Depth profiles for the electron trap at 0.14 eV and the traps EL-16 and E-12 have been derived from the  $\Delta C$  vs T plots of Figure 3-13. These profiles are shown in Figure 3-15, together with the hole-trap profile obtained from the plots of Figure 3-14. With increasing distance from the substrate, the concentrations of the three electron traps generally decrease, while there is an increase in the concentration of the hole trap(s). These observations suggest that the electron traps may result from the dry etching of the substrate, while the hole trap(s) may originate at the metal-semiconductor contact.

J.G. Mavroides      D.F. Kolesar  
S.W. Pang            G.A. Lincoln

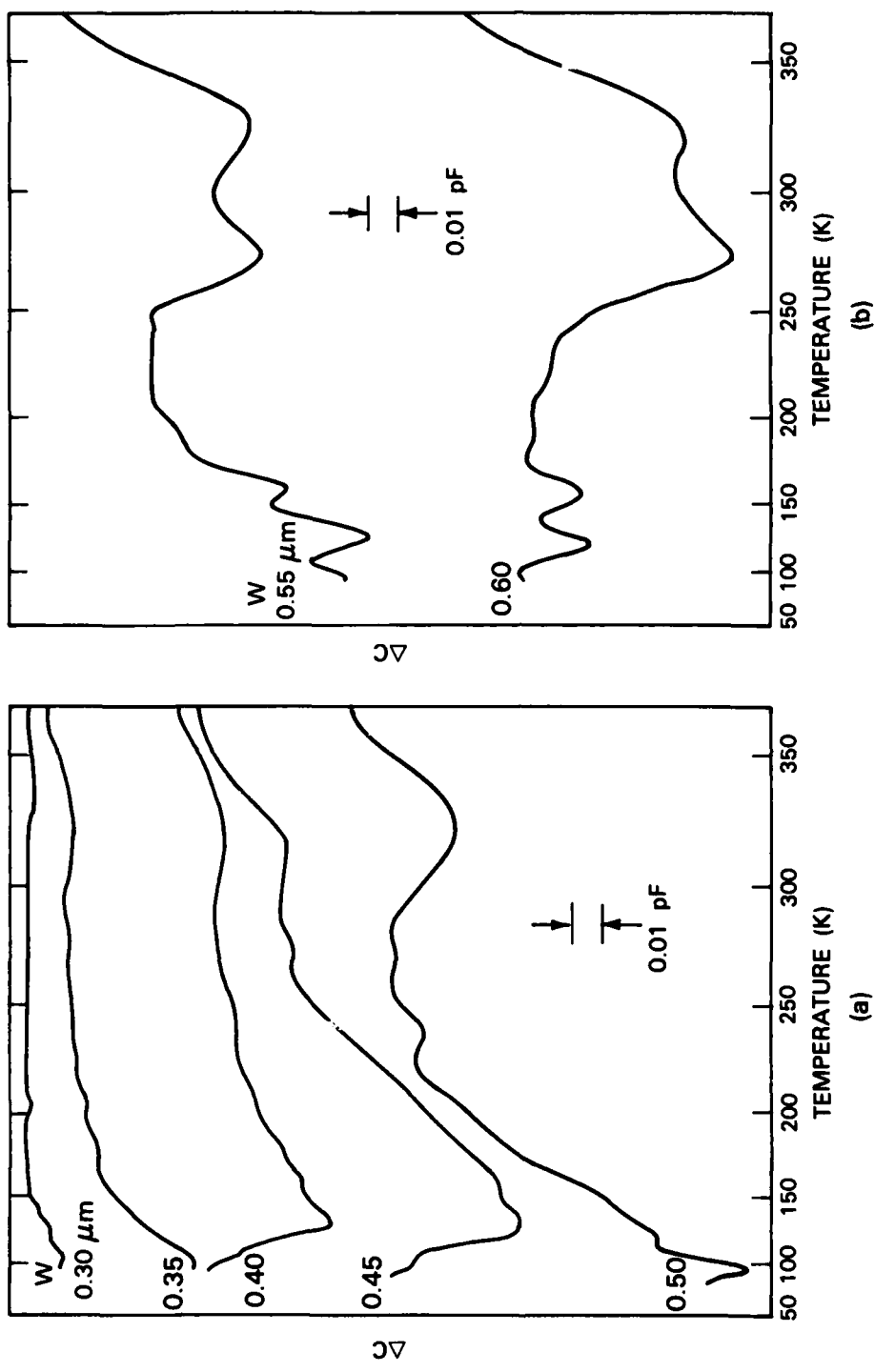


Figure 3-12. Temperature dependence of  $\Delta C$  obtained by DLTS measurements using pulses large enough to fill all traps in depletion region, for (a)  $W$  values between 0.30 and 0.50  $\mu\text{m}$ , and (b)  $W = 0.55$  and 0.60  $\mu\text{m}$ .

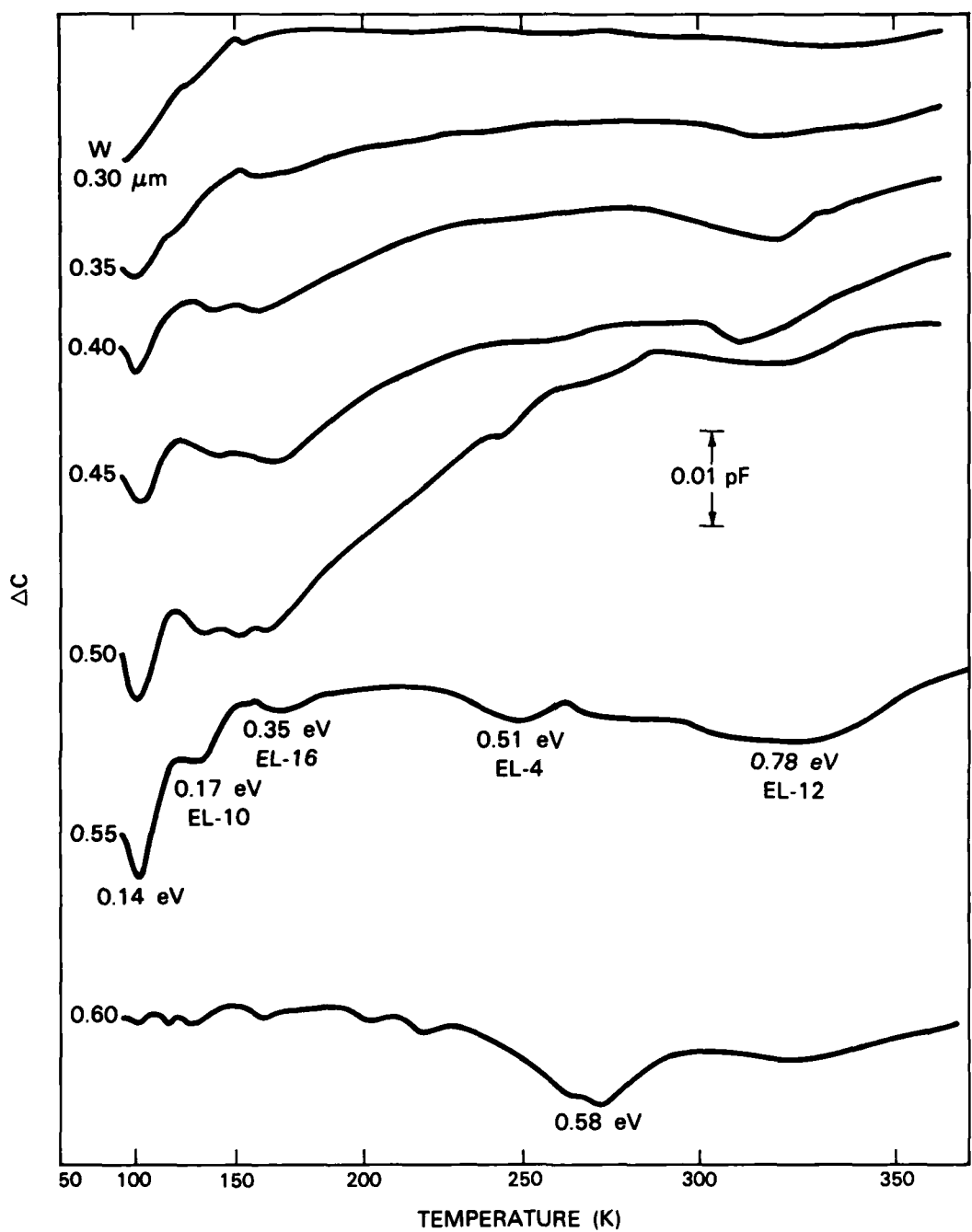


Figure 3-13. Temperature dependence of  $\Delta C$  obtained by DLTS measurements using trap-filling pulse with  $V_p = 0.15$  V, for W between 0.30 and 0.60  $\mu\text{m}$ .

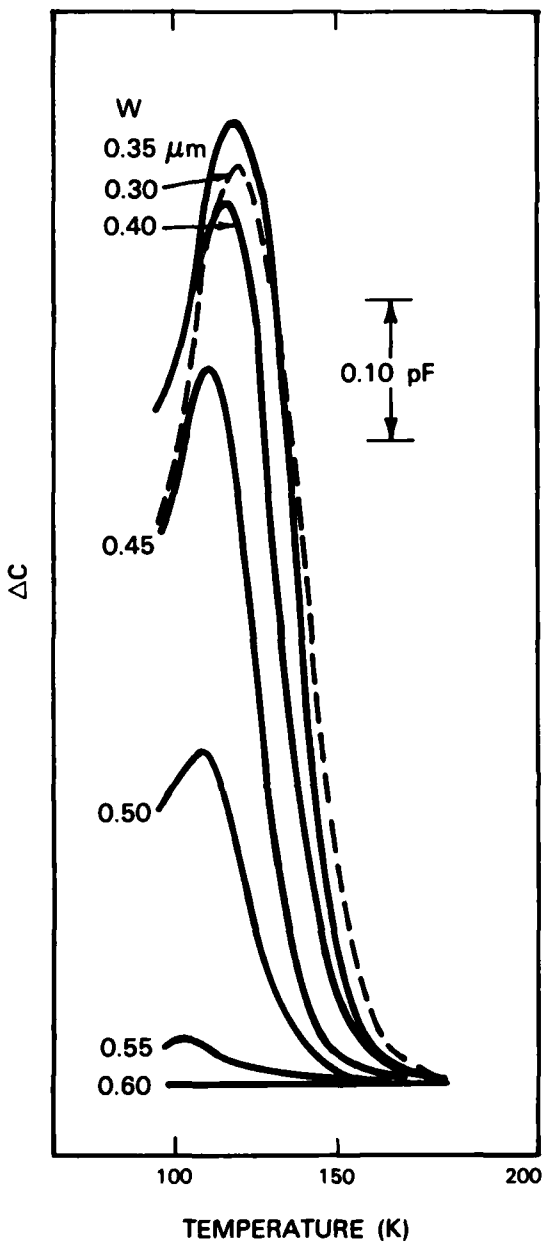


Figure 3-14. Temperature dependence of  $\Delta C$  obtained by ODLTS measurements for  $W$  between 0.30 and 0.60  $\mu\text{m}$ .

138807-N

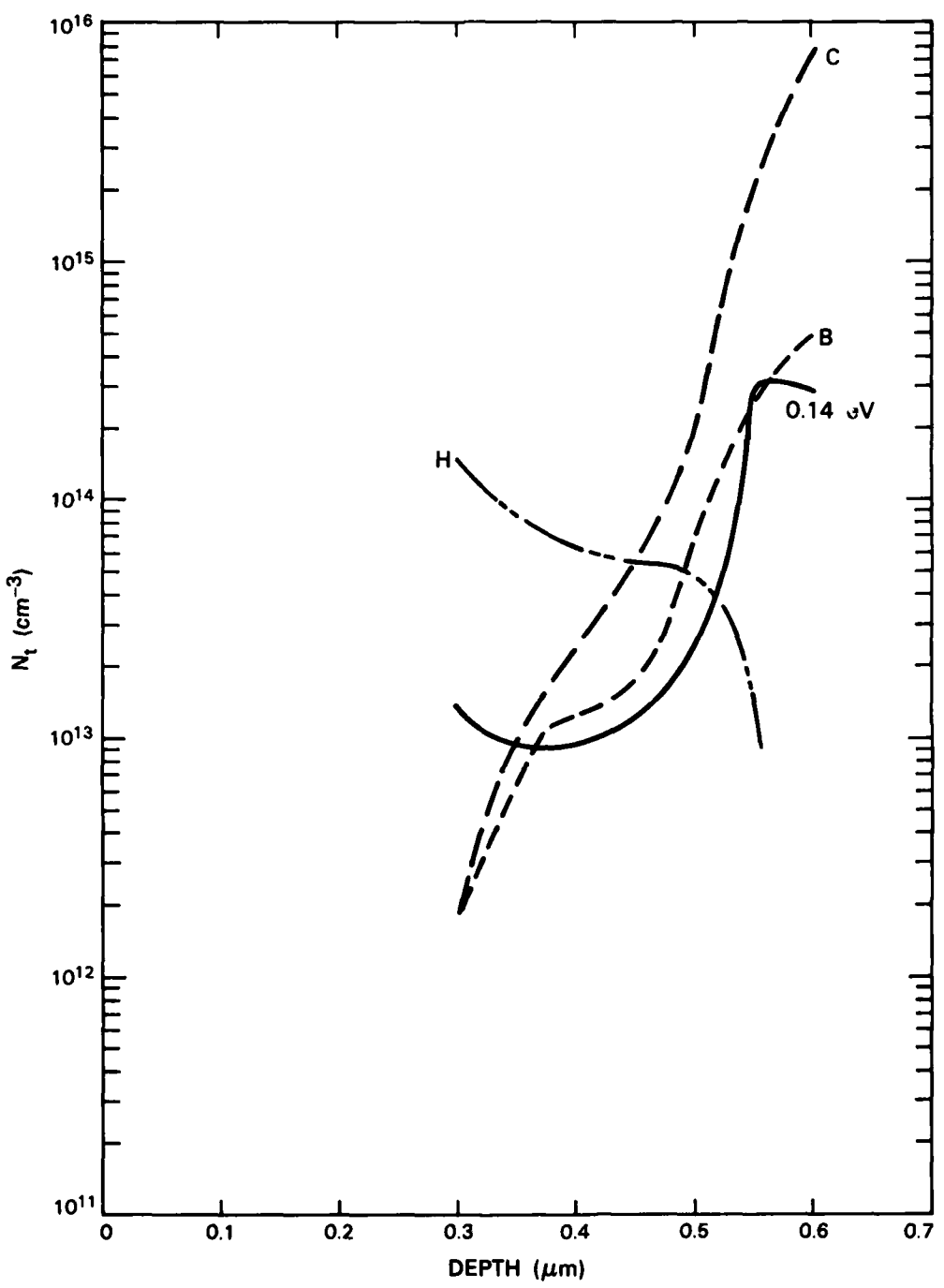


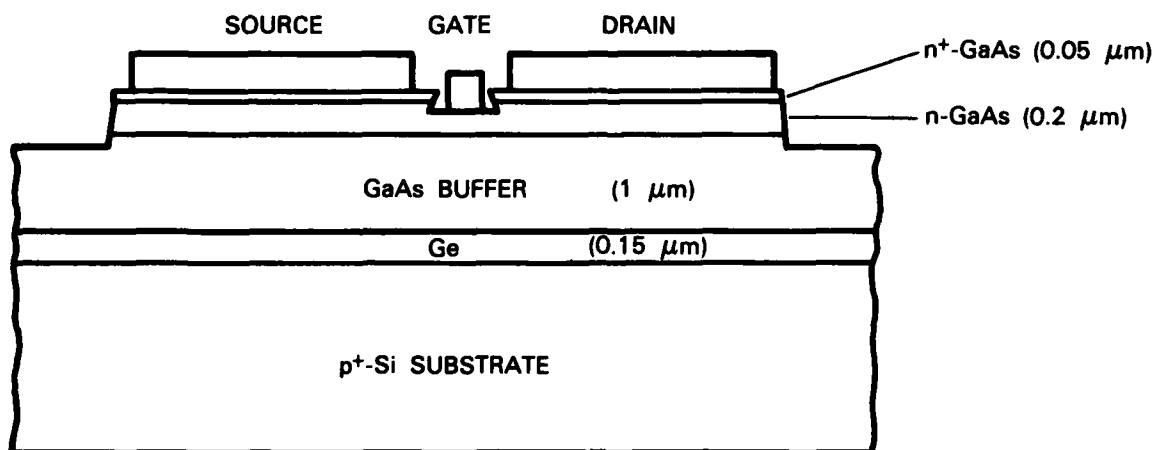
Figure 3-15. Depth profiles of hole trap and three electron traps.

### 3.5 GaAs MESFETS FABRICATED ON MONOLITHIC GaAs/Si SUBSTRATES

Recently, there has been growing interest in the possibility of developing integrated circuits that combine GaAs and Si devices fabricated on a single monolithic GaAs/Si (MGS) chip. Such MGS ICs could take advantage of the unique device capabilities of GaAs and Si more fully than hybrid circuits composed of devices on separate GaAs and Si chips. For example, MGS ICs could utilize GaAs diode lasers to form optical links for high-data-rate intrachip and interchip communication. Currently, MGS substrates are prepared by growing GaAs layers on Si wafers. Device-quality GaAs layers have not been obtained by direct growth on Si, however, because nucleation is difficult and also because GaAs and Si differ greatly in their lattice constants and thermal-expansion coefficients. At the present stage of MGS technology development, attention is focused on perfecting the growth of GaAs layers and demonstrating that devices with good operating characteristics can be fabricated in these layers.

The only MGS GaAs devices so far reported are shallow-junction solar cells<sup>28,29</sup> and light-emitting diodes.<sup>30</sup> The solar cells were fabricated in GaAs layers grown by AsCl<sub>3</sub>-GaAs-H<sub>2</sub> chemical-vapor deposition on Si wafers that had been coated with a thin nucleating epi-layer of Ge, which has lattice properties close to those of GaAs (see Reference 31). The light-emitting diodes were fabricated in GaAs layers grown by organometallic chemical-vapor deposition on Ge layers prepared by zone-melting recrystallization on SiO<sub>2</sub>-coated Si wafers. We report here the fabrication of the first MGS GaAs MESFETs. These devices, which were fabricated in GaAs layers grown by MBE on Ge-coated Si substrates, have good transistor characteristics, with maximum transconductance of 105 mS/mm for a gate length of 2.1 μm.

The design of the MGS GaAs MESFETs is shown schematically in Figure 3-16. An undoped Ge layer is deposited by e-beam evaporation<sup>32</sup> on a p<sup>+</sup>-Si substrate oriented 2°



135854-N-01

Figure 3-16. Design of MGS GaAs MESFET fabricated on monolithic GaAs/Si substrate. Doping concentrations of n and n<sup>+</sup> GaAs layers are  $1 \times 10^{17}$  and  $2.5 \times 10^{18} \text{ cm}^{-3}$ , respectively.

off (100) toward (011). Three GaAs layers — an undoped buffer layer, an n active-channel layer, and an n<sup>+</sup> contacting layer — are then grown by MBE. As shown by the Nomarski interference micrograph of Figure 3-17, the GaAs layers have mirror-smooth surfaces without any antiphase domains. No cracks have been observed after growth or during device fabrication. Mesa isolation is performed by wet chemical etching. The source and drain contacts are formed by alloying evaporated Ge/Au/Ni patterned by the photoresist lift-off process. The gate region is recessed by wet chemical etching, and the gate contact is made with evaporated Ti/Au patterned by the lift-off process. Figure 3-18 is an optical micrograph of a finished device.

Figure 3-19 shows the Schottky-diode characteristic between the source and gate (2.1 μm long, 200 μm wide) of an MGS GaAs MESFET. From the data for the forward direction, the built-in voltage is about 0.67 V and the ideality factor is about 1.38. The reverse leakage current, which increases from about 3 μA at V<sub>gs</sub> = -1 V to about 12 μA at V<sub>gs</sub> = -2 V, is believed to be due to a high density of defects that propagate from the Ge/Si interface. Preliminary results of a separate study indicate that the diode leakage current can be considerably reduced by growing a thicker buffer layer in order to reduce the defect density.

Figure 3-20 shows transistor characteristics for another MGS GaAs MESFET with gate length of 2.1 μm and gate width of 200 μm. The top curve was obtained for V<sub>gs</sub> = 0.5 V. The transconductance measured at V<sub>gs</sub> = 0 V is about 105 mS/mm, which is comparable to the values obtained for MESFETs on GaAs substrates.<sup>33</sup> This result suggests that the defect density in the GaAs active channel is not high enough to produce a marked reduction in the majority carrier mobility. However, the drain current is not completely turned off. A more detailed measurement at V<sub>gs</sub> = 2 V shows that the drain current reaches a minimum and then increases as V<sub>gs</sub> is made increasingly negative. This result indicates that the transistor leakage current is largely due to leakage between the gate and the drain, although there may also be a contribution from leakage through the buffer layer.

H.K. Choi              G.W. Turner  
B-Y. Tsaur              J.C.C. Fan  
G.M. Metze

135896-R-01

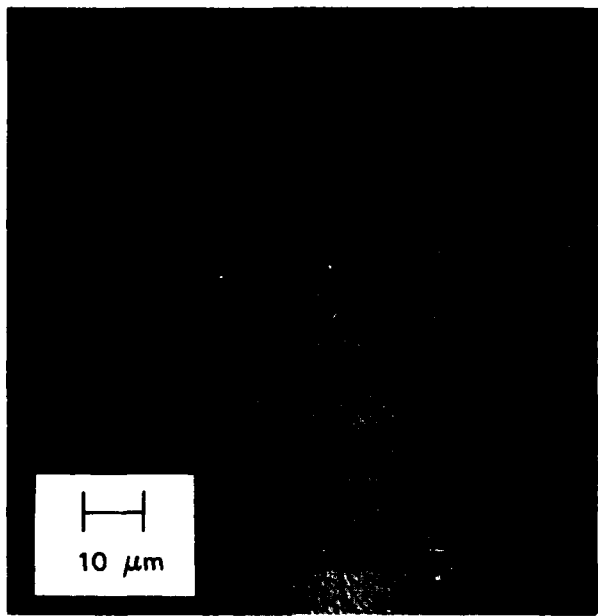


Figure 3-17. Nomarski interference micrograph showing surface morphology of GaAs layer grown by MBE on Ge-coated Si substrate.

135895-R-01

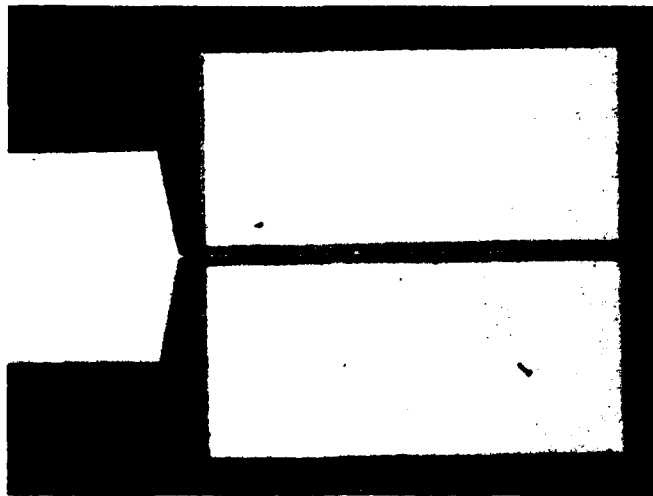


Figure 3-18. Optical micrograph of MGS GaAs MESFET with gate length of 2.1  $\mu\text{m}$  and gate width of 200  $\mu\text{m}$ .

135894-R

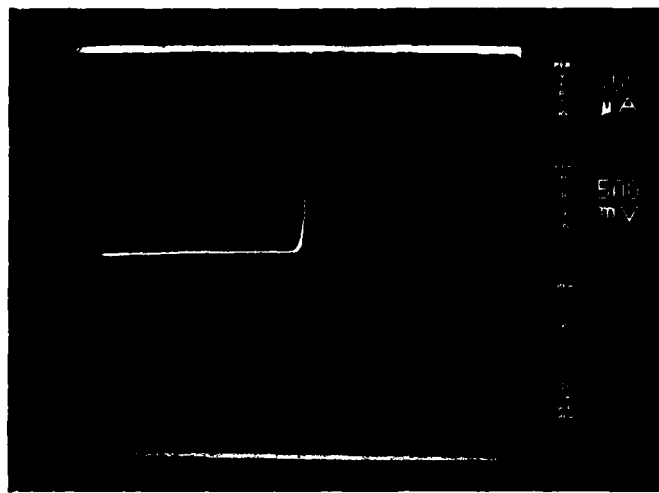


Figure 3-19. Schottky-diode characteristic between source and gate of MGS GaAs MESFET.

135895-R

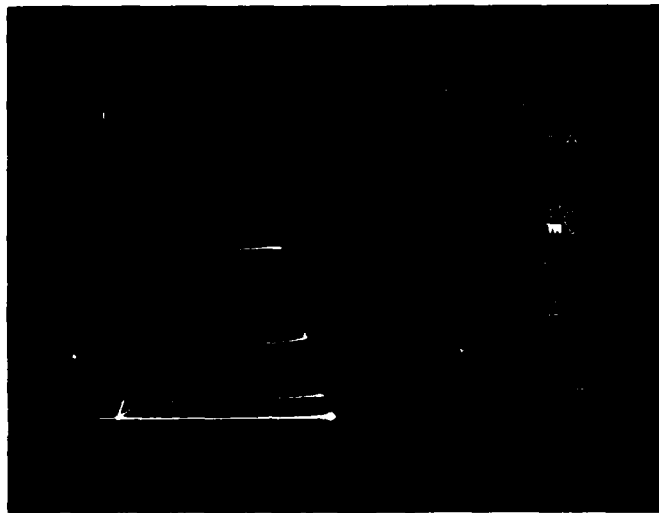


Figure 3-20. Transistor characteristics of MGS GaAs MESFET. Top curve is for  $V_{gs} = 0.5$  V.

## REFERENCES

1. J.C.C. Fan, B-Y. Tsaur, and M.W. Geis, in *Technical Digest, 1980 International Electron Devices Meeting, Washington, DC, 1980* (IEEE, New York, 1980), p. 845.
2. J.C.C. Fan, M.W. Geis, and B-Y. Tsaur, *Appl. Phys. Lett.* **38**, 365 (1981), DTIC AD-A130036/0.
3. B-Y. Tsaur, J.C.C. Fan, M.W. Geis, D.J. Silversmith, and R.W. Mountain, *Appl. Phys. Lett.* **39**, 561 (1981), DTIC AD-A110725/9.
4. M.W. Geis, H.I. Smith, B-Y. Tsaur, J.C.C. Fan, E.W. Maby, and D.A. Antoniadis, *Appl. Phys. Lett.* **40**, 158 (1982), DTIC AD-A121757.
5. J.C.C. Fan, B-Y. Tsaur, and M.W. Geis, *J. Cryst. Growth* **63**, 453 (1983).
6. R.F. Pinizzotto, H.W. Lam, and B.L. Vaandrager, *Appl. Phys. Lett.* **40**, 388 (1982).
7. For example, A. Kamgar and E. Labate, *Mater. Lett.* **1**, 91 (1983).
8. For example, A. Gat, L. Gerzberg, J.F. Gibbons, T.J. Magee, J. Peng, and J.D. Hong, *Appl. Phys. Lett.* **33**, 775 (1978).
9. For example, J.A. Knapp and S.T. Picraux, in *Laser-Solid Interactions and Transient Thermal Processing of Materials*, J. Narayan, W.L. Brown, and R.A. Lemons, Eds. (North Holland, New York, 1983), p. 557.
10. T. Carlberg, T.B. King, and A.F. Witt, *J. Electrochem. Soc.* **129**, 189 (1982).
11. W. Lin and D.W. Hill, *J. Appl. Phys.* **54**, 1082 (1983).
12. The equation for  $k_{\text{eff}}$  is given in Reference 11. The thickness of the diffusion boundary layer for our ZMR-samples is estimated to be much larger than  $50 \mu\text{m}$ , thus making  $k_{\text{eff}}$  close to one. We acknowledge private communications with W. Lin.
13. See, for example, J.C. Brice in *The Growth of Crystals from Liquids* (North-Holland Elsevier, New York, 1970), Chapter 3; or W.R. Wilcox, *J. Cryst. Growth* **7**, 203 (1970).
14. W. Bardsley, J.S. Boulton, and D.T.J. Hurle, *Solid-State Electron.* **5**, 395 (1962).
15. S. Gaur, *IEEE J. Solid-State Circuits* **SC-14**, 337 (1979).
16. B-Y. Tsaur and C.H. Anderson, Jr., *J. Appl. Phys.* **54**, 6336 (1983).
17. T.M. Liu and W.G. Oldham, *Electrochemical Society Meeting, San Francisco, May 1983, Extended Abstracts*, Vol. 83-1, p. 631.

18. W. Maszara, C. Carter, D.K. Sadana, J. Liu, V. Ozguz, J. Wortman, and G.A. Rozgonyi, paper presented at Symposium of Energy Beam-Solid Interactions and Transient Thermal Processing, MRS Meeting, Boston, Massachusetts, 1983.
19. See, for example, T.H. Ning and R.D. Isaac, IEEE Trans. Electron Dev. **ED-27**, 2051 (1980).
20. J.F. Gibbons, W.S. Johnson, and S.W. Mylroi, *Projected Range Statistics*, 2nd Edition (Dowden, Hutchinson and Ross, Stroudsburg, Pennsylvania, 1975).
21. See, for example, B. Swaminathan, K.C. Saraswat, R.W. Dutton, and T.I. Kamins, Appl. Phys. Lett. **40**, 795 (1982).
22. G.W. Iseler, J. Cryst. Growth **54**, 16 (1981), DTIC AD-A107051/5; Solid State Research Report, Lincoln Laboratory, M.I.T. (1980:3), p. 21, DTIC AD-A094075/9.
23. Solid State Research Report, Lincoln Laboratory, M.I.T. (1982:3), p. 35, DTIC AD-A124305/4.
24. P.J. Dean, M.S. Skolnick, and L.L. Taylor, J. Appl. Phys. (to be published).
25. P.J. Dean, M.S. Skolnick, B. Cockayne, W.R. MacEwan, and G.W. Iseler, J. Cryst. Growth (to be published).
26. Solid State Research Report, Lincoln Laboratory, M.I.T. (1983:3), pp. 49-59.
27. S.W. Pang, G.A. Lincoln, R.W. McClelland, P.D. DeGraff, M.W. Geis, and W.J. Piacentini, J. Vac. Sci. Technol. B **1**, 1334 (1983).
28. R.P. Gale, J.C.C. Fan, B-Y. Tsaur, G.W. Turner, and F.M. Davis, IEEE Electron Device Lett. **EDL-2**, 169 (1981), DTIC AD-A107056/4.
29. B-Y. Tsaur, J.C.C. Fan, G.W. Turner, F.M. Davis, and R.P. Gale, *Conference Record of the 16th IEEE Photovoltaic Specialists Conference, San Diego, California, 1982* (IEEE, New York, 1982), p. 1143, DTIC AD-A135130/3.
30. Y. Shinoda, T. Nishioka, and Y. Ohmachi, Jpn. J. Appl. Phys. Lett. **22**, L450 (1983).
31. J.C.C. Fan, R.P. Gale, F.M. Davis, and G.H. Foley, Appl. Phys. Lett. **37**, 1024 (1980), DTIC AD-A101031/3.
32. B-Y. Tsaur, M.W. Geis, J.C.C. Fan, and R.P. Gale, Appl. Phys. Lett. **38**, 779 (1981), DTIC AD-A103403/2.
33. H. Fukui, Bell Syst. Tech. J. **58**, 771 (1979).

## 4. MICROELECTRONICS

### 4.1 CHARGE-COUPLED DEVICES: TIME-INTEGRATING CORRELATOR

A CCD binary-analog time-integrating correlator (TIC) has been described in several previous reports<sup>1-4</sup> and a recent publication.<sup>5</sup> This 32-channel device was developed for GPS (Global Positioning System) and other spread-spectrum applications with bandwidths up to 10 MHz. Previously, we reported device operation at a 20-MHz clock rate with 25- $\mu$ s integration time, and initial results with a digital post-processing system to remove spatial or pattern noise from the CCD output and to perform additional time integration. In this report, we describe further results with this system including a process gain of 70 dB and the recovery of a pseudonoise (PN) signal in Gaussian noise with a -50-dB signal-to-noise ratio (SNR). With this system, the pattern noise is reduced to a level below the temporal noise of the CCD, and under these conditions the dynamic range of the CCD is 67 dB.

Figure 4-1 describes the principal features of the combined CCD/digital-processor system. The CCD correlator, shown at the left, is a 32-channel device using a pipe-organ architecture consisting of delay lines of 1 to 32 stages in length. The input delay lines are clocked at a 20-MHz rate, and for this sampling rate the input signal would normally have a bandwidth of up to 10 MHz. In the results described later, the input signal was a 10-Mbps m-sequence combined with Gaussian noise and low-pass filtered to 10 MHz; the same m-sequence, delayed by a few clock periods, was used as the local reference. The reference is modulated by the binary-level waveform described in Figure 4-1 before it is applied to the CCD. This code modulation is the basis of the pattern-noise removal method described previously.<sup>4</sup> The products of the delayed signal charge and the modulated reference are integrated for 512 clock periods or 25.6  $\mu$ s, and the integrated charge is then transferred to an output register and read out at a 1.4-MHz rate.

The digital portion of the system begins with an 8-bit A/D converter that digitizes the CCD output and sends the data to a binary multiplier. This multiplier removes the reference modulation from the correlation portion of the CCD signal, and at the same time modulates the pattern-noise portion that was unaffected by the earlier reference modulation in the CCD. The data then proceed to an accumulating memory consisting of an adder and a memory with 32 locations for integrating data from each of the 32 channels of the TIC. The 24-bit depth of the memory permits integration times of more than 1 s before overflow. The accumulator integrates for a period of  $2N \times (\text{CCD integration period})$  and then transfers the result either to a D/A converter for oscilloscope display or to a computer. Because the integrator accumulates an even number of data frames from the CCD, the pattern-noise component is canceled.

A severe test of this system and one that simulates a realistic spread-spectrum situation is illustrated in Figure 4-2 where the input signal (top trace) is a  $2^{20}$ -1-bit m-sequence combined with Gaussian noise with a low SNR of -50 dB. The middle trace shows the CCD output; but, since the process gain of this device is about 25 dB, the SNR at this

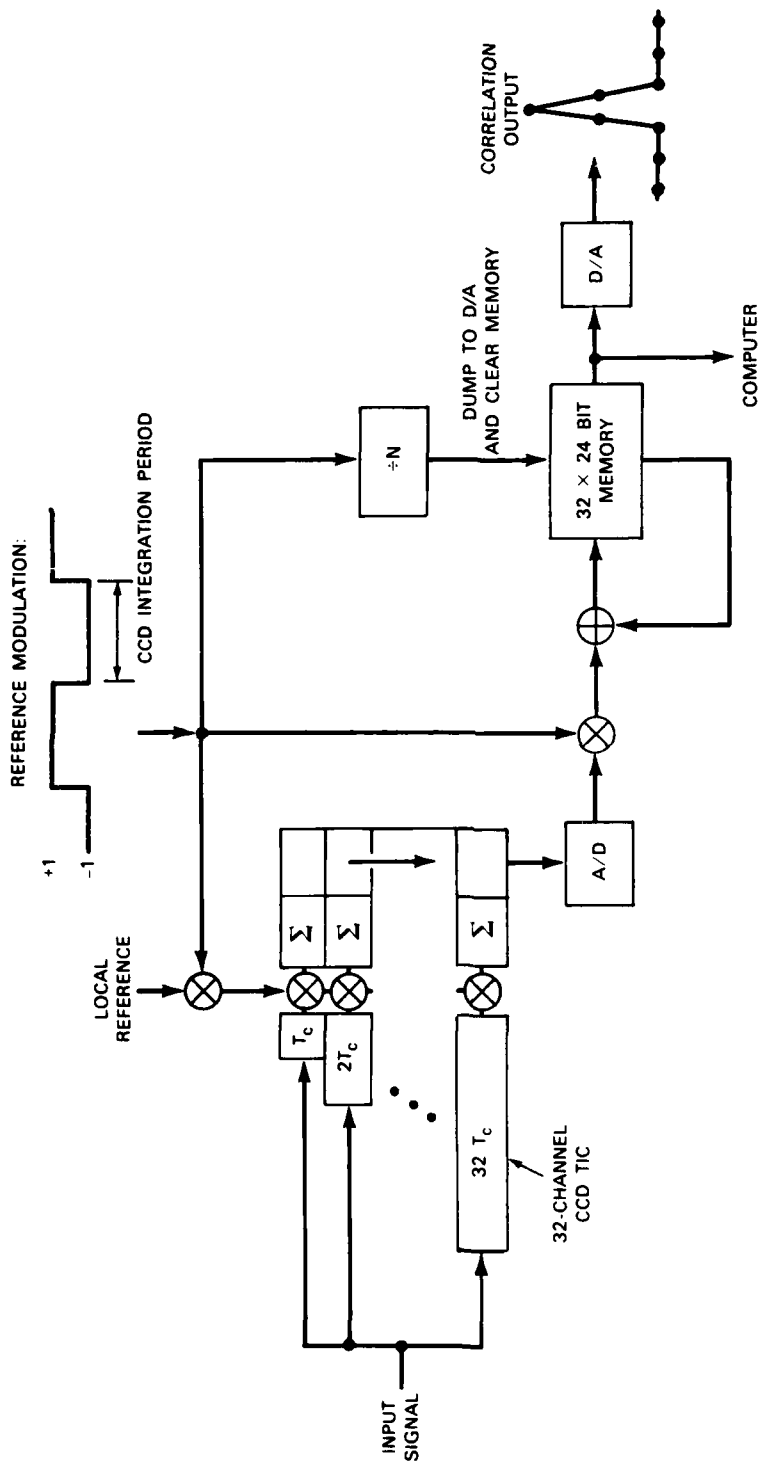


**Figure 4-1.** Schematic diagram of a correlator system using a CCD time-integrating correlator and a digital post-processor for pattern-noise suppression and additional integration.

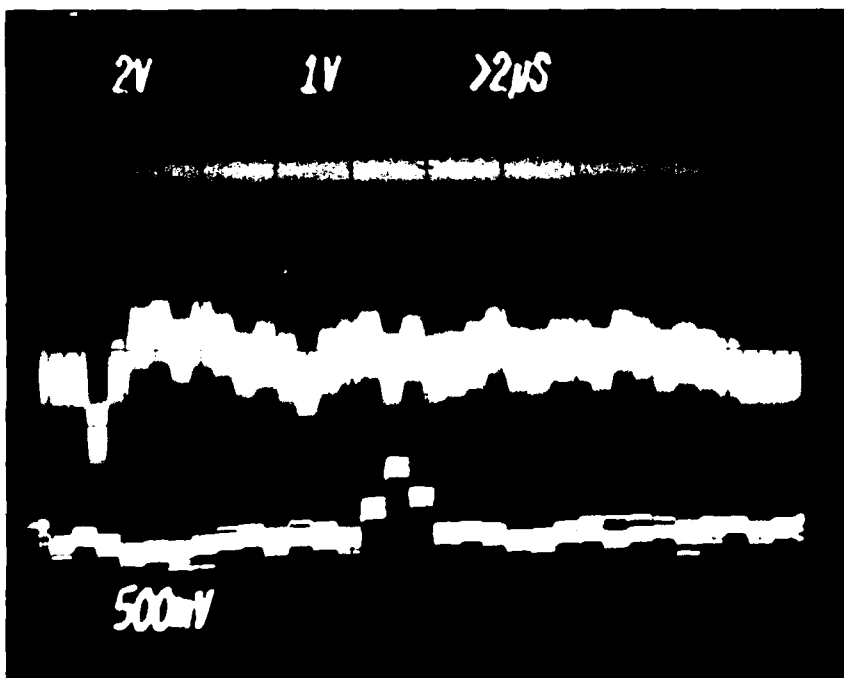


Figure 4-2. Top trace: CCD input signal consisting of an m-sequence with Gaussian noise (SNR = 50 dB). Middle trace: CCD correlator output. Bottom trace: Output of post-processor after integrating 32768 frames of CCD output data.

point is -25 dB. In addition, the signal lies about 35 dB below the spatial pattern noise, which is evident in this trace. The post-processor then integrates 32768 successive data frames for a total integration time of 0.83 s, and the result is displayed as the bottom trace. The correlation peak now lies well above both the temporal and spatial noise. The measured temporal SNR was 20 dB, indicating a total process gain of 45 dB [10 log(32768)] from the digital integrator. Some nonuniformities in the sidelobes can be seen in the lower trace, indicating incomplete suppression of the pattern noise. An rms pattern noise was computed using the mean values of the sidelobes, and from this a "spatial" SNR was found to be 22 dB. The noise-cancellation process has therefore been highly effective, which can be seen by the fact that the pattern noise has been suppressed by 57 dB relative to the signal.

An additional conclusion of these measurements is that the pattern noise can be suppressed to a level below the CCD thermal noise. The CCD dynamic range can therefore be considered to be limited by its internal temporal noise. On this basis a dynamic range of 67 dB has been measured.

B.E. Burke  
W.H. McGonagle  
D.L. Smythe

## 4.2 MODIFICATION OF SCHOTTKY-DIODE CHARACTERISTICS IN GaAs BY DRY ETCHING

Damage induced in GaAs by Ar ion-beam etching (IBE), reactive-ion etching (RIE) with  $\text{CF}_4$  and  $\text{CHF}_3$ , and ion-beam-assisted etching (IBAE) with Ar and  $\text{Cl}_2$  has been studied. The effects of etching were determined by evaluating Schottky diodes fabricated on the etched surfaces and by using deep-level transient spectroscopy (DLTS) to characterize trapping centers. Variations in the etching conditions had a strong effect on the measured characteristics of the samples.<sup>6,7</sup> GaAs samples were n-type layers grown by vapor-phase epitaxy (VPE) on n<sup>+</sup> substrates. The epitaxial layers were typically doped at  $1 \times 10^{16} \text{ cm}^{-3}$  and were 1  $\mu\text{m}$  thick. Schottky diodes were prepared on the GaAs surfaces after etching by using Ti-Au for the Schottky contacts and Ni-Ge-Au for the ohmic contacts.

Forward and reverse current-voltage (I-V) characteristics were measured on Schottky diodes fabricated on GaAs surfaces after Ar IBE. Ion energies of 250, 500, and 1000 V were used. The current density was 0.25 mA/cm<sup>2</sup> at 250 V, and 0.5 mA/cm<sup>2</sup> at 500 and 1000 V. Barrier height, n-factor, and breakdown voltage were deduced from the I-V measurements. Table 4-1 summarizes the measured values of the three parameters after Ar IBE. The diodes showed large reverse leakage currents and reduced barrier heights after IBE. This is probably due to surface disorder or Ar inclusion introduced by ion bombardment during etching. Auger analysis using xenon as the sputtering gas indicated that the amount of Ar present in the GaAs substrates and the penetration depth of the Ar increased with ion energy. Current-voltage and C-V characteristics recovered only after etching-off 750 Å of GaAs with a wet chemical solution.

TABLE 4-1  
Parameters Deduced from I-V Measurements on Schottky Diodes

Etching Condition	n	$\phi_B$ (eV)	$V_{BR}$ (V)
Control	1.04	0.76	38
Ar 250 V	1.06	0.60	16
Ar 500 V	Leaky	Leaky	<0.05
Ar 1000 V	Leaky	Leaky	<0.05

The presence of a  $\text{Cl}_2$  flux during Ar IBE has been shown to produce anisotropic etching of GaAs (see Reference 8). In addition, substantially less damage is introduced by this IBAE technique than by Ar IBE. Figure 4-3 shows the forward I-V characteristics for

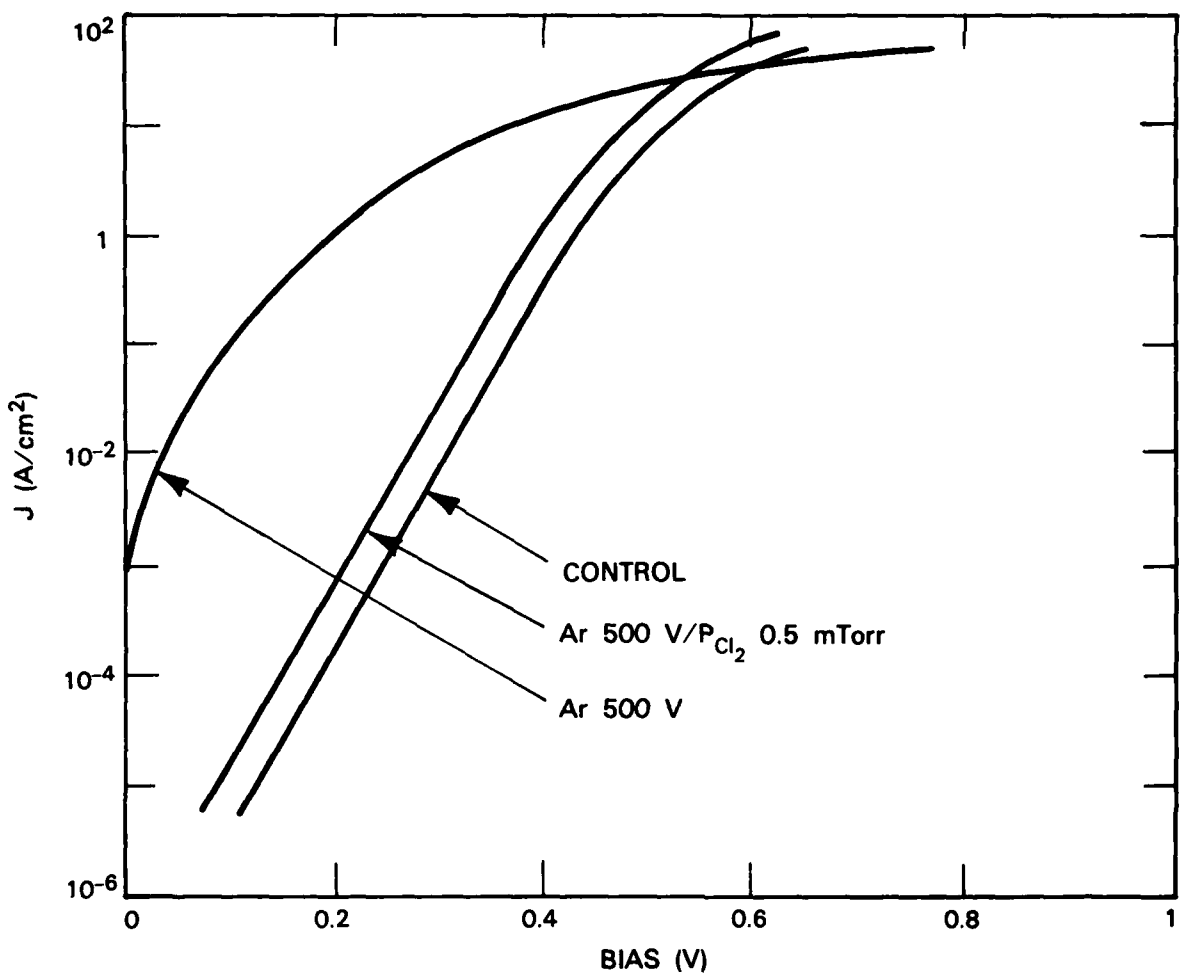


Figure 4-3. Semilog plot of forward current density as a function of voltage for a control sample, samples etched by Ar IBE at 500 V, and samples etched by IBAE with an  $\text{Ar}^+$  energy of 500 V and  $\text{Cl}_2$  flux equivalent to  $5 \times 10^{-4}$  Torr.

Schottky diodes fabricated on a control sample, a sample after etching by IBAE at 500 V with  $5 \times 10^{-4}$  Torr  $\text{Cl}_2$  pressure, and a sample etched by Ar IBE at 500 V. Without the presence of  $\text{Cl}_2$  during etching, both the forward and reverse I-V characteristics of the sample became leaky. The introduction of  $\text{Cl}_2$  at pressures as low as  $5 \times 10^{-4}$  Torr improved the diode behavior significantly. There was a slight reduction in the barrier height from 0.76 eV for a control sample to 0.72 eV after IBAE. Both ideality factor and reverse breakdown voltage were unchanged after etching by IBAE. In the range of Ar ion energy of 350 to 1000 V and equivalent  $\text{Cl}_2$  flux of 5 to  $50 \times 10^{-4}$  Torr that we have investigated, the

diodes fabricated directly on the etched surfaces showed I-V characteristics similar to those of control samples. These results show the importance of Cl<sub>2</sub> in minimizing damage induced by Ar IBE.

DLTS was used to detect and characterize trapping centers induced by dry etching. In order to probe the etched surfaces, which are usually shielded by the intrinsic depletion layer under a metal contact, 0.6-μm-thick GaAs layers were grown by VPE on the etched surfaces so that the etched region would not reside in the depleted layer. The growth of GaAs required cleaning the surfaces with hot H<sub>2</sub>SO<sub>4</sub> solution, which etched about 200 Å of the surface. The samples were also subjected to the 700°C temperature used in the VPE growth. The remaining damage in GaAs was expected to be reduced from its original value because of the cleanup and the thermal annealing. Results from the DLTS measurements are summarized in Table 4-2. The control sample had a trap density around  $1.3 \times 10^{13} \text{ cm}^{-3}$ . After RIE in CF<sub>4</sub> at 250 V, one additional trap with a concentration around  $1.6 \times 10^{13} \text{ cm}^{-3}$  was observed. When the sample was subsequently etched by Ar IBE at 500 V, a third trap near the conduction-band edge was introduced. However, when the sample was etched by IBAE following Ar IBE, the trap generated by Ar IBE was eliminated.

**TABLE 4-2**  
**DLTS Measurements**

Etching Condition	$N_t(10^{13} \text{ cm}^{-3})$		
	Trap 1	Trap 2	Trap 3
Control	1.3	—	—
CF <sub>4</sub> 250 V	2.3	1.6	—
CF <sub>4</sub> 250 V; Ar 500 V	1.7	1.7	4.0
CF <sub>4</sub> 250 V; Ar 500 V; IBAE 500 V	1.5	2.7	—
	$E_a(\text{eV})$	$\sigma(\text{cm}^2)$	
	0.89	$8 \times 10^{-13}$	
Trap 1	0.7	$3 \times 10^{-13}$	
Trap 2	0.14	$5 \times 10^{-15}$	

For GaAs samples reactive-ion etched in  $\text{CF}_4$  and  $\text{CHF}_3$ , I-V measurements on Schottky diodes fabricated on the etched surfaces indicated that barrier height and breakdown voltages were increased after etching at 500 V, as shown in Table 4-3. This change in barrier height and breakdown voltage suggests the formation of a polymer film or defect states on the sample surfaces during RIE. Capacitance-voltage measurements after RIE in  $\text{CF}_4$  at 250, 500, and 700 V are shown in Figure 4-4. The slope of  $1/C^2$  vs V is inversely proportional to the doping density, and the intercept on the voltage axis is related to the barrier height. Deviation from the control sample characteristics increased with bias voltage used during RIE.

TABLE 4-3 Parameters Deduced from I-V Measurements on Schottky Diodes		
Etching Condition	$\phi_B$ (eV)	$V_{BR}$ (V)
Control	0.73	40
$\text{CF}_4$ 500 V	0.82	50
$\text{CHF}_3$ 500 V	0.79	62

In summary, dry etching of GaAs by Ar IBE, RIE, or IBAE has been shown to induce changes in trapping levels, barrier heights, breakdown voltages, and effective substrate doping. The degree of electrical characteristic modification increases with the bias voltage used during dry etching. The presence of  $\text{Cl}_2$  during IBAE significantly reduced the damage generated by Ar IBE.

S.W. Pang  
G.A. Lincoln

M.W. Geis  
A. Vera

#### 4.3 ULTRA-LOW TEMPERATURE GROWTH OF GaAs USING CHLORIDE-TRANSPORT VAPOR-PHASE EPITAXY

We report on GaAs vapor-phase-epitaxy (VPE) epitaxial films grown at a temperature of 500°C at rates of 0.5 to 1.5  $\mu\text{m}/\text{h}$  in a chloride-transport process using a modified  $\text{AsCl}_3$ -GaAs-H<sub>2</sub> reactor. The chloride-transport VPE technique is especially useful for selective epitaxy in which it is desirable to minimize nucleation on a growth mask. Because gallium has a very low sticking coefficient to growth masks made from materials such as tungsten or silicon dioxide, lateral growth should be superior to that obtained by MBE or OMCVD in which the sticking coefficient of gallium is essentially unity.

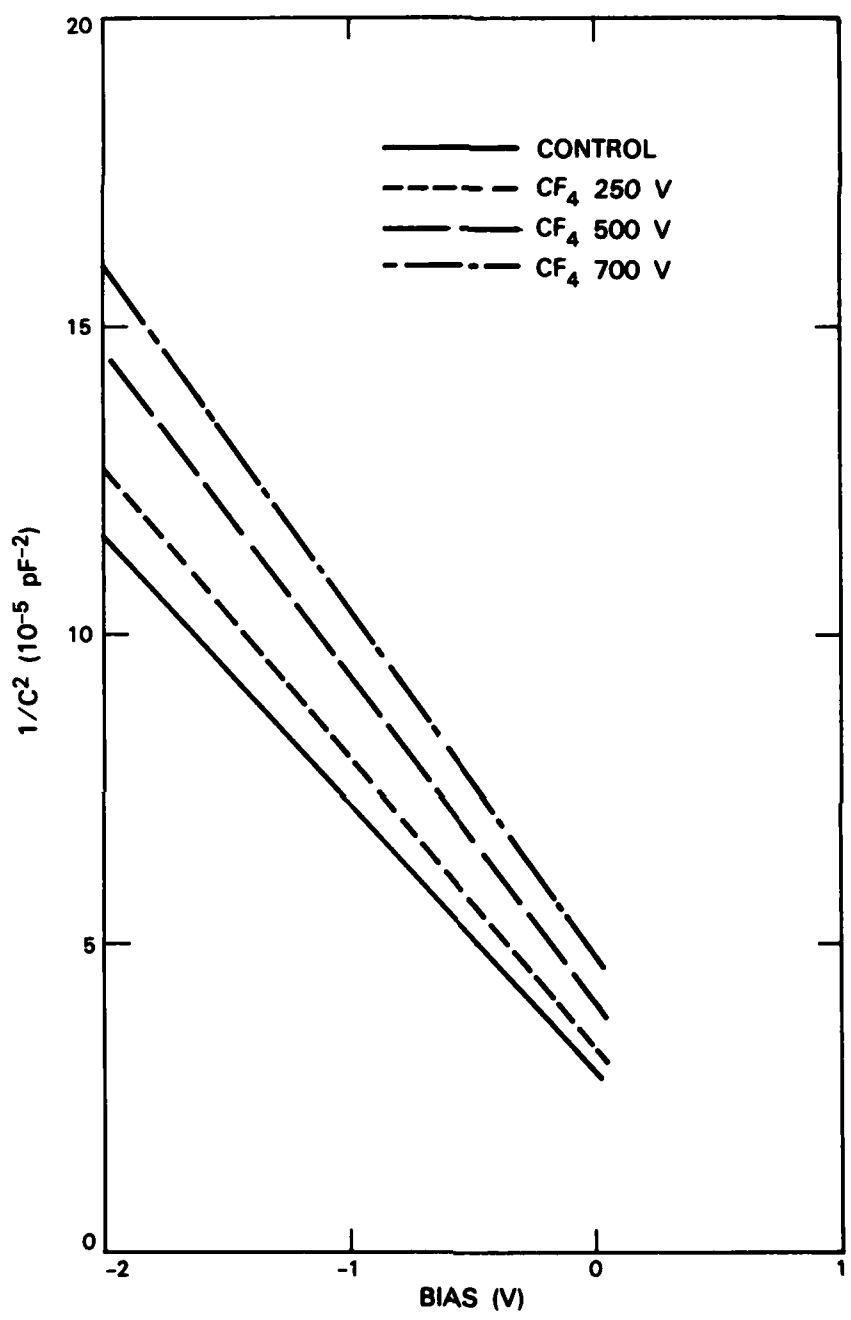


Figure 4-4. Capacitance-voltage plot for a control sample, and for samples reactive-ion etched in  $\text{CF}_4$  at 250, 500, and 700 V.

138891-N

The basic design of the reactor is a conventional  $\text{AsCl}_3$ -GaAs-H<sub>2</sub> system used to grow GaAs epitaxial layers at 700° to 750°C. The most important modification for low temperature growth is the addition of AsH<sub>3</sub> to the gas flow over the GaAs source. Results of experiments with epitaxial films grown with and without AsH<sub>3</sub> indicate that the films grown with AsH<sub>3</sub> have superior properties.

The GaAs substrates used in this study were oriented 5° off of the [100] direction toward [111]. The substrates used for measuring growth rate and carrier concentration of the epitaxial films were n<sup>+</sup> silicon-doped, while the van der Pauw measurement films were grown on Cr-doped, semi-insulating substrates. After growth, the thickness and carrier concentration of the epitaxial films were determined using C-V measurements made with a mercury-probe Schottky barrier. For epitaxial films thicker than 1 μm, the thickness was measured from a stained, cleaved cross section.

The epitaxial growth process can be discussed in terms of the effects of four variables: AsCl<sub>3</sub> partial pressure, AsH<sub>3</sub> partial pressure, GaAs source temperature, and dopant partial pressure. A series of epitaxial GaAs films were grown with a constant source temperature and a partial pressure of AsCl<sub>3</sub> that varied by a factor of 40. The growth rate was found to vary by less than 30% when comparing samples with a similar ratio of  $P(\text{AsH}_3)/P(\text{AsCl}_3)$ . However, a factor-of-3 increase in this ratio resulted in a 40-percent decrease in growth rate. This leads to the interesting conclusion that, as long as  $P(\text{AsH}_3)/P(\text{AsCl}_3)$  is held constant, the AsCl<sub>3</sub> partial pressure is a noncritical variable in determining the growth rate, while varying  $P(\text{AsH}_3)/P(\text{AsCl}_3)$  with AsCl<sub>3</sub> partial-pressure constant produces a large effect on growth rate. This is indicated by the data of Figure 4-5 which shows the growth rate as a function of combined AsH<sub>3</sub> and AsCl<sub>3</sub> partial pressures for three GaAs source temperatures and a constant AsCl<sub>3</sub> partial pressure.

The growth rate as a function of source temperature is shown in Figure 4-6 for two AsH<sub>3</sub> partial pressures. As expected, a higher source temperature increases the level of GaCl, thereby increasing the growth rate. The saturation in the growth rate with increasing source temperature is due, we believe, to nucleation of GaAs on the reactor quartzware.

The dependence of carrier concentration in the layers upon the partial pressure of H<sub>2</sub>S was as expected. An increase in dopant partial pressure produces an increase in carrier concentration. The concentration of dopant gas required for a given carrier concentration was similar to concentrations required at growth temperatures in the 700° to 750°C range.

The carrier concentration was also found to depend on the source temperature and AsH<sub>3</sub> partial pressure. A reduction in carrier concentration with increasing source temperature is shown in Table 4-4 for a constant AsCl<sub>3</sub> partial pressure at  $1.4 \times 10^{-3}$  atm. Since the higher source temperature causes a higher growth rate (as shown in Figure 4-6) while the arrival rate of sulfur remains constant, the sulfur concentration per unit volume is reduced. The effect of the AsH<sub>3</sub> concentration on the carrier concentration is given in Table 4-5 for a constant AsCl<sub>3</sub> partial pressure of  $1.4 \times 10^{-3}$  atm. The increase in doping of the epitaxial films with higher AsH<sub>3</sub> levels is due in part to the decreasing growth rate.

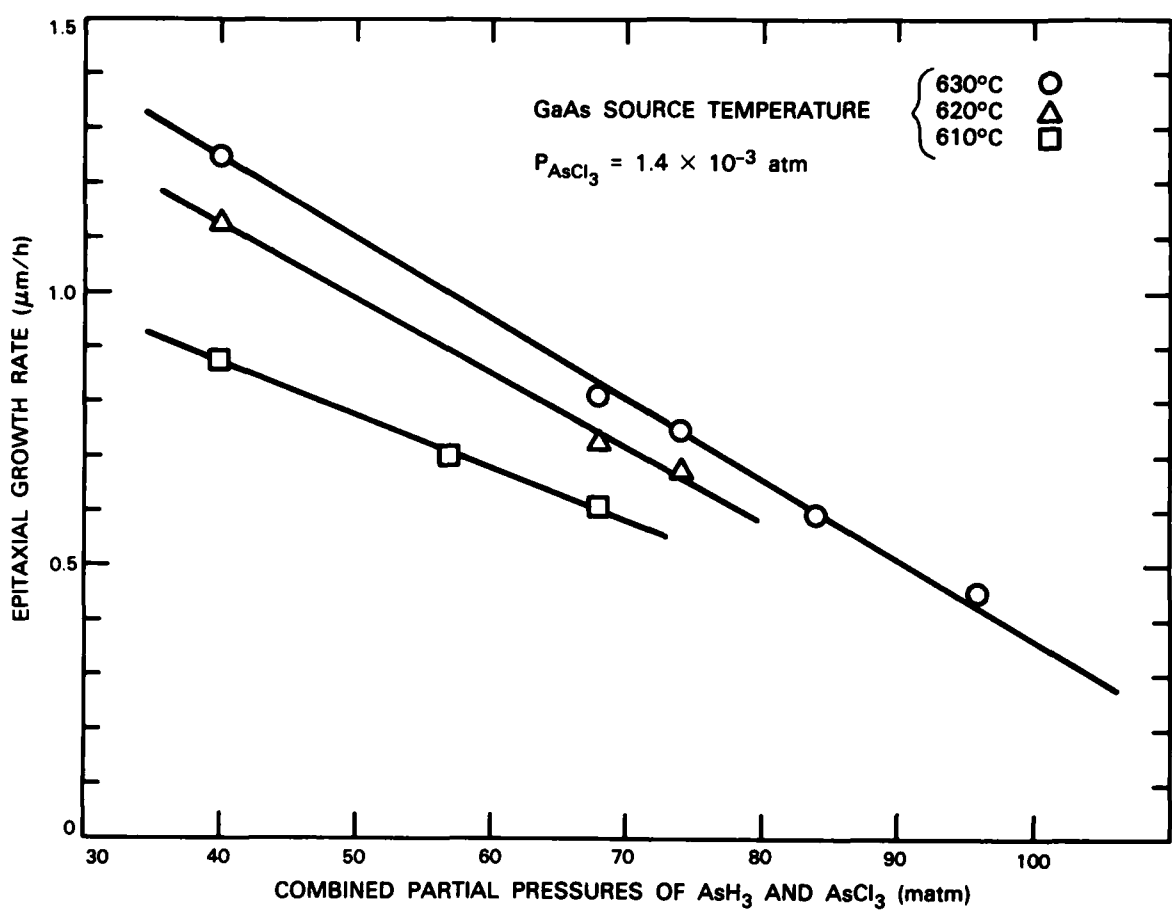


Figure 4-5. Epitaxial growth rate as a function of combined partial pressures of  $\text{AsH}_3$  and  $\text{AsCl}_3$  for various GaAs source temperatures.

However, impurities in the  $\text{AsH}_3$  (such as  $\text{GeH}_4$ ) may also contribute to the dependence of carrier concentration on the  $\text{AsH}_3$  partial pressure. One conclusion from these data is that the lowest possible  $\text{AsH}_3$  partial pressure is desirable when trying to obtain high-purity films. There is, however, a lower limit for the  $\text{AsH}_3$  pressure where the surface morphology and electrical properties degrade drastically.

To measure the electron mobility of GaAs films, thicker layers (1.5 to 3  $\mu\text{m}$ ) were grown on semi-insulating substrates. After fabricating four ohmic contacts by alloying tin into the GaAs, the carrier concentration and Hall electron mobility were then calculated from van der Pauw measurements.<sup>9</sup> Measurements were made on films grown at a source temperature of 665°C, an  $\text{AsH}_3$  partial pressure of  $3.9 \times 10^{-2}$  atm, and an  $\text{AsCl}_3$  partial pressure of  $1.4 \times 10^{-3}$  atm. For an n-type epitaxial GaAs film with a carrier concentration

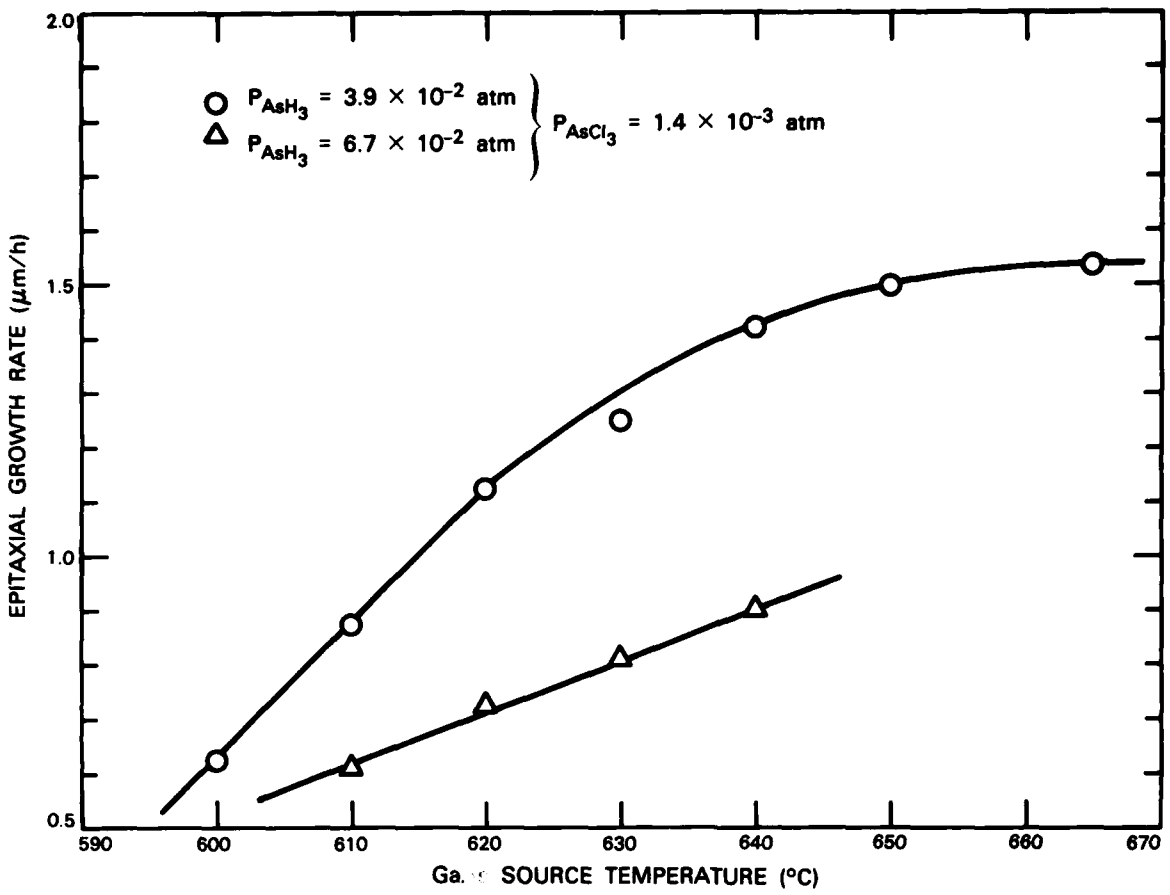


Figure 4-6. Epitaxial growth rate as a function of GaAs source temperature for a constant  $\text{AsCl}_3$  partial pressure and two  $\text{AsH}_3$  partial pressures.

of  $1.2 \times 10^{17} \text{ cm}^{-3}$ , the room-temperature and liquid-nitrogen mobilities were 3900 and  $4200 \text{ cm}^2/\text{V}\cdot\text{s}$ , respectively. Several n-type layers with carrier concentrations in the range  $5.6$  to  $6.9 \times 10^{16} \text{ cm}^{-3}$  were found to have room-temperature Hall mobilities in the range 4300 to  $4100 \text{ cm}^2/\text{V}\cdot\text{s}$  and liquid-nitrogen mobilities in the range 6000 to  $5500 \text{ cm}^2/\text{V}\cdot\text{s}$ . For the sample with a carrier concentration of  $5.6 \times 10^{16} \text{ cm}^{-3}$  and a 77 K Hall mobility of  $6000 \text{ cm}^2/\text{V}\cdot\text{s}$ , the total ionized impurity concentration ( $N_D + N_A$ ) was calculated<sup>10</sup> to be  $1.3 \times 10^{17} \text{ cm}^{-3}$ , which corresponds to 40-percent compensation ( $N_A/N_D$ ). This compensation, calculated<sup>11</sup> from the liquid-nitrogen mobility, compares well with the 43-percent compensation calculated from the room-temperature mobility.

It has been shown that VPE growth of GaAs at 500°C using chloride transport is possible. The epitaxial films have free carrier concentrations useful for device applications and reasonable mobilities for n-type GaAs. Specular surfaces are routinely achieved for epitaxial films grown at 500°C for sufficiently high  $\text{AsH}_3$  partial pressures. On the other hand, low

TABLE 4-4

## Carrier Concentration Dependence on Dopant Partial Pressure

Sample Number	GaAs Source Temperature (°C)	P(AsH <sub>3</sub> ) (10 <sup>-3</sup> atm)	P(H <sub>2</sub> S) (10 <sup>-9</sup> atm)	Carrier Concentration (10 <sup>16</sup> cm <sup>-3</sup> )
12	610	39	50	3.7
14	620	39	50	3.0
18	630	67	50	1.1
13	610	67	50	6.2
15	620	67	50	6.2
25	620	67	50	5.4

TABLE 4-5

## Carrier Concentration Dependence on Arsine Partial Pressure

Sample Number	GaAs Source Temperature (°C)	P(AsH <sub>3</sub> ) (10 <sup>-3</sup> atm)	P(H <sub>2</sub> S) (10 <sup>-9</sup> atm)	Carrier Concentration (10 <sup>16</sup> cm <sup>-3</sup> )
12	610	39	50	3.7
13	610	67	50	6.2
14	620	39	50	3.0
15	620	67	50	5.4
19	630	30	0	0.5
20	630	67	0	2.4
21	630	78	0	4.0
22	630	83	0	4.6

$\text{AsH}_3$  partial pressures result in GaAs films with large trap levels and surfaces marred by hillocks and vapor-liquid-solid growth whiskers. Growth rates from 0.5 to 1.5  $\mu\text{m}/\text{h}$  were obtained, with the maximum growth rate of high-quality GaAs limited to 1.5  $\mu\text{m}/\text{h}$  by, we believe, nucleation on the quartz reactor walls.

K.B. Nichols  
C.O. Bozler

#### 4.4 LARGE-AREA ION-BEAM-ASSISTED ETCHING OF GaAs WITH HIGH ETCH RATES AND CONTROLLED ANISOTROPY

Ion-beam-assisted etching (IBAE) is an anisotropic dry-etching technique in which the sputter etching component of an ion beam and the chemical etching component of a reactive gas flux are independently controlled. The results reported here are achieved with an improved IBAE system which was designed to etch GaAs for device fabrication. The IBAE system, shown schematically in Figure 4-7, consists of a 2.5-cm Kaufman ion source, one or more gas jets, and a liquid-nitrogen cold trap. This system is similar to earlier reported units<sup>12,13</sup> with the exception of the addition of a cold trap. This trap efficiently pumps the unused reactive gas from the jets, and the reaction products from the etching process. This enhanced pumping makes it possible to flood the sample with a reactive gas flux equivalent to a pressure of  $2 \times 10^{-2}$  Torr, while maintaining a chamber pressure in the  $1 \times 10^{-4}$  Torr range, which is necessary for the operation of the ion source.

Reactive fluxes equivalent to pressures in the range of  $1 \times 10^{-3}$  to  $2 \times 10^{-2}$  Torr are important to minimize surface damage during etching,<sup>13,14</sup> to control the etching uniformity, and to obtain rapid etching rates. Ion-beam sputtering is known to damage crystal surfaces, and the addition of a  $\text{Cl}_2$  flux has been shown to reduce this damage significantly. With the improved IBAE system, and better control of the reactive flux, the surface damage has been reduced further. The etching rate of GaAs varies with the reactive  $\text{Cl}_2$  flux. For reactive pressures less than  $1 \times 10^{-3}$  Torr the etching rate is a strong function of the reactive flux, and small variations in the reactive flux can cause considerable variations in the etching rate over the sample surface. To avoid this difficulty, the etching is usually performed at reactive pressures in excess of  $2 \times 10^{-3}$  Torr. The additional pumping speed of the cold trap allows for uniform coverage of the sample with reactive flux at equivalent pressures in excess of  $2 \times 10^{-3}$  Torr, making it possible to etch 5-cm-diam wafers and obtain  $\pm 5$ -percent uniformity over a 4- $\text{cm}^2$  area. This uniformity reflects variation of both the ion beam and the reactive flux over the sample. The effect that ion beam collimation has on the etched structure is depicted in Figure 4-8(a-b). An undercut structure that results from poor ion-beam collimation is illustrated in Figure 4-8(a). By increasing the ion source to sample distance, as shown in Figure 4-8(b), the collimation is improved and the undercutting is reduced. Collimation is determined to first order by the ratio of the beam diameter at the ion source to the sample-ion source distance. Figure 4-9(a) shows the resulting profile obtained with a 2.5-cm-diam ion beam and a sample-to-source distance of 19 cm. The angular

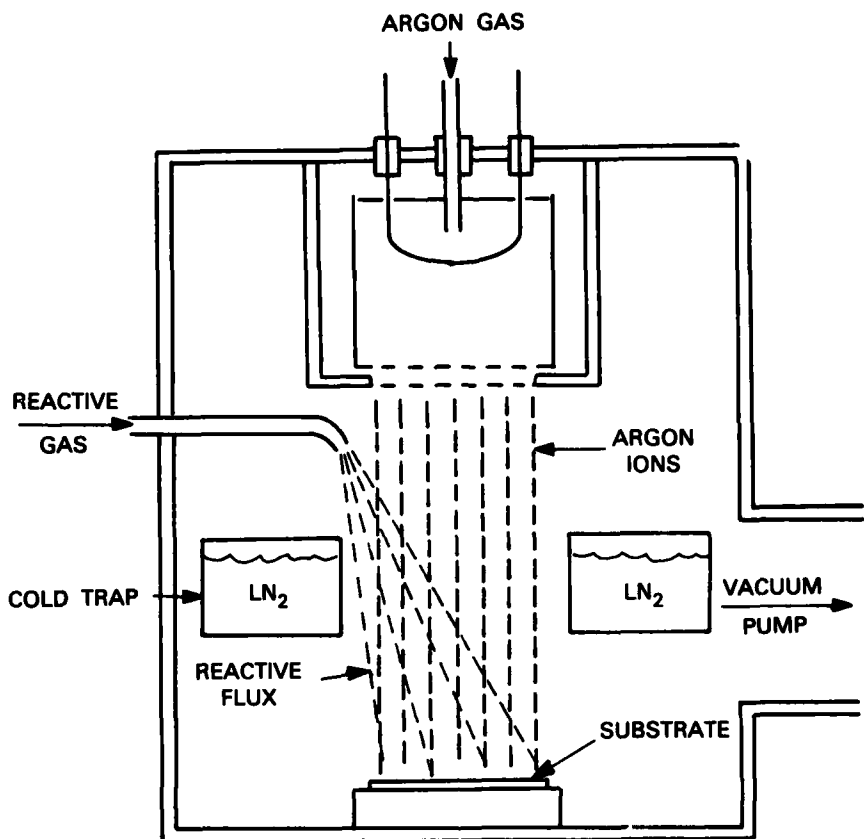


**Figure 4-7.** Schematic diagram of IBAE system which consists of an ion source, one or more reactive gas jets (only one shown), and a cold trap to pump unused reactive gas and reaction products. Stainless-steel vacuum chamber is pumped either with a cryopump or a cold trapped diffusion pump.

spread of the ion beam is about  $\pm 4^\circ$ , which is approximately equal to the  $5^\circ$  of undercutting of the profile. The profile shown in Figure 4-9(b) was obtained using the same etching parameters but with the sample-to-source distance increased to 45.5 cm, resulting in an angular spread of about  $\pm 1.5^\circ$ . Structures with aspect ratios in excess of 40:1 have been etched with this increased sample-to-source distance and reactive fluxes equivalent to  $2 \times 10^{-2}$  Torr. Figure 4-10 shows a profile obtained in GaAs with an aspect ratio in excess of 10:1.

The IBAE system reported here is capable of etching up to 5-cm-diam wafers with an etching uniformity of  $\pm 5$  percent over a  $4\text{-cm}^2$  area. The independent control of the ion beam and the reactive flux makes it possible to etch extremely high aspect ratio structures with minimal surface damage to GaAs substrates. Etching rates of 5 to  $10 \mu\text{m min}^{-1}$  are easily obtainable, making it possible to etch substrate throughholes in a few minutes. This

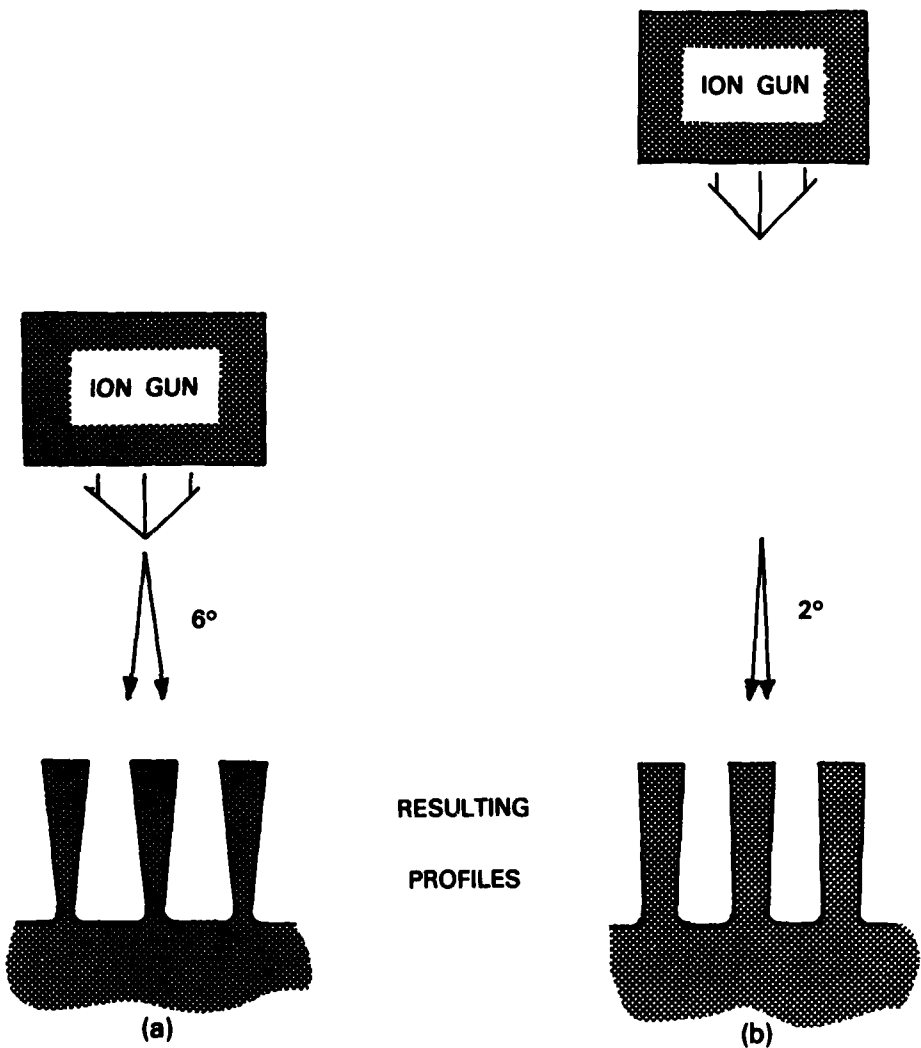
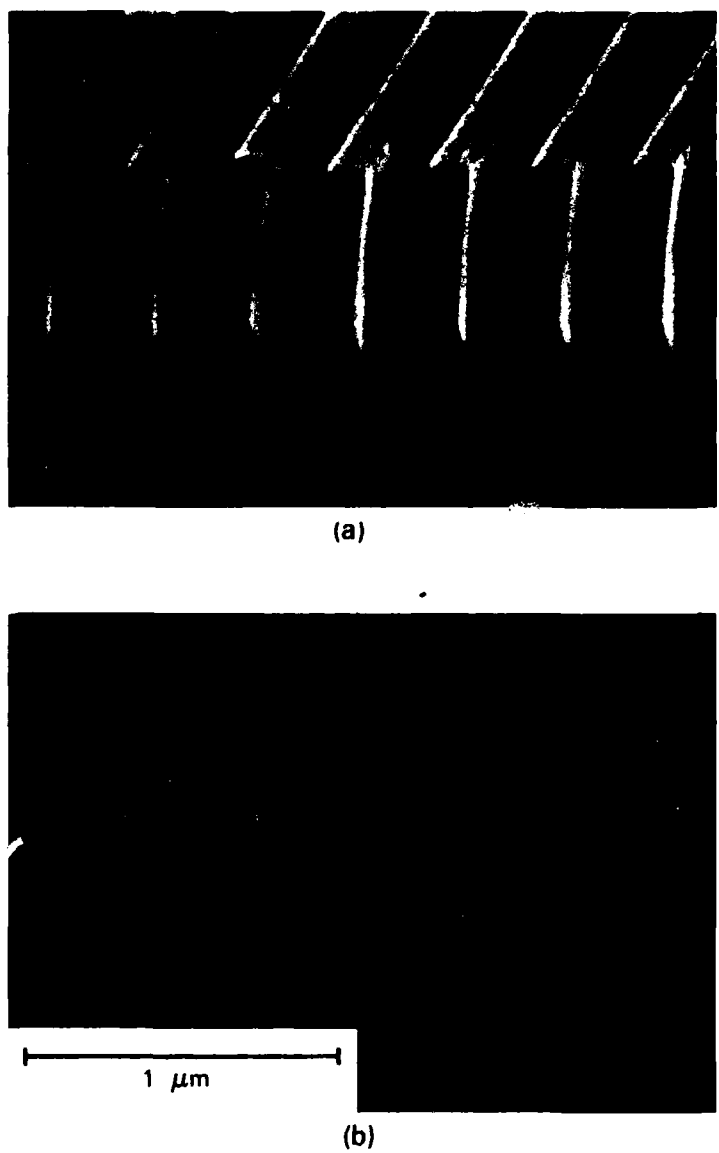


Figure 4-8(a-b). Diagram showing effect of ion source to sample distance on profile of etched structure.



**Figure 4-9.** Scanning electron micrographs of GaAs samples etched with (a) a sample-to-source distance of 19 cm, and (b) a sample-to-source distance of 45.5 cm. A  $20\text{-}\mu\text{A cm}^{-2}$  beam of 500-eV Ar<sup>+</sup> and an equivalent reactive flux of  $2 \times 10^{-3}$  Torr were used to obtain these profiles.



Figure 4-10. Scanning electron micrograph of a GaAs sample etched under same conditions as sample shown in Figure 4-9(b). Grating is etched to about a 1.5- $\mu$ m depth.

system, which is discussed in more detail elsewhere,<sup>15</sup> is presently being used to etch submicrometer structures for devices.

G.A. Lincoln      S. Pang  
M.W. Geis      N.N. Efremow

#### 4.5 SUBMICROMETER GATES FOR FIELD-EFFECT TRANSISTORS

Submicrometer-gate FETs have previously been fabricated using scanning electron-beam lithography.<sup>16</sup> Although electron-beam lithography is widely used in the research community,<sup>17,18</sup> there has been an increased effort in commercial companies<sup>19,20</sup> to develop the capability for fabricating submicrometer-gate FETs using conventional lithography. The driving force is to produce low-cost and high-performance devices for microwave applications.

These objectives are common to GaAs monolithic circuits under development here. For this reason we are investigating several techniques for producing submicrometer gates. One promising approach is the use of deep ultraviolet lithography for the replication of submicrometer features. In this technique, patterns are defined on a quartz mask and replicated

on a GaAs wafer coated with a layer of PMMA. This operation is performed using a contact printer constructed here, which consists of an alignment module and a deep ultraviolet light source with output wavelengths in the 200-nm region. An example of a submicrometer gate is shown in Figure 4-11. The "T"-shaped cross section is fabricated by means of a lift-off process, and its purpose is the reduction of gate resistance.



Figure 4-11. Submicrometer T-shaped gate fabricated using deep ultraviolet lithography.

Another approach is to reduce the size of features, defined using conventional lithography, by using a special process sequence. Such unconventional processing techniques are not yet fully proven. The scanning electron micrograph in Figure 4-12 shows an example of a plated and recessed submicrometer-gate FET. Devices fabricated using this process sequence have been tested, and RF results are shown in Figure 4-13. Maximum stable gain and maximum available gain are plotted as a function of frequency. The maximum available gain of 6.5 dB at 18 GHz shows promise, although further development of the process is necessary.

A. Chu

L.J. Mahoney

D.J. Burrows

W.J. Piacentini

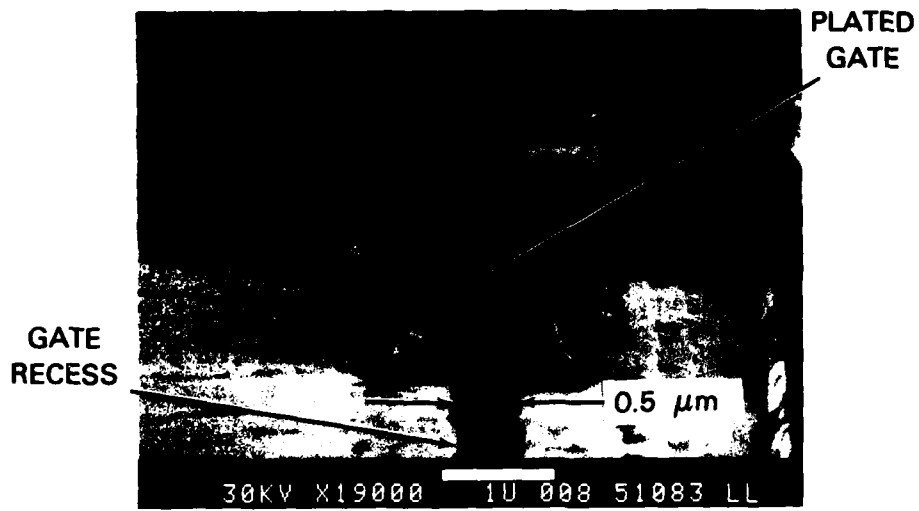


Figure 4-12. Plated and recessed submicrometer-gate FET.

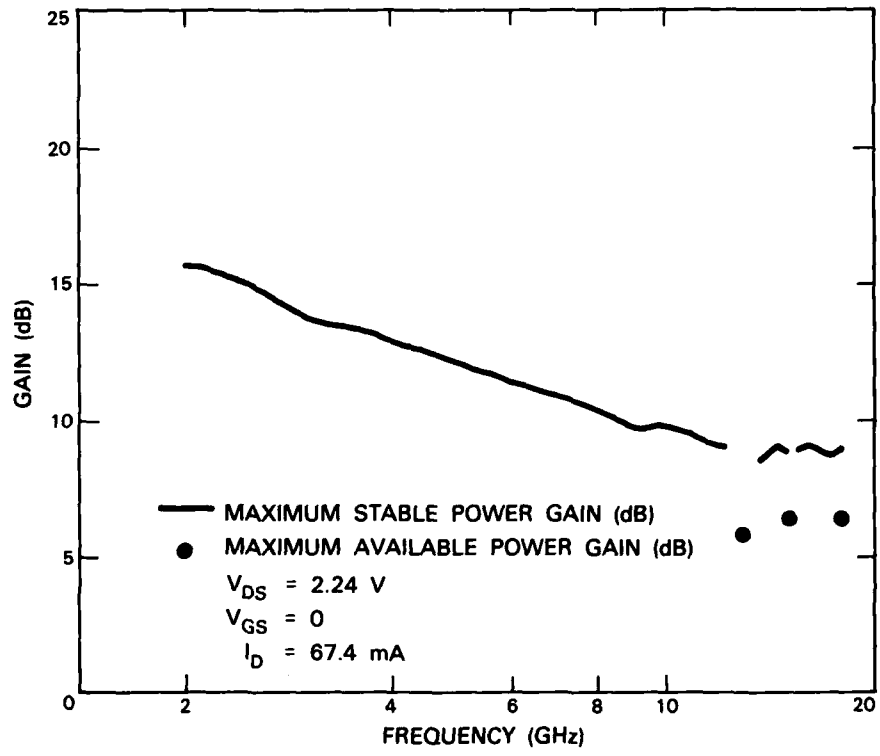


Figure 4-13.  $0.5 \times 150\text{-}\mu\text{m}$  gate FET.

#### 4.6 PLANAR GaAs PIN PHOTODIODE WITH PICOSECOND TIME RESPONSE

The development of optical signal processing and optical communication systems has created the need for ultrafast photodetectors to achieve high data rates. Very fast response times have been obtained with GaAs Schottky photodiodes.<sup>21</sup> Here, we report the development and characterization of a high-speed planar GaAs PIN photodiode which exhibits an impulse response of 19-ps FWHM to 4-ps pulses from a near-infrared laser. Because of its design characteristics, the photodiode is ideally suited for fiberoptic coupling of the light directly into the intrinsic layer. Since the device has planar contacts, it can easily be integrated into optoelectronic circuits.

As illustrated in Figure 4-14, the planar diode is fabricated on a semi-insulating GaAs substrate on which a sequence of active layers has been grown in a vapor-phase-epitaxial reactor. The 2- $\mu\text{m}$ -thick intrinsic layer has an n-type background concentration of  $10^{13} \text{ cm}^{-3}$ . The device is isolated by means of mesa etching and proton bombardment. This permits the subsequent fabrication of large planar electrodes that access the small anode and cathode contacts of the device, a configuration that is essential for obtaining low parasitic capacitances. In the high-speed test package, the large electrodes are bonded to  $50\text{-}\Omega$  microstrip lines which are connected to SMA microstrip launchers. The photosensitive area not covered by metal measures  $300 \mu\text{m}^2$ . The capacitance of the device is  $\sim 15 \text{ fF}$ , and the carrier transit time through the intrinsic layer is estimated to be 20 ps. The photodiode has a reverse breakdown voltage in excess of 25 V; however, the device can be operated at a low reverse bias voltage of 1 to 2 V.

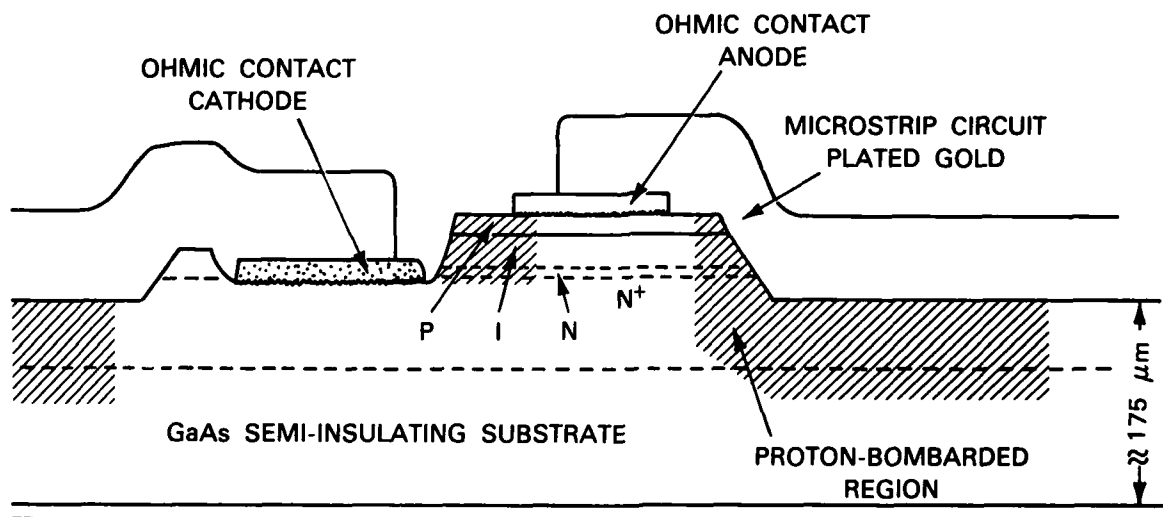


Figure 4-14. Cross section of planar GaAs PIN photodiode.

126183-N-04

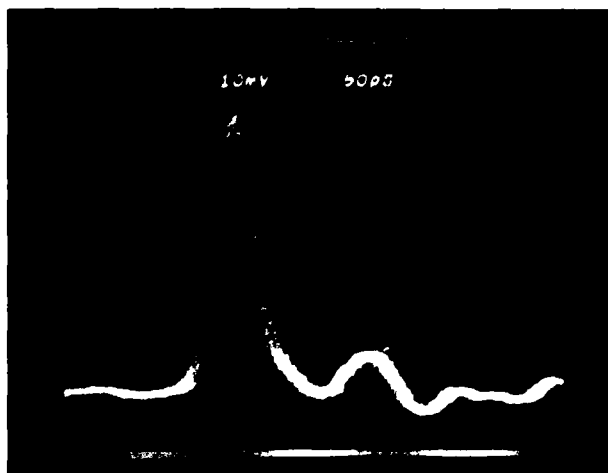


Figure 4-15. Impulse response of planar GaAs PIN photodiode biased at -1.5 V.

The time response of the device has been measured using the near-infrared pulses from a synchronously pumped oxazine 750 dye laser. Figure 4-15 shows the impulse response of the photodiode to a 4-ps laser pulse at  $\lambda = 757$  nm as monitored with a sampling oscilloscope having a 25-ps rise time. Because of the limited time resolution of the instrument, the observed pulse is broadened to a FWHM of 45 ps. To improve the time resolution, a picosecond optoelectronic correlation technique<sup>22</sup> was employed. The photodiode was attached to a special 50- $\Omega$  microstrip circuit which contained a photoconducting sampling gate fabricated from amorphous Si. This measurement technique gives the correlation function of the photodiode time response and the 17.5-ps aperture time of the photoconductive gate, the latter having been calibrated in a separate experiment. The correlation trace shown in Figure 4-16 has a FWHM of 26 ps. This yields a value of 19 ps [ $\sqrt{(26)^2 - (17.5)^2}$  ps] for the FWHM impulse response of the planar GaAs PIN photodiode to the 4-ps dye-laser pulses at  $\lambda = 757$  nm. The external quantum efficiency of the photodiode, biased at -1.5 V, was found to exceed 10 percent within the 740- to 820-nm tuning range of the dye laser. The generated photocurrent increases linearly with the impinging light intensity. The observed results suggest that the measured impulse response is transit time limited. Theoretical analysis of PIN diode operation based upon the material parameters of GaAs indicates that even faster impulse response and better sensitivity can be achieved by optimizing the device design.

W. Lenth  
W.E. Barch  
A. Chu  
L.J. Mahoney

R.W. McClelland  
R.W. Mountain  
D.J. Silversmith

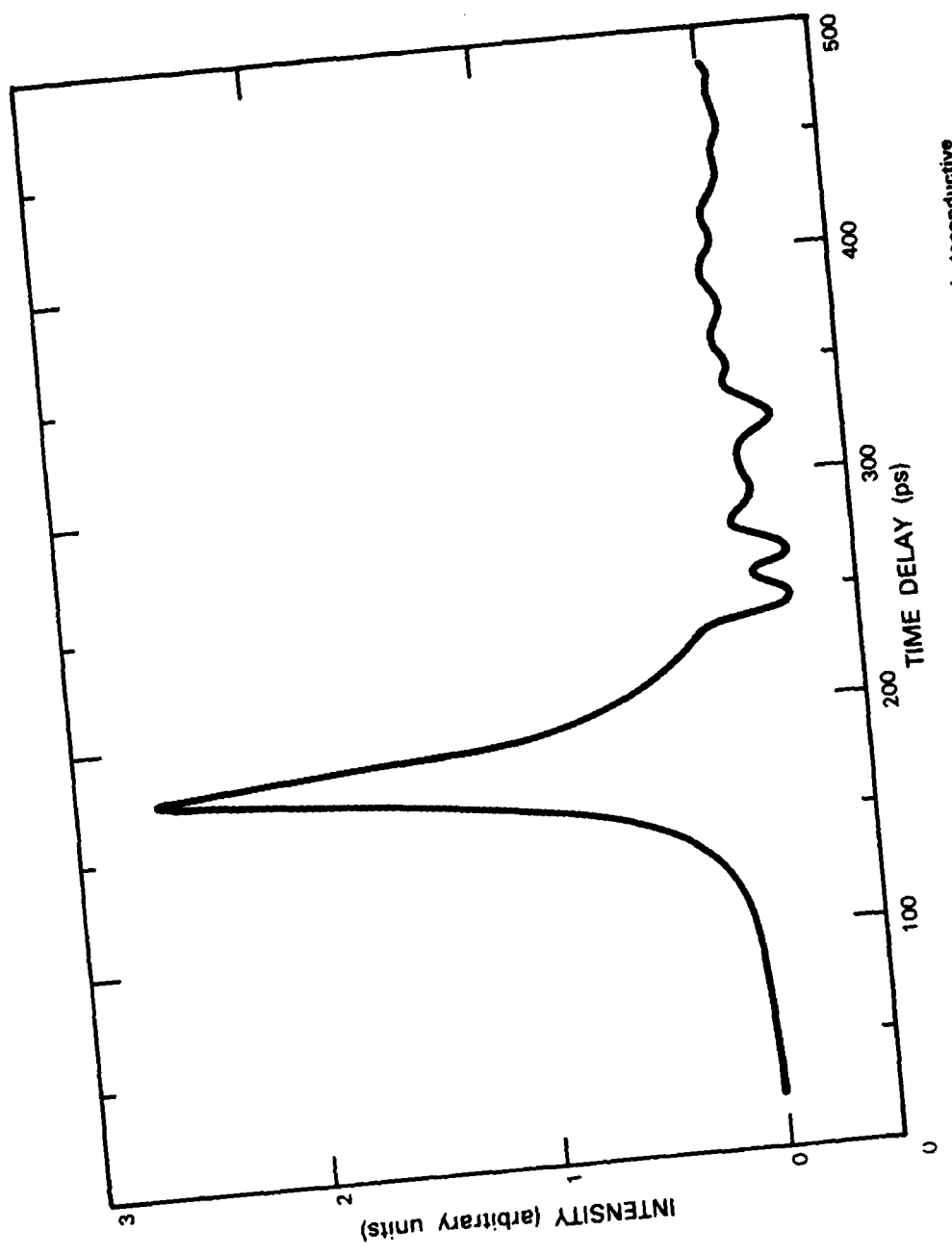


Figure 4-16. Correlation measurement of planar GaAs PIN photodiode and a photoconductive sampling gate.

## REFERENCES

1. Solid State Research Report, Lincoln Laboratory, M.I.T. (1981:3), pp. 45-49, DTIC AD-A112696/0.
2. *Ibid.* (1982:2), pp. 59-63, DTIC AD-A122252.
3. *Ibid.* pp. 55-58.
4. *Ibid.* (1983:3), pp. 64-68.
5. B.E. Burke and D.L. Smythe, IEEE J. Solid-State Circuits **18**, 736 (1983).
6. G.A. Lincoln, M.W. Geis, L.J. Mahoney, A. Chu, B.A. Vojak, K.B. Nichols, W.J. Piacentini, N.N. Efremow, and W.T. Lindley, J. Vac. Sci. Technol. **20**, 786 (1982).
7. S.W. Pang, G.A. Lincoln, R.W. McClelland, P.D. DeGraff, M.W. Geis, and W.J. Piacentini, J. Vac. Sci. Technol. B **1**, 1334 (1983).
8. M.W. Geis, G.A. Lincoln, N.N. Efremow, and W.J. Piacentini, J. Vac. Sci. Technol. **19**, 1390 (1981), DTIC AD-A117772/4; G.A. Lincoln, M.W. Geis, S.W. Pang, and N.N. Efremow, J. Vac. Sci. Technol. B **1**, 1043 (1983).
9. L.J. van der Pauw, Philips Res. Rep. **13**, 1 (1958).
10. G.E. Stillman and C.M. Wolfe, Thin Solid Films **31**, 69 (1976), DTIC AD-A024175/2.
11. W. Walukiewicz, L. Lagowski, L. Jastrzebski, M. Lichtensteiger, and H. Gatos, J. Appl. Phys. **50**, 899 (1979).
12. M.W. Geis, G.A. Lincoln, N.N. Efremow, and W.J. Piacentini, J. Vac. Sci. Technol. **19**, 1390 (1981), DTIC AD-A117772/4.
13. G.A. Lincoln, M.W. Geis, L.J. Mahoney, A. Chu, B.A. Vojak, K.B. Nichols, W.J. Piacentini, N.N. Efremow, and W.T. Lindley, J. Vac. Sci. Technol. **20**, 786 (1982).
14. S.W. Pang, G.A. Lincoln, R.W. McClelland, P.D. DeGraff, M.W. Geis, and W.J. Piacentini (submitted to J. Vac. Sci. Technol.).
15. G.A. Lincoln, M.W. Geis, S. Pang, and N.N. Efremow, J. Vac. Sci. Technol. B **1**, 1043 (1983).
16. Solid State Research Report, Lincoln Laboratory, M.I.T. (1980:2), pp. 33-35, DTIC AD-A092724/4.

17. E.T. Watlains, J.M. Schellenberg, L.H. Hackett, H. Yamasaki, and M. Feng, "A 60 GHz GaAs FET Amplifier," 1983 IEEE MTT-S International Microwave Symposium Digest, pp. 145-147.
18. P.C. Chao, P.M. Smith, S. Wanuga, J.C.M. Hwang, W.H. Perkins, R. Tiberis, and E.D. Wolf, "Electron-Beam Fabrication of Quarter-Micron T-Shaped-Gate FETs Using a New Tri-Layer Resist System," 1983 IEEE MTT-S International Microwave Symposium Digest, pp. 613-616.
19. J. Rosenberg, C. Chye, C. Huang, and G. Policky, "A 26.5 to 40 GHz FET Amplifier," 1983 IEEE MTT-S International Microwave Symposium Digest, pp. 166-168.
20. Y.H. Yun, G.C. Taylor, D.S. Bechtle, S.T. Jolly, S.G. Liu, and R.L. Camisa, "Ka Band GaAs Power FETs," 1983 IEEE MTT-S International Microwave Symposium Digest, pp. 136-138.
21. S.Y. Wang and D.M. Bloom, Electron. Lett. **19**, 554 (1983).
22. D.H. Auston and P.R. Smith, Appl. Phys. Lett. **41**, 599 (1982).

## 5. ANALOG DEVICE TECHNOLOGY

### 5.1 INTEGRATION OF MULTIPLE ELASTIC CONVOLVERS INTO A COMMUNICATION SIGNAL PROCESSOR

High-performance monolithic elastic convolvers with 100-MHz bandwidth have been developed for operation in a prototype spread-spectrum communication network. The system provides 90-kHz and 1.4-MHz data rates for different system environments. To process signals at these respective rates, different convolvers are provided. Long (22- $\mu$ s) devices provide 30 dB of processing gain at the low data rate for high-noise environments, and short (1.4- $\mu$ s) convolvers are used in low-noise environments for high-data-rate communication.

The long convolvers use segmented output electrode for differential-phase-shift-keyed (DPSK) data demodulation.<sup>1,2</sup> In DPSK, the data are coded by a 0°/180° phase flip between adjacent waveform segments. The interaction region of the convolver spans two 11- $\mu$ s segments. The reference must be applied as a time-reversed waveform 22  $\mu$ s long. A single convolver can provide only one bit decision every 22  $\mu$ s by comparing its two outputs and, therefore, two convolvers are required with time-staggered references to provide continuous output at a 90-kHz rate.

The precise time of arrival for signal components has uncertainty because of direct and multiple-indirect transmission paths ("multipath"). While an uncertainty of the order of 1  $\mu$ s causes minor degradation in the long-convolver output, it prevents the use of the same DPSK demodulation scheme with the short convolver. Binary orthogonal keying (BOK) was selected for modulation in the high-data-rate mode. Each 700-ns block is coded by a 0°/180° phase flip at midpoint, and separate convolvers with flipped and unflipped references are required for demodulation. As with the long convolvers, two sets are required for continuous output for a total of four short convolvers.

The four short and two long convolvers are connected through a PIN-diode switch matrix which provides data-rate mode selection as well as commutation for continuous output. This switch matrix and the six convolvers have been integrated into one modular package.

A photograph of the long-convolver subassembly is shown in Figure 5-1. A single signal port on the left of the housing drives input transducers for two identical dual-track convolvers.<sup>3</sup> The reference transducers are driven through separate matching circuits to permit independent application of those waveforms. Each LiNbO<sub>3</sub> convolver includes a pair of electrically orthogonal signal/reference transducers at opposite ends of the substrate. The transducers are slightly chirped to compensate for waveguide dispersion. They drive the dual-track waveguide structure through two pairs of 0.5- $\mu$ s-long parabolic-horn beam-width compressors. The waveguide of the dual-track convolver is three wavelengths wide, segmented into two 11- $\mu$ s-long sections with eight equally spaced output taps on each section. The taps from one waveguide are parallel bonded to a low-impedance-output summing bus while the

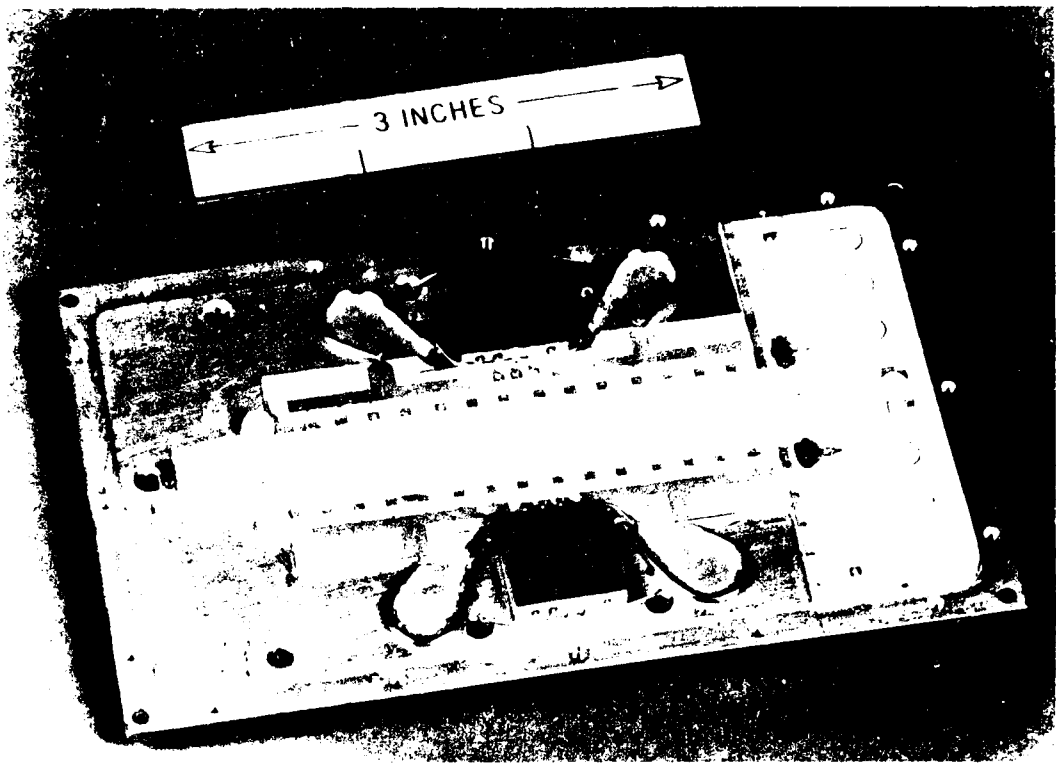


Figure 5-1. Long-convolver subassembly.

adjacent waveguide is grounded.  $10\text{-}\Omega$ -impedance coaxial lines from the summing buses provide impedance matching to the input ports of sum-difference hybrids incorporated into the package for continuous DPSK demodulation. The convolver features summarized here were developed to suppress self-convolution, minimize phase dispersion, reduce long-line effects in the output circuit, and to simplify output matching. The concepts and early results have been described previously in detail.<sup>3</sup>

The short-convolver subassembly is shown in Figure 5-2. Four  $1.4\text{-}\mu\text{s}$ -long convolvers are shown in the lower view. The signal input transducers near the center of the substrate are parallel connected in pairs, and driven simultaneously through the power divider. The separate reference transducers are matched to  $50\ \Omega$  using  $1.4$ -wavelength microstrip impedance inverters. Each of the four  $1.4\text{-}\mu\text{s}$ -long convolver segments is connected to one of the four output ports through a series tuning inductor. Short-convolver design features are carried over from the long-convolver design, and fabrication details differ only in the thicker metallization of the waveguide. The added phase dispersion caused by the increased mass loading of the short waveguide section is compensated by the same slightly chirped transducers designed for the long convolver, thereby simplifying production.

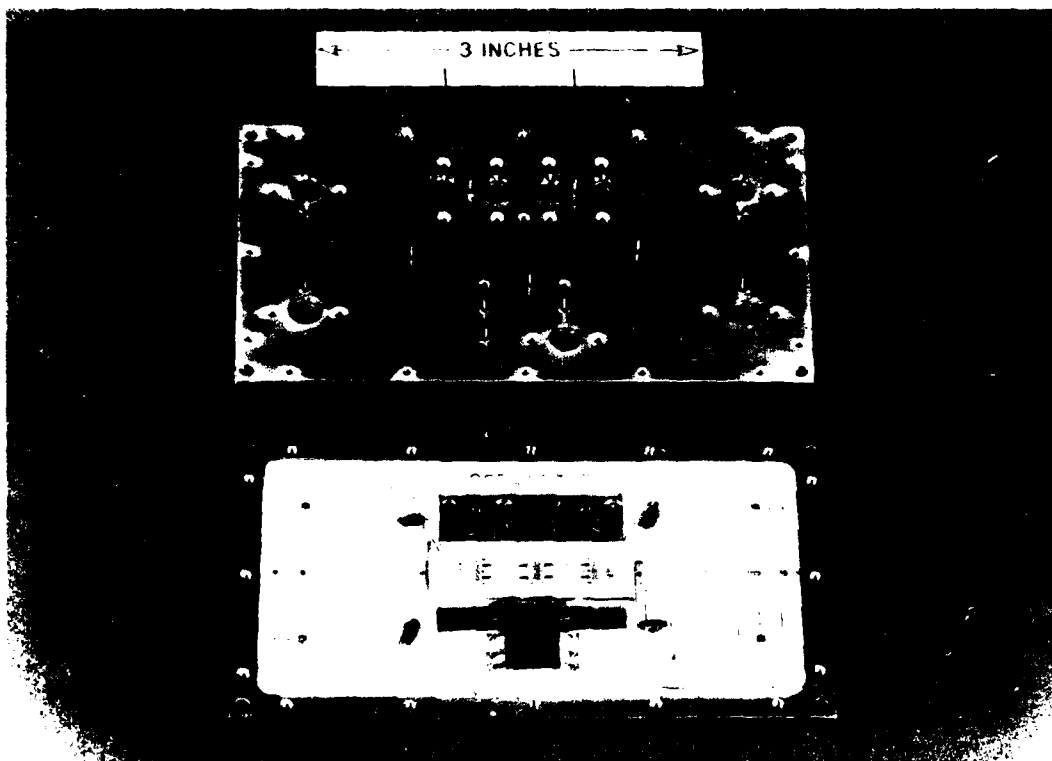


Figure 5-2. Short-convolver subassembly.

The upper view in Figure 5-2 shows input/output pin connections on the underside of the device package. When plugged into the module, this pin arrangement provides a low-profile board assembly. For preliminary testing and matching of the convolvers, shield housings are available which conveniently mate with the pins to provide standard SMA connectors.

Table 5-1 summarizes the measured device characteristics of the long and short convolvers.

Consistent with a compact radio-receiver design, all convolvers were mounted on a single printed-circuit module containing the associated commutating and mode-selection switch matrix. Convolver input and output locations on the board were chosen to minimize feedthrough.

The convolvers described above are high-performance devices. In order not to degrade this performance, the module circuit performance criteria were set as in Table 5-2.

A block diagram of the switching matrix is shown in Figure 5-3. A hybrid power splitter provides a continuous signal input to all convolvers. The loss of input signal level by this power division is compensated by amplification rather than switching to minimize

**TABLE 5-1**  
**Elastic Convolver Characteristics**

	Long	Short
Center Frequency (MHz)	300	300
Bandwidth (3 dB) (MHz)	100	100
Deviation from Linear Phase (deg)	<±30	<±30
Efficiency (dBm)	-72	-73
Dynamic Range <sup>†</sup> (dB)	59	58
Self-Convolution Suppression (dB)	>40	>36
Interaction Uniformity		
Amplitude (dB)	±0.5	±0.5
Phase (Time Domain) (deg)	<±5	<±5

† Above thermal noise floor with input powers at +20 dBm.

**TABLE 5-2**  
**Module Performance Characteristics**

<b>Isolation</b>	
Input — Input	>60 dB
Input — Output	>60 dB
<b>Switch Characteristics</b>	
ON Insertion Loss	<1.0 dB
OFF Isolation	>40 dB
Passband Ripple	<1.0 dB
Input Power Level	+23 dBm
Second-Harmonic Generation	<60 dBc
<b>Switching Speed</b>	
Commutation	<10 ns
Mode	<1 μs
<b>Filtering</b>	
Output Rejection of 300 MHz	>30 dB
Phase Variation	<10°
Output Amplification	>20 dB

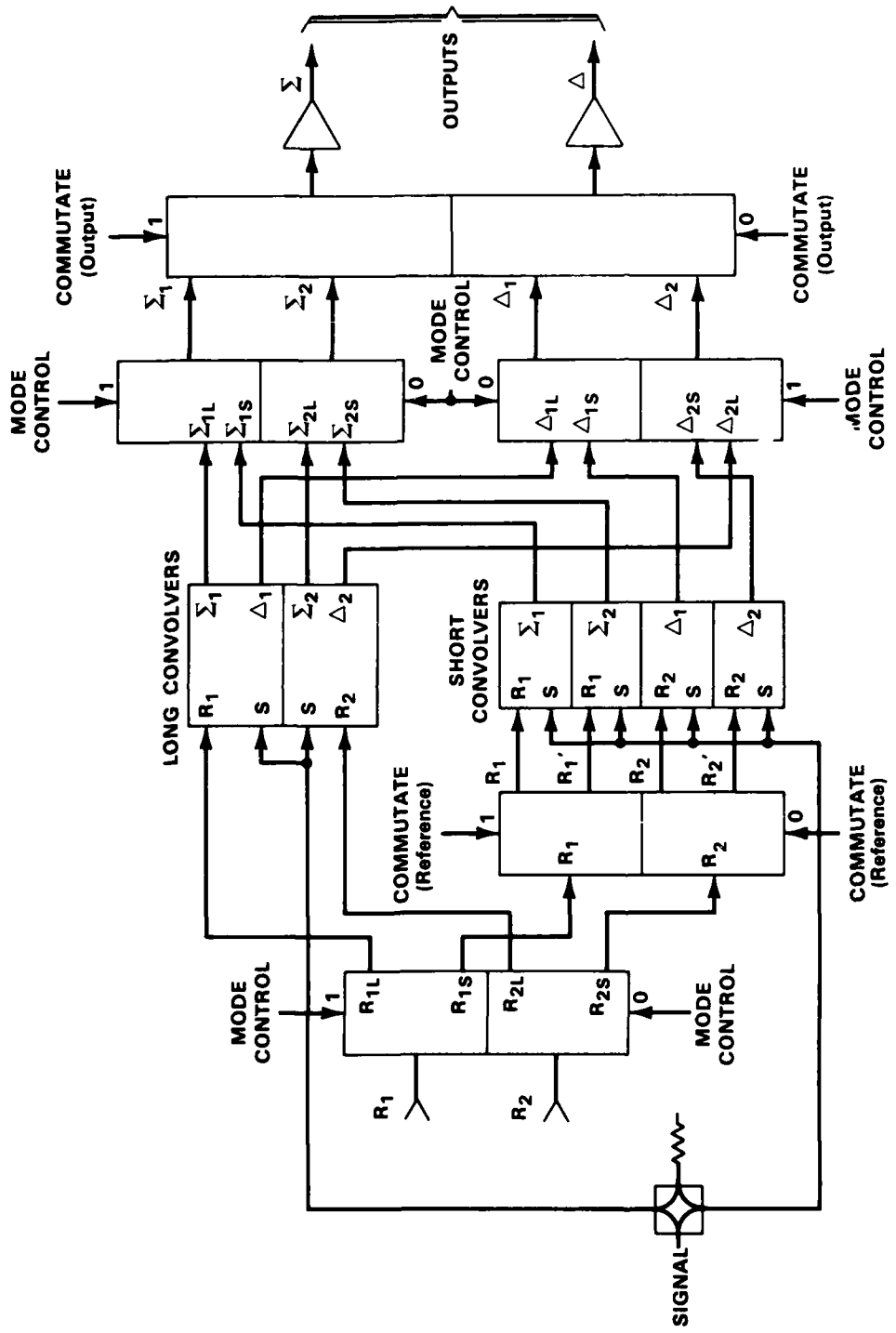


Figure 5-3. Convolver module switching-matrix schematic.

complexity with no sacrifice in performance. The mode switches are used to select high or low data rates, i.e., short or long convolvers, and switch both input references as well as outputs. The reference commutation is provided only to the short convolvers.

The stripline module which integrates the convolvers, switches, switch drivers, filters, and amplifiers is shown in Figure 5-4. It is a five-layer module, 7 × 7 in. square. Two signal planes sandwiched between three ground planes routing all signals from convolvers to switches provide the required isolation and filtering. All power and switching signals are entered via an edge connector; all the radio-frequency signals are entered through SMA connectors on the opposite end of the module.



Figure 5-4. Convolver module assembly.

The inputs to the convolvers are 100 MHz in bandwidth, centered at 300 MHz. The uncorrelated convolver output is a low-level (-60-dBm) signal, 200 MHz in bandwidth, centered at 600 MHz. Therefore, it is essential to maintain good input/output isolation on the module.

RD-A147 429 SOLID STATE RESEARCH(U) MASSACHUSETTS INST OF TECH  
LEXINGTON LINCOLN LAB A L MCWHORTER 15 FEB 84 1984-1  
ESD-TR-84-006 F19628-80-C-0002

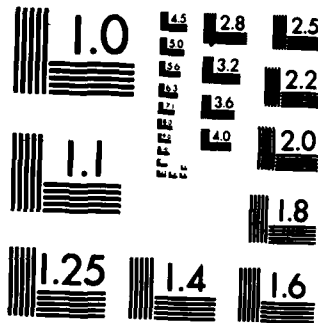
3/2

UNCLASSIFIED

F/G 20/12

NL





It is also important to have low switch insertion loss, since it adds directly to the noise figure of the module and subtracts from the dynamic range.

Additionally, switch speed directly affects implementation loss as  $(T - \tau)/T$ , where  $\tau$  is the switching time and  $T$  is the length of the coded waveform. The switching time is 10 ns and the waveform length is 700 ns for the short convolver. This contributes a loss of only 0.062 dB for the short convolver.

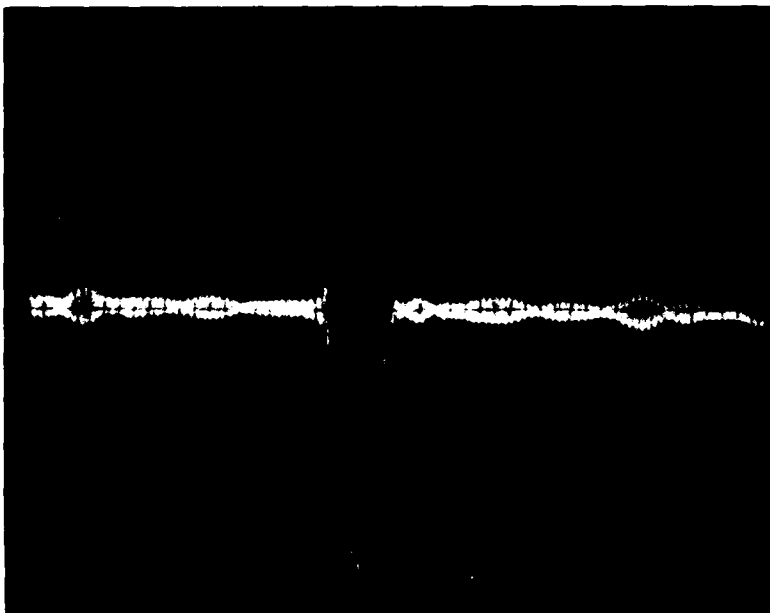


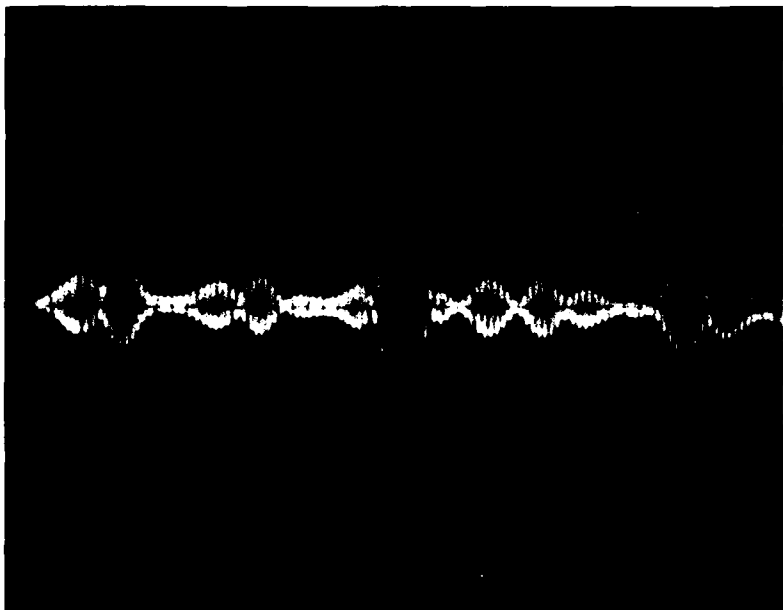
Figure 5-5. Short-convolver correlation waveform.

Correlation waveforms for the short and long convolvers are shown in Figures 5-5 and 5-6, respectively. All output pairs vary by less than 1.0 dB. Stationary time sidelobes exist because a repeated pseudorandom code was used for tests. Preliminary measurements of correlation-peak/sidelobe rms ratios are 29.8 dB for the long convolver and 16.5 dB for the short convolver, close to the theoretical values.

V.S. Dolat  
G.T. Flynn

## 5.2 CONCEPT FOR A HOLOGRAPHIC-GRATING BULK-ACOUSTIC-WAVE REFLECTIVE-ARRAY DEVICE

Surface-acoustic-wave (SAW) grating devices are finding extensive application as RF signal-processing elements. It has become evident that SAW devices are limited in bandwidth to about 1 GHz by a number of fundamental factors<sup>4</sup> such as dispersion and loss due to surface defects, propagation loss due to phonon scattering, and photolithography feature size limitations.



13884-S

Figure 5-8. Long-convolver correlation waveform.

We propose a new class of acoustic reflection-grating devices which employ bulk acoustic waves (BAW) instead of surface waves, and which employ a reflection grating within the bulk crystal made by the optical holographic technique<sup>5</sup> of interfering two coherent light beams within the crystal, as seen in Figure 5-7. An optical phase hologram can be formed in LiNbO<sub>3</sub>, and once the hologram is established the laser illuminator is removed. If the material is kept in the dark, the hologram will be stored indefinitely. The stored hologram can interact with an acoustic wave by means of the electroacoustic effect, where the stored electric field causes changes in the acoustic velocity.<sup>6</sup> In the simplest case, a periodic hologram forms a narrow-band reflector, and a bandpass filter becomes possible as illustrated in Figure 5-7. The acoustic wave does not degrade the stored grating, and the acoustic properties are expected to be essentially constant for years with properly stored holograms. The hologram, however, could be erased with light and rewritten at any time to reprogram the filter function. BAW devices can operate at higher frequencies and therefore higher bandwidths than SAW devices<sup>7</sup> (bandwidths approaching 5 GHz are possible). Also, BAWs have lower loss, are insensitive to surface effects, and require no extensive photolithography.

We can estimate the strength of the acoustic reflection in LiNbO<sub>3</sub> using our previously measured values of the electroacoustic coefficients.<sup>8</sup> We assume a simple periodic grating created by the interference of two uniform, plane light waves of the same wavelength. We also assume, as reported in the literature,<sup>9</sup> that the stored electric field of the hologram is 50 kV/cm. The incident acoustic beam is at the Bragg wavelength and at normal incidence

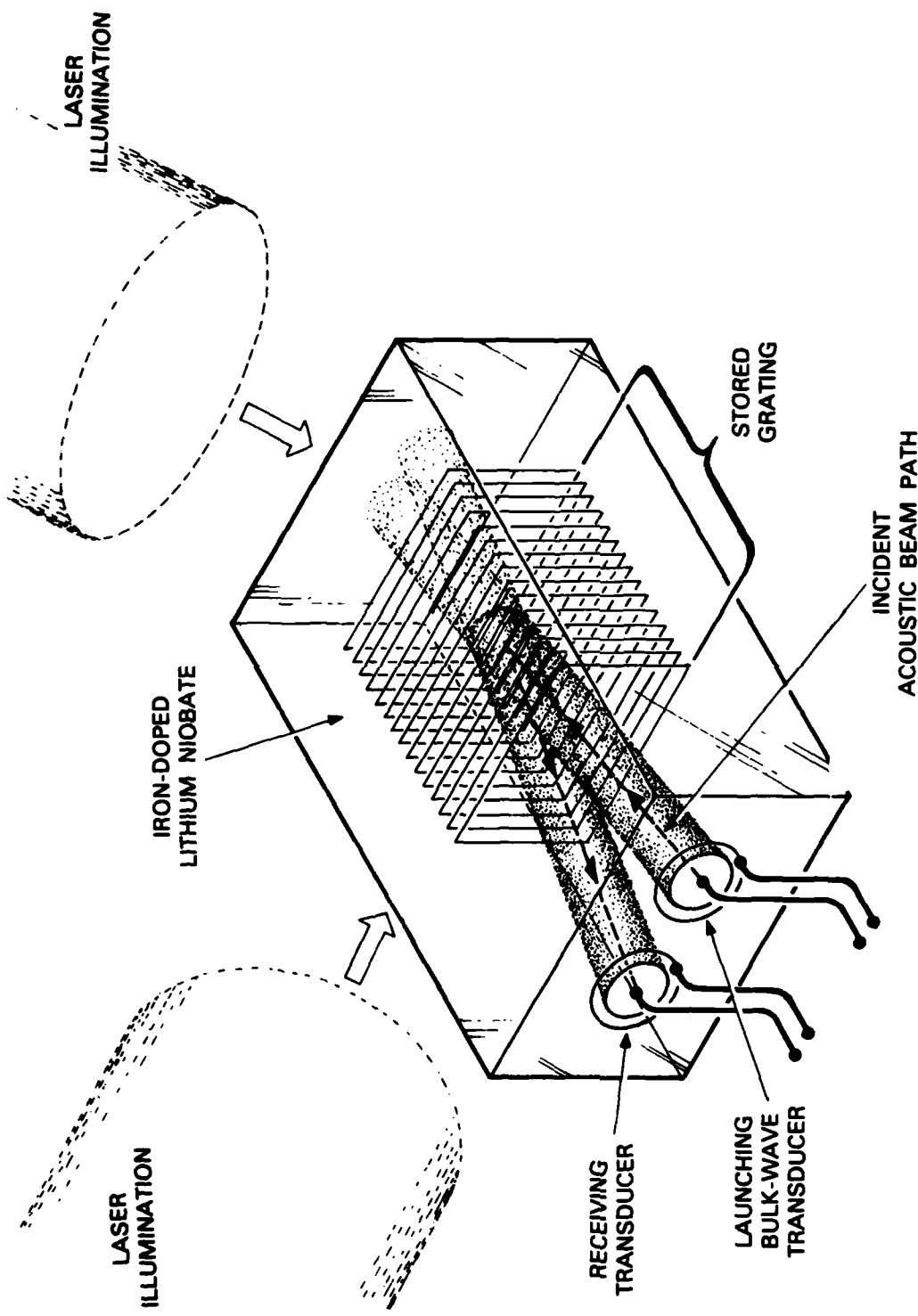


Figure 5-7. Bulk-acoustic-wave grating reflector. Stored grating is created by interference of two laser beams. Incident acoustic beam strongly interacts with grating in a narrow frequency band, thus forming a bandpass filter.

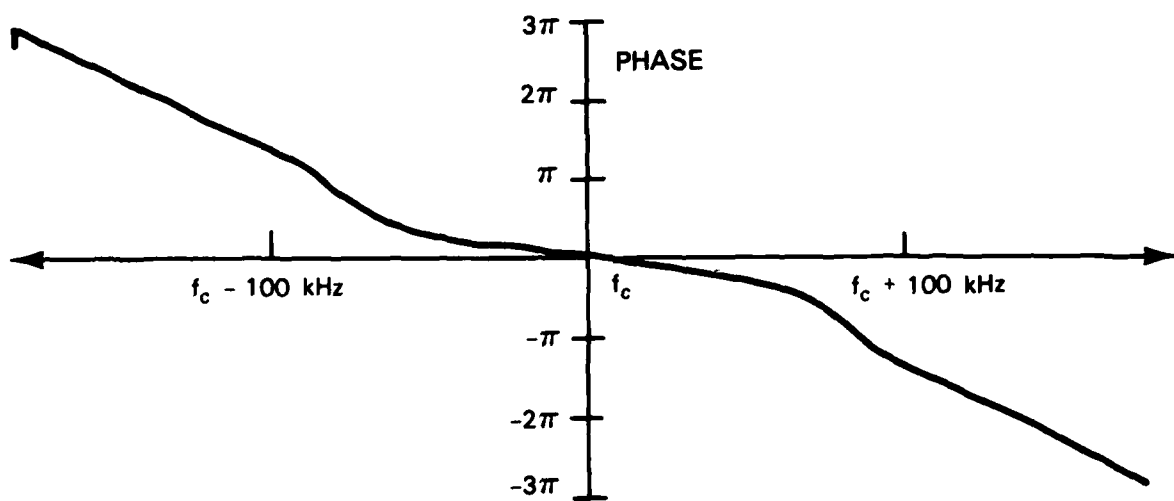
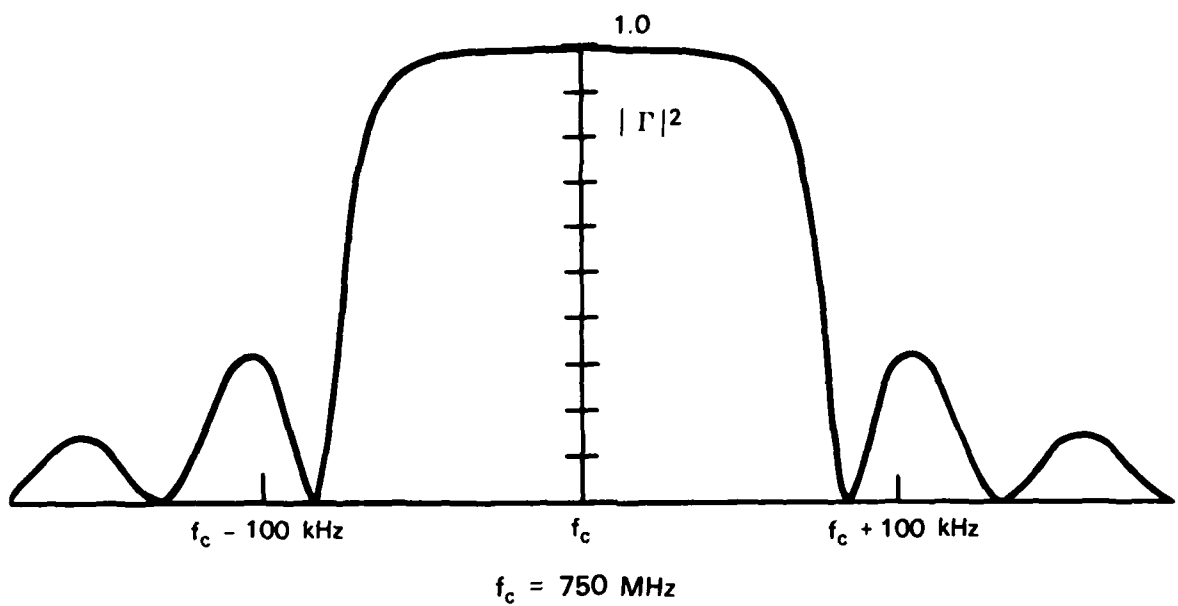


Figure 5-8. Theoretical response of a holographic-grating bandpass filter in  $\text{LiNbO}_3$  calculated from coupled-wave theory.

133188-H-01

to the grating. If we neglect loss and depletion effects, the total reflection  $|\Gamma|$  from the grating is given by<sup>8</sup>

$$|\Gamma| = N \left( \frac{\Delta\rho}{\rho} + \frac{\Delta v}{v} \right)$$

where  $N$  is the number of periods in the grating,  $\Delta\rho/\rho$  is the relative change in density of the medium, and  $\Delta v/v$  is the relative change of velocity of the acoustic wave caused by the stored hologram. The density change  $\Delta\rho/\rho$  can be calculated from the piezoelectric coefficient, and  $\Delta v/v$  is obtained from the measured electroacoustic coefficient. An estimate of  $|\Gamma|$  for a grating in  $\text{LiNbO}_3$  at 50 kV/cm stored field is

$$|\Gamma| = 2.7 \times 10^{-4} \text{ N}$$

This implies that for  $N$  of order  $10^4$ , an acoustic wave would experience full depletion. Thus, the reflections are strong enough that useful grating devices are feasible. This simple result is borne out by a more rigorous coupled-wave calculation. Figure 5-8 shows the result of coupled-wave calculations<sup>10</sup> for the acoustic reflection coefficient (i.e., ratio of the acoustic field strength of the reflected acoustic beam to that of the incident field strength) for the case of a grating of length 1 cm, assuming 50 kV/cm peak stored fields and a center frequency of 750 MHz. The flattening in the passband of  $|\Gamma|^2$  in Figure 5-8 is caused by large depletion effects, indicating a very strong interaction of the bulk longitudinal wave with the grating.

Clearly, the next step is the fabrication of a holographically stored grating device based on the principles presented above. Efforts to this end are now under way.

D.E. Oates  
P.G. Gottschalk

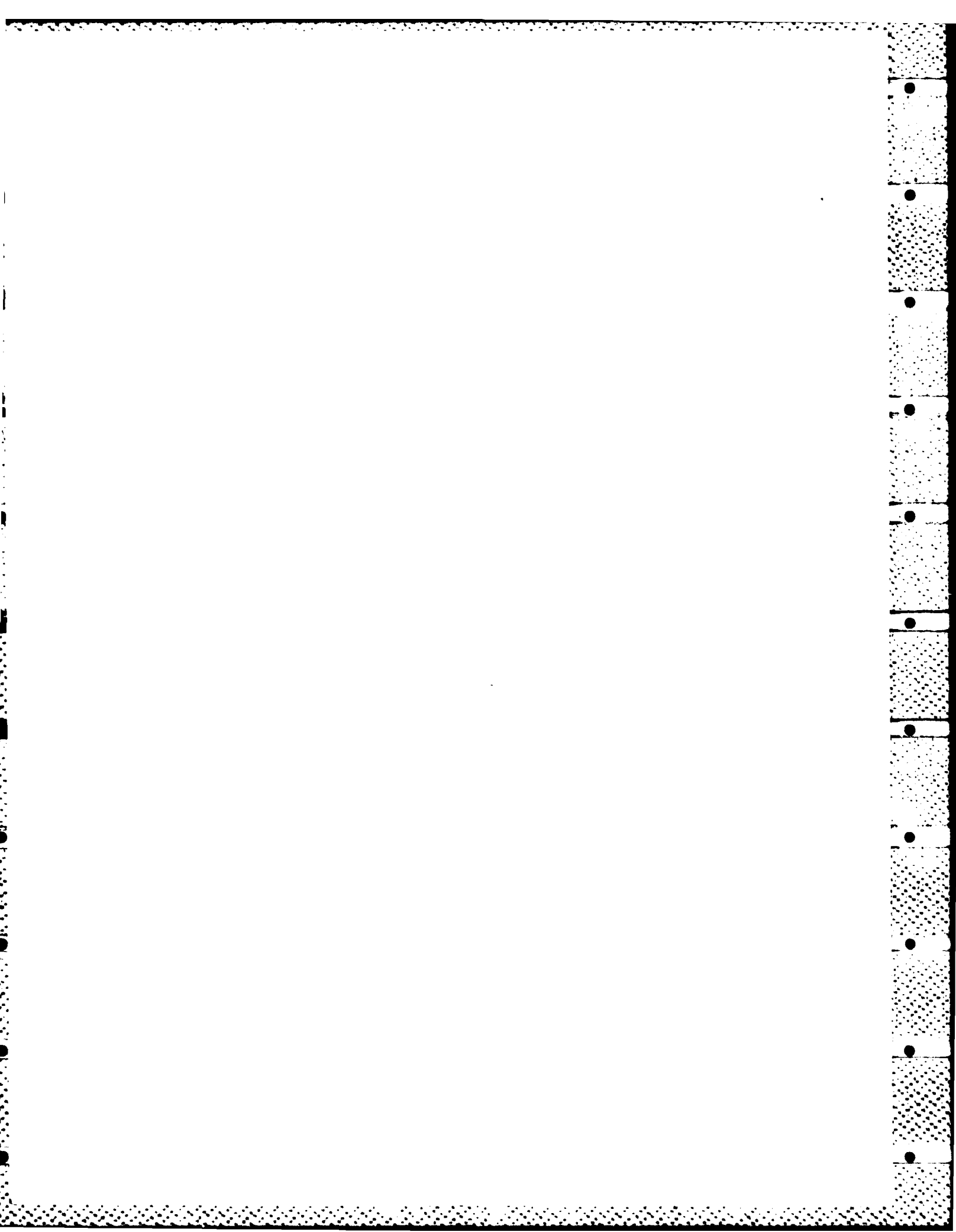
## REFERENCES

1. D. Brodtkorb and J.E. Laynor, in *1978 Ultrasonics Symposium Proceedings* (IEEE, New York, 1978), pp. 561-566, DTIC AD-A069926/4.
2. S.A. Reible, J.H. Cafarella, R.W. Ralston, and E. Stern, in *1976 Ultrasonics Symposium Proceedings* (IEEE, New York, 1976), pp. 451-455, DTIC AD-A040519/1.
3. I. Yao, in *1981 Ultrasonics Symposium Proceedings* (IEEE, New York, 1981), pp. 181-185, DTIC AD-A117861/5; and Solid State Research Report, Lincoln Laboratory, M.I.T. (1981:4), pp. 56-61, DTIC AD-A114189/4.
4. R.C. Williamson, in *1974 Ultrasonics Symposium Proceedings* (IEEE, New York, 1974), pp. 321-328, DTIC AD-A011322/5.
5. D.L. Staebler, *Topics in Applied Physics Vol. 20, Holographic Recording Materials* (Springer-Verlag, Berlin, 1977), pp. 101-132.
6. R.B. Thompson and C.F. Quate, *J. Appl. Phys.* **42**, 907 (1971).
7. A.H. Meitzler, *Ultrasonic Transducer Materials* (Plenum Press, New York, 1971), pp. 125-182.
8. Solid State Research Report, Lincoln Laboratory, M.I.T. (1983:2), p. 63, DTIC AD-A134594/1.
9. E. Kratzig and H. Kurz, *J. Electrochem. Soc.* **124**, 131 (1977).
10. H.A. Haus and P.V. Wright, in *1980 Ultrasonics Symposium Proceedings* (IEEE, New York, 1980), pp. 277-281.

## UNCLASSIFIED

SECURITY CLASSIFICATION OF THIS PAGE (When Data Entered)

REPORT DOCUMENTATION PAGE		READ INSTRUCTIONS BEFORE COMPLETING FORM															
1. REPORT NUMBER  ESD-TR-84-006	2. Govt Accession No.  A1447429	3. RECIPIENT'S CATALOG NUMBER															
4. TITLE (and Subtitle)  Solid State Research		5. TYPE OF REPORT & PERIOD COVERED  Quarterly Technical Report 1 November 1983 — 31 January 1984															
7. AUTHOR(s)  Alan L. McWhorter		8. PERFORMING ORG. REPORT NUMBER 1984:1															
9. PERFORMING ORGANIZATION NAME AND ADDRESS  Lincoln Laboratory, M.I.T. P.O. Box 73 Lexington, MA 02173-0073		10. PROGRAM ELEMENT, PROJECT, TASK AREA & WORK UNIT NUMBERS  Program Element No. 63250F Project No. 649L															
11. CONTROLLING OFFICE NAME AND ADDRESS  Air Force Systems Command, USAF Andrews AFB Washington, DC 20331		12. REPORT DATE  15 February 1984															
14. MONITORING AGENCY NAME & ADDRESS (if different from Controlling Office)  Electronic Systems Division Hanscom AFB, MA 01731		15. SECURITY CLASS. (of this report)  Unclassified															
16. DISTRIBUTION STATEMENT (of this Report)  Approved for public release; distribution unlimited.																	
17. DISTRIBUTION STATEMENT (of the abstract entered in Block 20, if different from Report)																	
18. SUPPLEMENTARY NOTES  None																	
19. KEY WORDS (Continue on reverse side if necessary and identify by block number)  <table style="width: 100%; border-collapse: collapse;"> <tr> <td style="width: 33%;">solid state devices</td> <td style="width: 33%;">photodiode devices</td> <td style="width: 33%;">surface-wave transducers</td> </tr> <tr> <td>quantum electronics</td> <td>lasers</td> <td>charge-coupled devices</td> </tr> <tr> <td>materials research</td> <td>imaging arrays</td> <td>acoustoelectric devices</td> </tr> <tr> <td>microelectronics</td> <td>LIDAR system</td> <td>waveguide structures</td> </tr> <tr> <td>analog device technology</td> <td></td> <td></td> </tr> </table>			solid state devices	photodiode devices	surface-wave transducers	quantum electronics	lasers	charge-coupled devices	materials research	imaging arrays	acoustoelectric devices	microelectronics	LIDAR system	waveguide structures	analog device technology		
solid state devices	photodiode devices	surface-wave transducers															
quantum electronics	lasers	charge-coupled devices															
materials research	imaging arrays	acoustoelectric devices															
microelectronics	LIDAR system	waveguide structures															
analog device technology																	
20. ABSTRACT (Continue on reverse side if necessary and identify by block number)  <p style="margin-left: 40px;">This report covers in detail the solid state research work of the Solid State Division at Lincoln Laboratory for the period 1 November 1983 through 31 January 1984. The topics covered are Solid State Device Research, Quantum Electronics, Materials Research, Microelectronics, and Analog Device Technology. Funding is primarily provided by the Air Force, with additional support provided by the Army, DARPA, Navy, NASA, and DOE.</p>																	



END

SEARCHED

2-84

DTIC